UNIVERSITY OF CALIFORNIA

SAN DIEGO

A Study of Hadron-Proton Elastic Scattering at High Energy and Large Momentum Transfer

A dissertation submitted in partial satisfaction of the requirements for the degree Doctor of Philosophy in Physics

by

Sean Francis McHugh

Committee in charge:

Professor Robert A. Swanson, Chair
Professor Joseph Kraut
Professor Wayne Vernon
Professor David Y. Wong
Professor Manuel Rotenberg
Dr. Hans Kobrak

1983

The dissertation of Sean Francis McHugh is approved,

and it is acceptable in quality and form for

publication on microfilm:

Joseph Kraut

Hans Kobzak

Wayne Vernon

David Wong

Daniel Rothberg

Robert A. Swanson

Chair

University of California, San Diego

1983

Table of Contents

		Page
	List of Figures	vi
	List of Tables	x
	Acknowledgments	xii
	Vita and Publications	xiii
	Abstract	xiv
I.	Introduction	1
II.	Theory	7
	A. Chou-Yang model	8
	B. Elastic scattering and QCD	14
III.	Experimental Apparatus	20
IV.	Data Reduction	30
V.	Results	32
VI.	Conclusions	55
	References	64
Appendix 1.	The M6 Beam	66
Appendix 2.	Beam Differential Cerenkov Counter	75
Appendix 3.	Threshold Cerenkov Counter	79
Appendix 4.	Liquid Hydrogen Target and Target Veto Counters	82
Appendix 5.	Forward and Recoil Spectrometers	84
Appendix 6.	Proportional Wire Chambers	89

Page

Appendix 7.	Trigger Hodoscopes and Scintillation Counters	94
Appendix 8.	Trigger Logic	98
Appendix 9.	Elastic Two Body Kinematics	103
Appendix 10.	Event Reconstruction and Selection	106
Appendix 11.	Monte Carlo	143
Appendix 12.	Particle Separation	164
Appendix 13.	Cross Section Calculation	169
Appendix 14.	Chou-Yang Analysis	195

List of Figures

Figure		Page
1.1	Proton-proton elastic differential cross sections at incident beam momenta of 3 to 24 GeV/c	4
1.2	$\pi^- p$ elastic differential cross sections at incident beam momenta of 5 to 22.6 GeV/c	5
1.3	Proton-proton elastic differential cross sections at center of mass energies 23 to 62 GeV	6
2.1	Example of QCD diagrams for meson-proton scattering	17
2.2	Elastic pp scattering at fixed θ	17
2.3	Leading diagrams contributing to the Landshoff mechanism for pp scattering and πp scattering . . .	18
2.4	Proton-proton elastic differential cross section at equivalent laboratory incident momentum near 500 GeV/c and 1500 GeV/c	19
3.1	Beam apparatus and forward spectrometer	25
3.2	Forward and recoil spectrometers	27
3.3	Recoil spectrometer	29
5.1	100 GeV/c $\bar{p}p$ elastic differential cross section	40
5.2	200 GeV/c $\bar{p}p$ elastic differential cross section	41
5.3	100 GeV/c pp elastic differential cross section	42
5.4	200 GeV/c pp elastic differential cross section	43
5.5	100 GeV/c $\pi^- p$ elastic differential cross section . . .	44
5.6	200 GeV/c $\pi^- p$ elastic differential cross section . . .	45
5.7	100 GeV/c $\pi^+ p$ elastic differential cross section . . .	46
5.8	200 GeV/c $\pi^+ p$ elastic differential cross section . . .	47

Figure		Page
5.9	100 GeV/c K^-p elastic differential cross section . . .	48
5.10	200 GeV/c K^-p elastic differential cross section . . .	49
5.11	100 GeV/c K^+p elastic differential cross section . . .	50
5.12	200 GeV/c K^+p elastic differential cross section . . .	51
5.13	The coplanarity elastic signal in four ranges of t . . .	53
6.1	The profile function, $\Gamma(b)$, for the 200 GeV/c for the pp and π^-p elastic scattering systems	59
6.2	The proton form factor	61
6.3	The pion form factor	63
A1.1	M6 beam optics	74
A2.1	Cerenkov counter pressure curve	78
A3.1	Response of the threshold Cerenkov counter to 100 GeV/c, $\bar{p}$, K^- and π^-	80
A3.2	Response of the threshold Cerenkov counter to 200 GeV/c, $\bar{p}$, K^- and π^-	81
A8.1	Trigger logic	101
A8.2	Beam, fast veto and logic gate	102
A10.1	Cluster size distribution	122
A10.2	Number of clusters per chamber	123
A10.3	Track segment algorithm	125
A10.4	Number of track segment candidates	126
A10.5	The effect of large angles on the magnetic center	127

Figure		Page
A10.6	Geometrical and kinematic distributions used in the event selection. DXF (mm)	129
A10.7	DXR (mm)	131
A10.8	(PF-PFM)/PF	133
A10.9	$(PR-PRM)/PR^2$ $(GeV/c)^{-1}$	135
A10.10	YD (mm)	137
A10.11	$(TF-TR)/(a + b\|TF\|)$	139
A10.12	CPL	141
A11.1	Comparison between Monte Carlo and real data DXF (mm)	150
A11.2	DXR (mm)	151
A11.3	$[(PF-PRM)/PF] \times 10^3$	152
A11.4	$(PR-PRM)/PR^2$ $(GeV/c)^{-1}$	153
A11.5	YD (mm)	154
A11.6	$(TF-TR)/(a + b\|TF\|)$	155
A11.7	$CPL \times 10^3$	156
A11.8	$CPL \times 10^3$	157
A11.9	$CPL \times 10^3$	158
A11.10	$CPL \times 10^3$	159
A11.11	Geometrical acceptance	161
A11.12	The effect of vertical focusing on the residual in the downstream Y proportional chambers	163

Figure Page

A13.1 Rate correction extrapolation 177

A13.2 Measurement resolution of -t as a function of -t . . 179

List of Tables

Table		Page
5.1	Elastic differential cross sections for negative 200 GeV/c beam	35
5.2	Elastic differential cross sections for positive 200 GeV/c beam	36
5.3	Elastic differential cross sections for negative 100 GeV/c beam	37
5.4	Elastic differential cross section for positive 100 GeV/c beam	38
5.5	Error in normalization	39
A1.1	Properties of the M6 beam as determined by program TURTLE	70
A1.2	M6 beam line elements	71
A2.1	Beam composition	77
A2.2	CB efficiency	77
A4.1	Hydrogen target	83
A5.1	Analysis magnets	87
A5.2	Chamber deployment	88
A6.1	Chamber efficiencies	93
A7.1	Hodoscopes	96
A7.2	Additional scintillators	97
A8.1	Logic matrices	100
A10.1	Pattern recognition groups	113
A10.2	Trajectory parameterization	114

Table Page

A10.3 Analysis constants 115

A10.4 Measurement variable definitions 116

A10.5 Resolutions used for initial cuts 118

A10.6 Final event selection criteria 119

A10.7 Fiducial cuts 120

A10.8 Event selection history 121

A12.1 CF calibration 166

A12.2 CB calibration 167

A12.3 Particle contamination correction matrix (P_{ij}) 168

A13.1 Corrections to incident hadron flux 180

A13.2 Acceptance and corrections
100 GeV/c $\bar{p}p$ acceptance and corrections 183

A13.3 200 GeV/c $\bar{p}p$ acceptance and corrections 184

A13.4 100 GeV/c pp acceptance and corrections 185

A13.5 200 GeV/c pp acceptance and corrections 186

A13.6 100 GeV/c $\pi^- p$ acceptance and corrections 187

A13.7 200 GeV/c $\pi^- p$ acceptance and corrections 188

A13.8 100 GeV/c $\pi^+ p$ acceptance and corrections 189

A13.9 200 GeV/c $\pi^+ p$ acceptance and corrections 190

A13.10 100 GeV/c $K^- p$ acceptance and corrections 191

A13.11 200 GeV/c $K^- p$ acceptance and corrections 192

A13.12 100 GeV/c $K^+ p$ acceptance and corrections 193

A13.13 200 GeV/c $K^+ p$ acceptance and corrections 194

A14.1 Parameters for fit to scattering amplitude 197

Acknowledgments

I sincerely thank Hans Kobrak and Bob Swanson for their efforts on my behalf during my tenure as a graduate student. I also thank my family for their support. This experiment was the result of a collaboration of four institutions, University of Arizona, Cornell University, Fermilab and UCSD. I would like to thank the collaborators from these institutions as well as the staffs of Fermilab and UCSD. Special thanks to to my fellow graduate students, Dave Kaplan, Paul Karchin and Keith Krueger for many enlightening discussions and moral support during the experiment and to Annetta Whiteman for the preparation of this manuscript.

Also thanks go to the American taxpayer who paid for this.

This work was supported by the National Science Foundation.

Vita

Born - Plainfield, New Jersey

1977	B.S. Harvey Mudd College
1977-1978	Teaching Assistant, Department of Physics, University of California, San Diego
1978-1983	Research Assistant, Department of Physics, University of California, San Diego
1983	Doctor of Philosophy, University of California, San Diego

Publications

"Observation of Structure in Large-Momentum-Transfer $\pi^- p$ Elastic Scattering at 200 GeV/c" (with W. F. Baker, D. P. Eartly, J. S. Klinger, A. J. Lennox, R. Rubinstein, R. M. Kalbach, K. W. Krueger, A. E. Pifer, D. H. Kaplan, P. Karchin, Jay Orear), Phys. Rev. Lett. 47 (1981) 1683.

"Antiproton-proton and proton-proton elastic scattering at 100 and 200 GeV/c" (with D. H. Kaplan, P. Karchin, J. Orear, R. M. Kalbach, K. W. Krueger, A. E. Pifer, W. F. Baker, D. P. Eartly, J. S. Klinger, A. J. Lennox, R. Rubinstein), Phys. Rev. D26 (1982) 723.

"Elastic scattering of $\pi^{\pm}$ and $K^{\pm}$ on protons at 100 and 200 GeV/c" (with R. M. Kalbach, K. W. Krueger, A. E. Pifer, D. H. Kaplan, P. Karchin, J. Orear, W. F. Baker, D. P. Eartly, J. S. Klinger, A. J. Lennox, R. Rubinstein), Phys. Rev. D27 (1983) 2752.

ABSTRACT OF THE DISSERTATION

A Study of Hadron-Proton Elastic Scattering at High Energy and Large Momentum Transfer

by

Sean Francis McHugh

Doctor of Philosophy in Physics

University of California, San Diego, 1983

The differential cross sections of π^+, π^-, K^+, K^-, p, $\bar{p}$ on p elastic scattering were measured at laboratory momenta of 100 and 200 GeV/c in the range of four momentum transfer squared

$$0.9 < -t < 11.0 \ (\mathrm{GeV}/c)^2 \quad \text{at 100 GeV/c}$$

and

$$0.4 < -t < 3.0 \ (\mathrm{GeV}/c)^2 \quad \text{at 200 GeV/c}$$

The data obtained extend the knowledge of these cross sections to large momentum transfer. The primary emphasis of this experiment was to study the $\pi^- p$ reaction. This cross section falls six decades between $-t = 0.9$ and $-t = 3.8 \ (\mathrm{GeV}/c)^2$. At $-t = 3.8 \ (\mathrm{GeV}/c)^2$

there is a dip which is followed by a secondary maximum at $-t = 5.5\ (\mathrm{GeV}/c)^2$. At larger values of $-t$ the measured cross section falls more slowly than in the low $-t$ region. This dip-bump structure is a characteristic of optical models. One such model, the Chou-Yang model, has been used to extract the π^- form factor from the data.

I. Introduction

This thesis describes an experiment to study the elastic scattering of long lived hadrons ($\pi^{\pm}$, $K^{\pm}$, p, $\bar{p}$) on protons at incident momenta of 100 and 200 GeV/c and with four-momentum transfer squared, t, between -0.9 and -11 $(GeV/c)^2$ at 200 GeV/c and between -0.4 and -3.0 $(GeV/c)^2$ at 100 GeV/c. Primary emphasis was placed on obtaining the $\pi^- p$ cross section at 200 GeV/c over the entire range of acceptance of the detector.

Extensive data exist for the pp reaction at these energies[1-3] and also at higher energies.[4] Our measurement of this process served as a check. Data for ($\pi^{\pm}$, $K^{\pm}$)[5-7] and $\bar{p}$[8] reactions exist at lower energies. Data for these reactions at beam energies of 100 GeV or more exist only in the low momentum transfer (low -t) region.[1,9,10] The results of this experiment extend these data to higher momentum transfer. In addition, these reactions have recently been measured in the high -t range with beam energies between 20 and 50 GeV.[11]

Hadron-proton scattering at high energy is a way of studying hadron structure. Collisions with large momentum transfer can be used to investigate (via the uncertainty principle) the short range part of the interaction. If the hadrons are composed of constituents, then the effect of collisions between individual constituents may become important at large momentum transfer. Experiments which study

protons with a point-like probe, a lepton or photon, complement the hadron elastic scattering data. These experiments probe the proton with electromagnetic or weak interactions. It is necessary to use another hadron to study the proton with the strong interaction.

In addition, the mesons cannot be studied with point-like probes at large momentum transfer. Because they do not exist in stable states suitable for targets, the meson must be a beam particle. Furthermore, the only stable point-like probe suitable as a fixed target is an electron. The maximum value of $-t$ is approximately equal to s, the center of mass energy squared ($s \cong 2\,ME$ where M is the fixed target mass and E is the beam energy). Hence the maximum momentum transfer is limited by the low mass of the electron. With a given beam energy, much larger momentum transfers may be obtained with a proton target.

Figure 1.1 and figure 1.2 show the pp and $\pi^- p$ differential cross sections at low energies. Both are characterized by a large peak in the forward (low-t) direction. This "diffraction" peak follows a simple exponential form at low $-t$. As the beam energy increases this form extends to higher $-t$. At larger $-t$ the cross sections fall more slowly with increasing $-t$. The pp cross section is smooth in this region whereas the $\pi^- p$ cross section exhibits dips and bumps. In both cases the cross section is strongly dependent on s in this region. At low energies, the other cross sections

(π^+, $K^\pm$, $\bar{p}$) are characterized by a diffraction peak followed by a strongly s dependent form.

The $\bar{p}p$ cross section develops a dip at $-t \cong 1.4\ (\mathrm{GeV}/c)^2$ at a beam energy of 150 GeV.[12] This dip persists to the highest energies available.[4] At these energies (figure 1.3) the cross sections show little dependence on s. The slope of the diffraction peak increases slightly (the diffraction peak becomes narrower) and the dip position moves to lower -t with increasing s.

Many models have been proposed to explain the shape and energy dependence of the proton-proton cross section. The study of the elastic scattering of other hadrons on protons serves to put some constraints on these models.

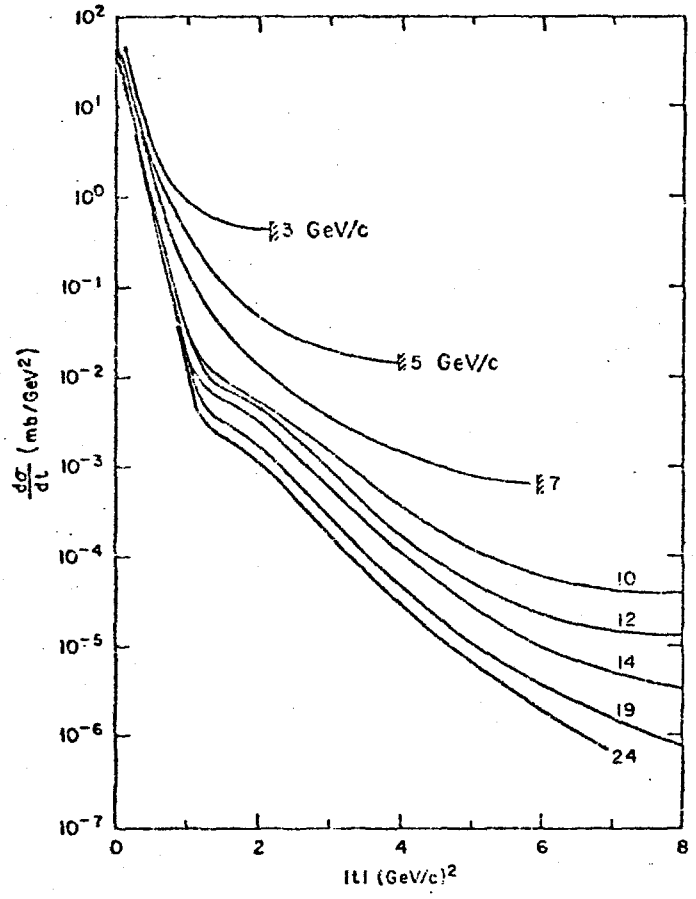

Figure 1.1. Proton-proton elastic differential cross sections at incident beam momenta of 3 to 24 GeV/c. This figure was reproduced from reference 13.

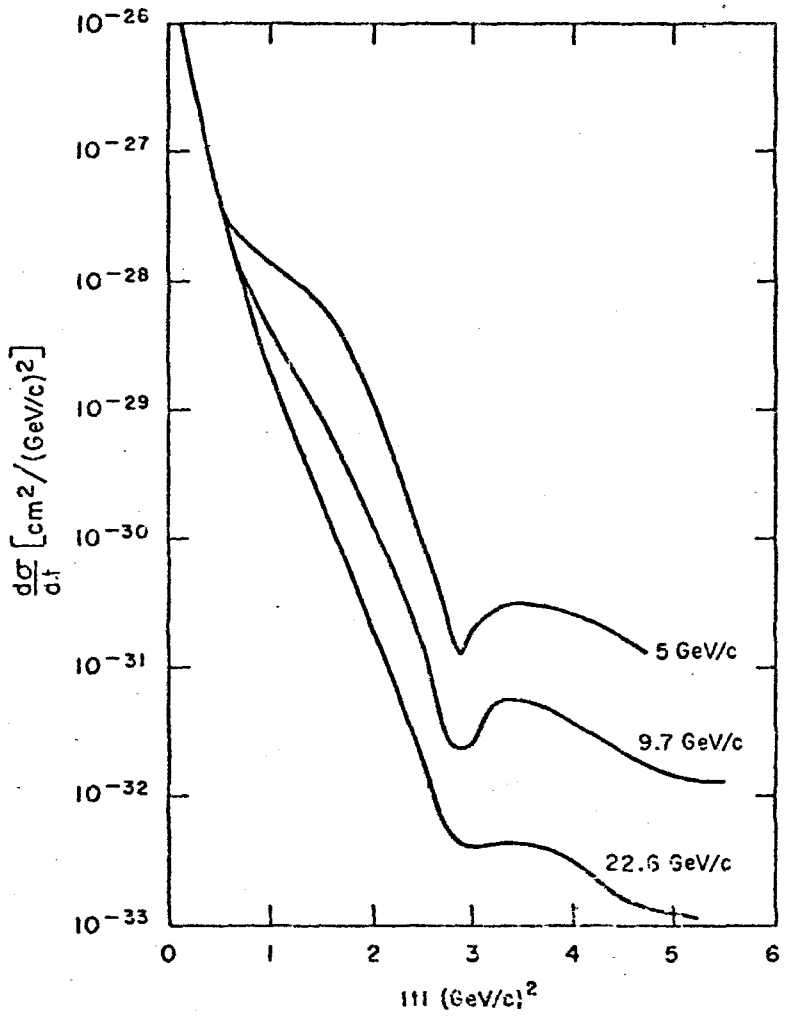

Figure 1.2. $\pi^- p$ elastic differential cross sections at incident beam momenta of 5 to 22.6 GeV/c. This figure was reproduced from reference 13.

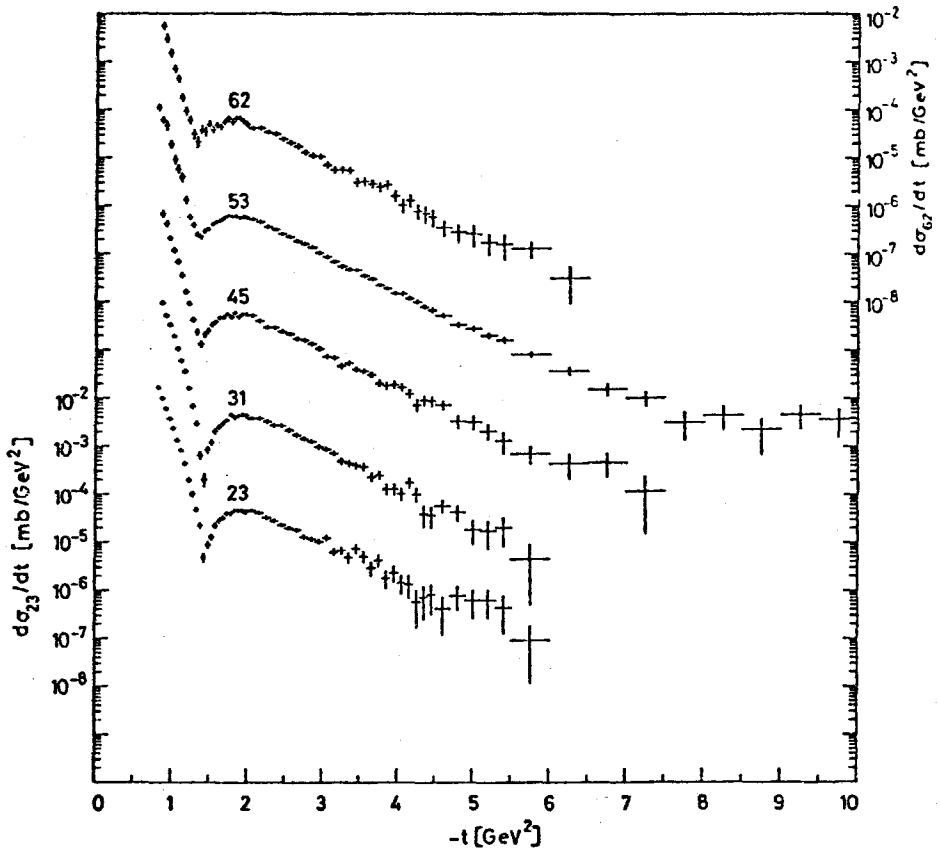

Figure 1.3. Proton-proton elastic differential cross sections at center of mass energies 23 to 62 GeV. The data are displaced by factors of 10 for clarity. This figure was reproduced from reference 4.

II. Theory

There are many phenomenological models which describe the elastic scattering of hadrons. Reference 15 is a comprehensive review of current theories of this subject. The application of Regge theory to elastic scattering is discussed in reference 16. Unfortunately, Regge theory has little to say about the t dependence of the cross sections. Other models are based on an assumed structure of the hadrons. The "multiple scattering" [17] model of Wakaizumi, for instance, defines the cross section in terms of an effective potential derived from the quark-quark scattering of the hadrons. A model by Van Hove [18] takes a different point of view and assumes that the elastic scattering of hadrons is due to the "glue" that holds the constituents of the hadron together. The Chou-Yang model, [19] analyzes the proton scattering data in terms of a form factor. This form factor can be compared to that extracted from proton electron scattering data. Similarly, the electromagnetic form factor of the extracted from pion electron scattering data (up to $-t = 0.1\ (\mathrm{GeV}/c)^2$) and pion electro production (up to $-t = 4\ (\mathrm{GeV}/c)^2$, [20] can be compared to the pion form factor extracted from pion proton scattering data. This model is the subject of section A.

In the past ten years a new theory of strong interactions, quantum chromodynamics (QCD) has been formulated. This is a color SU(3) gauge theory of quarks interacting through gluons.

Unfortunately, the theory does not lead readily to precise calculations at accessible momentum transfers. Its application to hadron elastic scattering is the subject of section B.

A. Chou-Yang model

The model uses the impact parameter representation which is derived from the partial wave expansion of the scattering amplitude.[21] It is assumed that the scattering system possesses azimuthal symmetry and that spin effects can be ignored in the high energy limit. The differential cross section is given by

$$\frac{d\sigma}{dt} = \frac{\pi}{k^2} |a|^2 \tag{1}$$

where the scattering amplitude, a, is given by

$$a = \frac{1}{ik} \sum_{\ell} \left(\ell + \frac{1}{2}\right) P_{\ell}(\cos\theta)(1 - S_{\ell}) \tag{2}$$

Here k is the wave number of the center of mass momentum p,

$$k = \frac{p}{h} \tag{3}$$

P_{ℓ} is the ℓ'th Legendre polynomial and the complex coefficients, S_{ℓ}; depend on the form of the scattering reaction. In general, $|S_{\ell}| \leq 1$ and in the absence of absorption (inelastic reactions) $|S_{\ell}| = 1$. Equation (2) is expressed in terms of impact parameter b, defined by

$$L = \left(\ell + \frac{1}{2}\right)\hbar \equiv bp = b\hbar k \tag{4}$$

where L is the angular momentum of the partial wave. At high energies there are many partial waves and the sum in equation (2) is approximated as an integral.

$$a = \frac{1}{ik} \int_0^\infty d\left(\ell + \frac{1}{2}\right)\left(\ell + \frac{1}{2}\right) P_\ell(\cos\theta)(1 - S_\ell) \tag{5}$$

For ℓ large and θ small the Legendre function (the continuous extension of the Legendre polynomials) is approximated by

$$P_\ell(\cos\theta) \cong J_0(\ell \sin\theta) \tag{6}$$

where J_0 is the zeroth order Bessel function and equation (5) is expressed as an integral over impact parameter b.

$$a \doteq \frac{k}{i} \int_0^\infty bdb\, J_0(bk \sin\theta)(1 - S(b)) \tag{7}$$

Using the identity

$$J_0(x) = \frac{1}{2\pi} \int_0^{2\pi} e^{ix\cos\phi}\, d\phi \tag{8}$$

equation (7) can be put in the form of a two dimensional Fourier transform

$$a = \frac{k}{i2\pi} \int d^2\vec{b}\, e^{i\vec{q}\cdot\vec{b}}\, (1 - S(b)) \tag{9}$$

where the two dimensional momentum transfer $\vec{q}$ makes angle ϕ with $\vec{b}$.

In the center of mass frame the energy component of the four momentum transfer vanishes. If θ is small then $q_z \cong 0$ so that

$$-t = -(0, q_x, q_y, 0)^2 = q^2 = k^2 \sin^2\theta$$

For a purely absorptive reaction $S(b)$ is real. Equation (9) can also be derived (in the same limit of high energy and small scattering angles by adding the spherical waves emanating from an opaque object placed in the path of a plane wave, where $S(b)$ is the transmission coefficient at impact parameter b. The form of $S(b)$ can be chosen in several ways. For example, the choice

$$\begin{aligned} S(b) &= 0 \qquad & b < b_0 \\ S(b) &= 1 \qquad & b > b_0 \end{aligned} \tag{10}$$

yields the black disk model with differential cross section given by

$$\frac{d\sigma}{dt} = \pi \frac{b_0^2}{|t|} J_1^2(b_0 \sqrt{-t}) \tag{11}$$

The form proposed by Chou and Yang is

$$S(b) = e^{-\mu\Omega(b)} = e^{-2\pi\mu \int d^2\vec{q}\; e^{i\vec{q}\cdot\vec{b}}\; F_1(q^2)\, F_2(q^2)} \tag{12}$$

Here $F_1(q^2)$ and $F_2(q^2)$ are the form factors of the interacting particles. This choice, first proposed in 1968, was motivated by

the following observations:

1) The form of the proton-proton differential cross section was approaching (as $s \to \infty$) a form approximately (but not exactly) proportional to the fourth power of the proton form factor. Furthermore, the total cross sections of the various hadron-hadron reactions appeared to be approaching constants asymptotically as $s \to \infty$, and the ratio of the real part of the scattering amplitude to the imaginary part (as determined by studying the differential elastic cross section in the Coulomb interference region $-t \cong 0.01\ \mathrm{GeV}/c^2$) was approaching zero asymptotically.

2) Since hadrons have a finite size, corrections for the shielding of the back of the target by the front are important.

These observations led Chou and Yang to assume that the scattering was (in the high energy limit) due to purely absorptive effects.

For a point probe, the transmission coefficient is $S(b) = e^{-\mu D(b)}$ where $D(b)$ is the thickness of the target. If $\rho(x, y, z)$ is the distribution of nuclear matter, then the amount of nuclear matter that a point particle traveling along z encounters is

$$D(x, y) = \int_{-\infty}^{\infty} dz\ \rho(x, y, z) \tag{13}$$

For a diffuse probe, the opacity at impact parameter $\vec{b}$ is defined as

$$\Omega(\vec{b}) = \int d^2\vec{b}_1 \, D_1(\vec{b} - \vec{b}_1) \, D_2(\vec{b}_1) \tag{14}$$

and the form of $S(b)$ as prescribed above

$$S(\vec{b}) = e^{-\mu\Omega(\vec{b})} \tag{15}$$

The parameter μ represents the interaction strength and is the only free parameter of the model. It is determined by the total cross section of the reaction and the optical theorem.

$$\left.\frac{d\sigma}{dt}\right|_{t=0} = \frac{\sigma_{tot}^2}{16\pi} \tag{16}$$

The last step in the model is to relate the nuclear matter densities to the form factors. The assumption is made that the nuclear densities are the same as the charge densities. The form factor is the three dimensional Fourier transform of the charge distribution [22]

$$F(q^2) = \frac{1}{(2\pi)^{3/2}} \int d^3\vec{b} \; \rho(\vec{b}) \; e^{i\vec{b}\cdot\vec{q}} \tag{17}$$

If the scattering angle θ, is small then the z component of the momentum transfer q can be neglected as above and the z integration in equation (14) performed.

$$F(q^2) = \frac{1}{(2\pi)^{3/2}} \int d\vec{b}^2 \; e^{i\vec{b}\cdot\vec{q}} \; D(b_x, b_y) \tag{18}$$

Inverting equation (18) gives:

$$D(b_x, b_y) = \frac{1}{(2\pi)^{1/2}} \int d^2\vec{q}\, e^{-i\vec{b}\cdot\vec{q}}\, F(q^2) \tag{19}$$

If the Fourier transform of x is denoted $\langle x \rangle$ and the convolution of equation (14) is expressed as

$$\Omega(b) = 2\pi D_1 \otimes D_2 \tag{20}$$

then the expression for the scattering amplitude becomes

$$a = \frac{k}{i} \langle 1 - e^{-\mu\Omega(\vec{b})} \rangle \tag{21}$$

where

$$\Omega(\vec{b}) = (2\pi)^2 \langle F_1 \rangle \otimes \langle F_2 \rangle \tag{22}$$

Equations (21), (22) and (1) with free parameter μ specified by equation (16) give a complete statement of the Chou-Yang model. The convolution theorem can be used to express (16) as

$$\Omega(\vec{b}) = (2\pi)^2 \langle F_1 F_2 \rangle \tag{23}$$

The model can be inverted and the measured cross section used to calculate the product of the form factors

$$F_1 F_2 = \frac{-1}{(2\pi)^2 \mu} \left\langle \ln\left(1 - \frac{i}{k} \langle a \rangle\right) \right\rangle \tag{24}$$

B. Elastic scattering and QCD

QCD calculations to first order in perturbation theory result in a large number of diagrams because of the constituent nature of hadrons. Furthermore, these results are put in doubt because of the large size of α_s, the strong interaction coupling constant. The effects of higher order diagrams may be important. Nevertheless, it has been possible to extract some elastic scattering predictions from this theory in the kinematic range.

Reference (23) has shown that dimensional counting rules may be derived from QCD. These rules were first formulated independently of QCD from dimensional arguments alone.[24] The dimensional counting rule, of interest here, is that for the t dependence of the form factor

$$F(t) \propto t^{1-n} \quad , \quad -t \to \infty \tag{25}$$

where n is the number of constituents in the particle. When similar arguments are applied to the elastic scattering of hadrons the following is predicted:

$$\frac{d\sigma}{dt} \propto \frac{1}{s^2} t^{-6} f\left(\frac{t}{s}\right) \quad , \quad -t,\ s \to \infty \ \text{(meson-baryon)} \tag{26}$$

$$\frac{d\sigma}{dt} = \frac{1}{s^2} t^{-8} f\left(\frac{t}{s}\right) \quad , \quad -t,\ s \to \infty \ \text{(baryon-baryon)} \tag{27}$$

In general $f(t/s)$ is too complicated to be calculated in the region

appropriate to this experiment ($t, s \to \infty$, $-t \ll s$). At fixed angle, however, i.e. fixed $\frac{t}{s} \cong \frac{1}{2}(1 - \cos\theta)$, these rules predict cross sections with energy dependence of s^{-8} and s^{-10}. In reference[23] the dominant contributing diagrams are ones like that shown in figure 2.2. These are the hard scattering diagrams which are characterized by being connected. That is, all parts of the diagram are joined.

A rival mechanism, first described by Landshoff,[25] is depicted in figure 2.3. In these diagrams the quark lines are disconnected if the hadron vertices are removed. These diagrams lead to energy independent contributions to the cross section with angular dependence t^{-7} and t^{-8} for meson-baryon and baryon-baryon scattering, respectively. There are more hard scattering diagrams, but the Landshoff mechanism leads to differential cross sections which are independent of s. Hence this mechanism may become important at large s. The cross section is not independent of s until beam energies of 500 GeV/c but at higher energies the data have a t dependence consistent with the Landshoff mechanism (figure 2.4). There is some doubt, theoretically, as to whether the Landshoff mechanism is suppressed by higher order corrections to the diagrams.[23] Also, because the relative contributions of the hard scattering and the Landshoff mechanism depend on the addition of a large number of diagrams it is now known a priori at what s and t

the Landshoff behavior should dominate in pion-proton scattering (or if it ever is a dominant contribution at all).

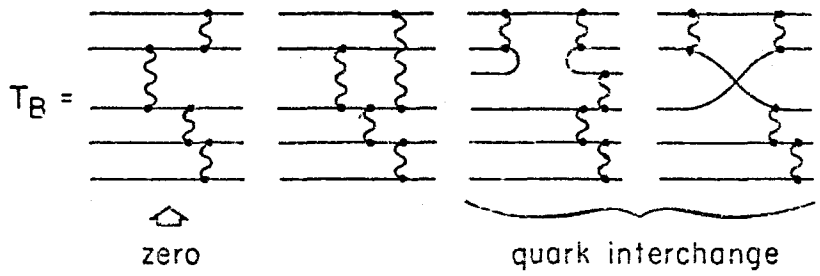

Figure 2.1. Example of QCD diagrams for meson-proton scattering. This figure is reproduced from reference 27.

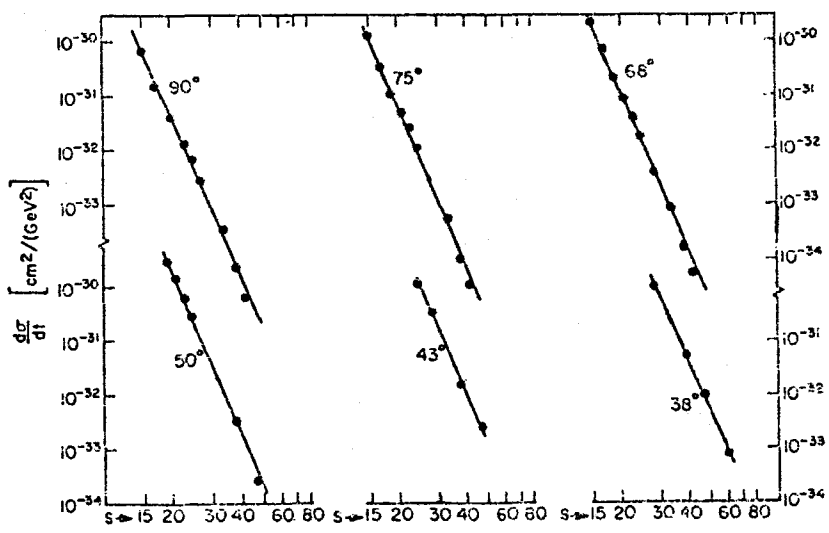

Figure 2.2. Elastic pp scattering at fixed θ. The best overall fit is $s^{-9.7 \pm 0.5} f(t/s)$. This figure is reproduced from reference 28.

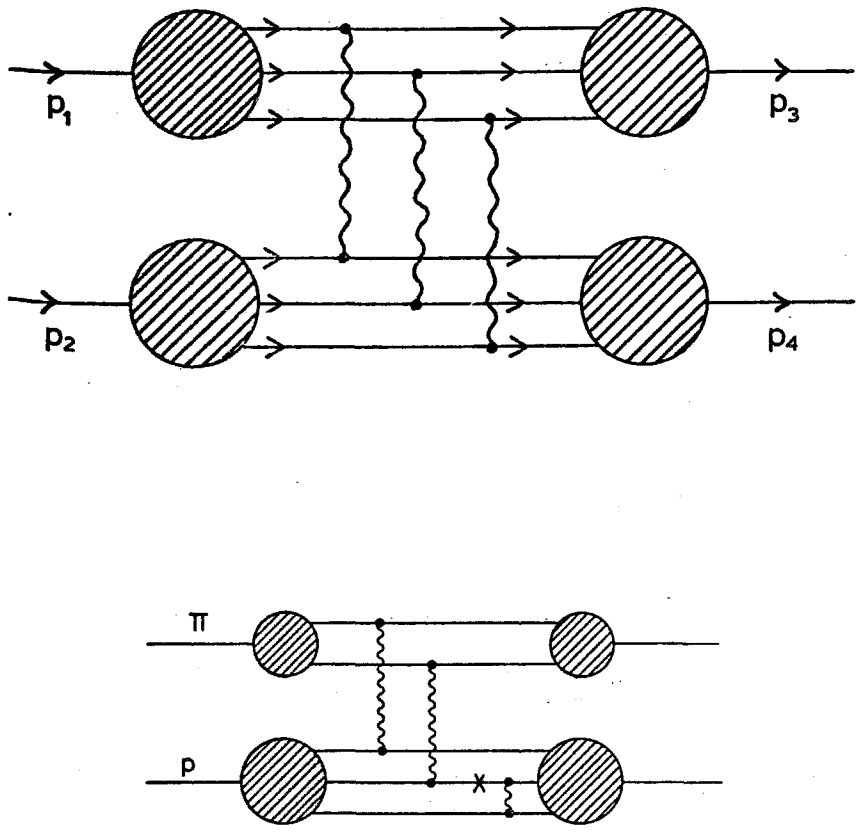

Figure 2.3. Leading diagrams contributing to the Landshoff mechanism for pp scattering (above) and πp scattering (below). This figure is reproduced from reference 25.

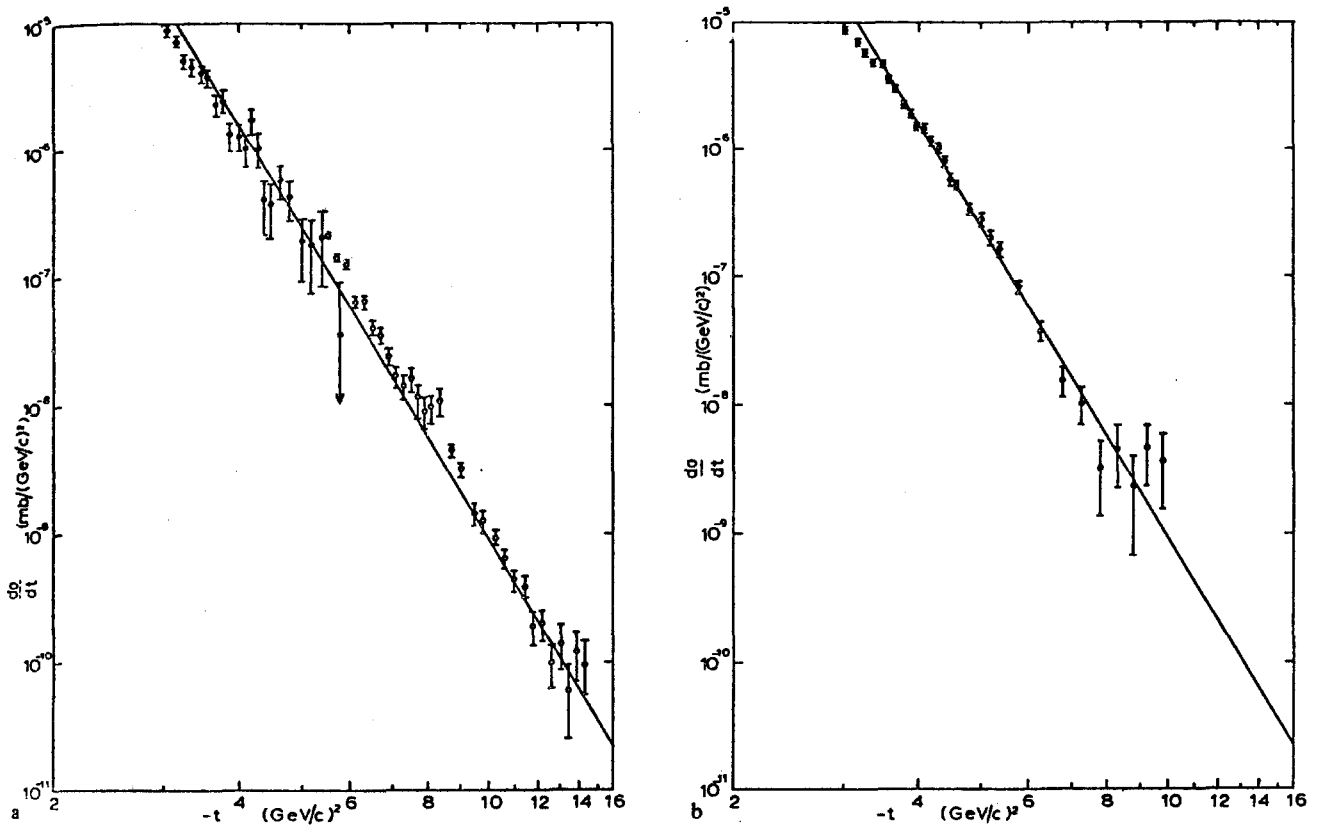

Figure 2.4. Proton-proton elastic differential cross section at equivalent laboratory incident momentum near 500 GeV/c (a), and 1500 GeV/c (b). This figure was reproduced from reference 25. The lines are $d\sigma/dt = 0.09\ t^{-8}$.

III. Experimental Apparatus

The experimental apparatus is shown in figures 3.1-3.3 and described in detail in Appendices 1 through 8. The experiment measures the differential cross section of the reactions

$$H + p \rightarrow H + p$$

at incident beam moments of 100 and 200 GeV/c. The incident beam hadrons (H) are protons, pions, kaons and their antiparticles. The detector was sensitive to events with sqared four momentum transfer in the range

$$0.9 < -t < 11.0 \ (\mathrm{GeV}/c)^2 \quad \text{at 200 GeV/c}$$

and

$$0.4 < -t < 3.0 \ (\mathrm{GeV}/c)^2 \quad \text{at 100 GeV/c}$$

For the reaction of primary interest, $\pi^- p$ at 200 GeV/c, the total cross section is 24 mb.[14] At low values of -t, the elastic cross section depends exponentially on t (approximately as e^{9t}) and elastic scattering contributes only 13% to this total cross section.[1] Thus the rate of elastic events in the t range of this experiment is several orders of magnitude lower than the total reaction rate.

This small rate required that the experiment have high luminosity. This was accomplished by having about 8×10^6 particles per accelerator spill traverse a 1 meter liquid hydrogen target giving a luminosity of 34 inverse microbarns per accelerator spill. The

beam was defined by a fast coincidence between the scintillation counters B1 and B2 (see figure 3.1). Approximately 10% of the beam interacted with the protons in the target. The production and transport of the beam are described in Appendix 1. The hydrogen target is described in Appendix 4.

The small ratio of the high -t elastic cross section to the total cross section required that the experiment have both fast and efficient rejection of unwanted (inelastic and low -t) events.

The efficient rejection was achieved by kinematic selection made possible by the use of proportional wire chambers (Appendix 6) with precise space resolution ($\sim$ 2 mm) but poor time resolution ($\sim$ 100 ns). These proportional wire chambers were deployed in two spectrometers (Appendix 5) which measured the vector momenta of the scattered hadron and the recoil proton. A similar measurement of the beam particle momentum was impractical because of the high beam rate.

The trajectory and momentum of the scattered hadron was measured in the forward spectrometer (figure 3.2) and was close to that of the beam particle. That spectrometer contained two magnets which deflected the hadron about 10 mr toward the beam axis. Proportional wire chambers were used to measure the trajectory of the hadron before and after this deflection. This system measured the forward scattering angle with a resolution of 35 microradians and

the forward momentum with a resolution of 0.45 GeV/c (at 100 GeV/c) or 0.91 GeV/c (at 200 GeV/c). The trajectory and momentum of the recoil proton were determined by the recoil spectrometer (figure 3.3). This momentum ranged from 1 to 10 GeV/c. The spectrometer consisted of an analyzing magnet bracketed by proportional wire chambers. The magnet deflected the recoil proton towards the beam axis. The recoil scattering angle was measured with resolution of 1.4 mr and the momentum with resolution of

$$\frac{\delta p}{p^2} = 0.01\ (\mathrm{GeV/c})^{-1} .$$

For fast rejection of unwanted events the experiment incorporated scintillation counters (Appendix 4) with fast time resolution ($\sim$ 5 ns) but poor spatial resolution ($\sim$ 10 cm). Four scintillation counter hodoscopes, located in the spectrometers, detected the forward scattered hadron and the recoil proton. The experiment trigger (Appendix 8) consisted of a suitable coincidence between the beam counters and these spectrometer hodoscopes. Only hodoscope signal combinations that were consistent with elastic event trajectories were used in the trigger. The target was covered on three sides by anticoincidence counters which vetoed inelastic events and elastic events which had an azimuthal orientation to which the spectrometers were insensitive. A potential trigger was vetoed by either one or more of the target anticoincidence counters or the detection

of two or more charged particles in any of the spectrometer hodoscopes.

The hadron was identified with a differential Cerenkov counter (CB) located in the beam and a threshold Cerenkov counter (CF) located in the forward spectrometer (Appendices 2 and 3). During any one run, the beam counter CB was set to "tag" one type of beam particle. The threshold counter was always set so that it was insensitive to protons. The absence of a signal in CF identified the scattered hadron as a proton or antiproton. At incident beam momenta of 100 GeV/c, separation between pions and kaons was obtained from the pulse height of the signal in CF.

Upon occurrence of a trigger, the state of the detector elements was read through a CAMAC interface into an on-line computer and then written to magnetic tape. This information was then processed by an off-line computer as described below.

Figure 3.1. Beam apparatus and forward spectrometer.

m6b3e-m6v8v	beam line magnets
CB	beam differential Cerenkov counter
1-2	proportional wire chambers (PWCs) b1x and b2y
B1	beam scintillation counter
Hx	beam hodoscope
B2	beam scintillation counter
A1	beam halo veto counter
T	liquid hydrogen target
M2, M3	forward spectrometer analysis magnets
CF	threshold Cerenkov counter
Z	beam axis and z axis of the forward spectrometer
Z_d	path of unscattered beam during data taking
He	helium bags

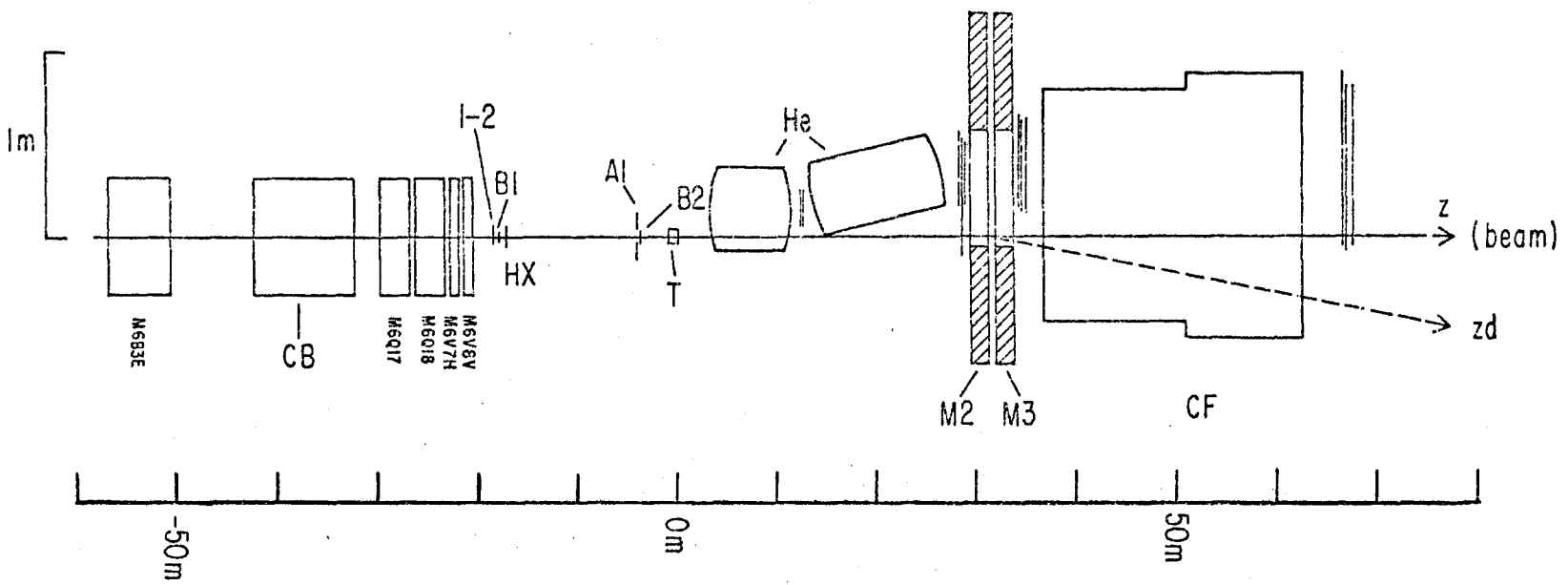

Beam Apparatus and Forward Spectrometer
(Plan View)

Figure 3.2. Forward and recoil spectrometers.

T	liquid hydrogen target
x	x axis of forward coordinate system (the y axis points out of the page)
1-4	PWCs F1x-F4x (only the sensitive region of the PWCs is drawn)
5-10	PWCs F5x-F10y
M2, M3	forward spectrometer analysis magnets
11-13	PWC's F11x-F13x
H3	forward trigger hodoscope
CF	threshold Cerenkov counter
14-16	PWCs F14x-F16x
H4	forward trigger hodoscope
H1	recoil trigger hodoscope
M1	recoil spectrometer magnet
H2	recoil trigger hodoscope

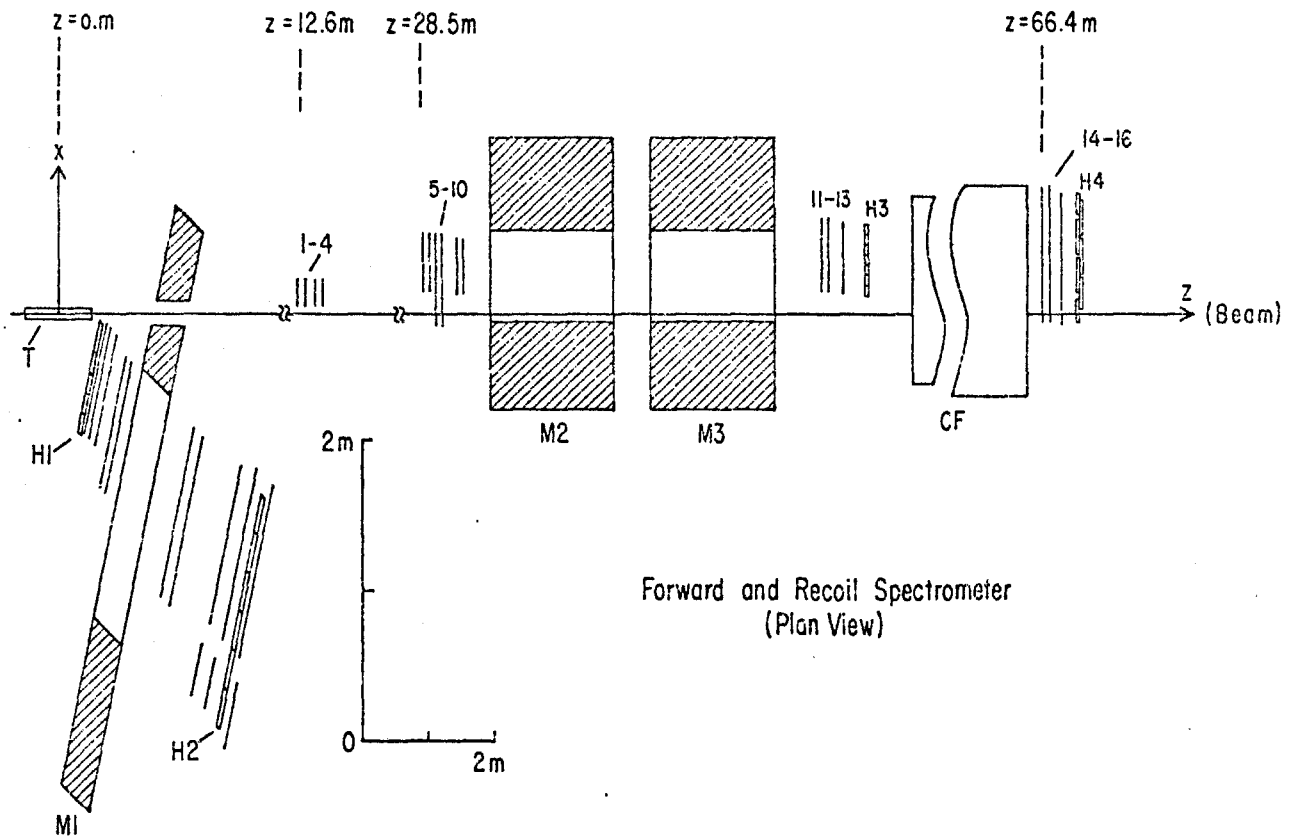

Forward and Recoil Spectrometer
(Plan View)

Figure 3.3. Recoil spectrometer.

T	liquid hydrogen target
x, z	forward coordinate system
x', z'	recoil coordinate system (the angle between the two coordinate systems is 25 degrees)
H1	recoil trigger hodoscope
1-13	PWCs r1x - r13y
M1	recoil analysis magnet
H2	recoil trigger hodoscope

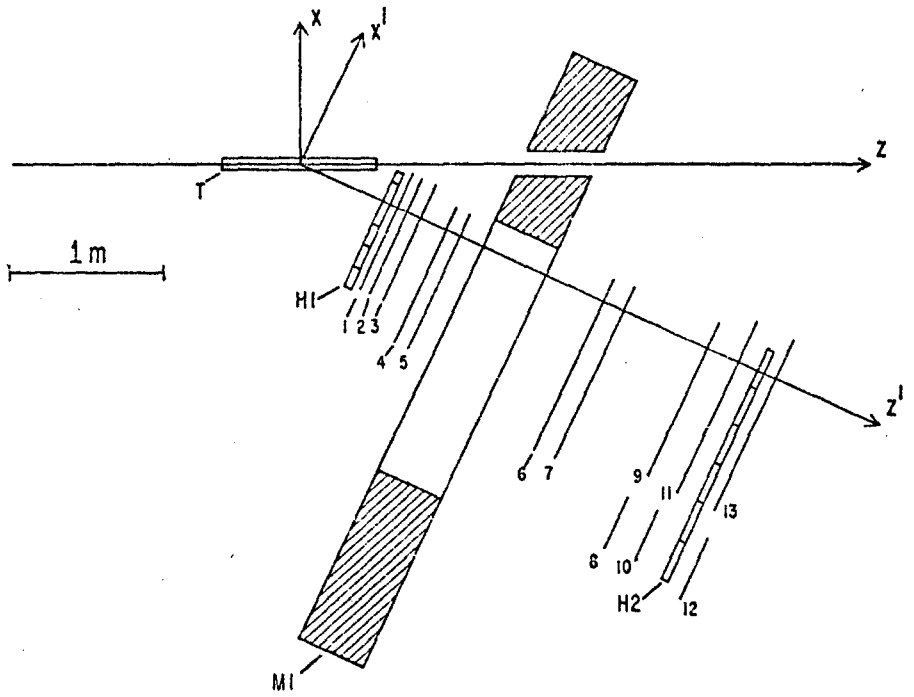

Recoil Spectrometer (Plan View)

IV. Data Reduction

The first step in reducing the data stored on magnetic tape to cross sections was to reconstruct the particle trajectories of each event. Once this was done, a set of seven criteria was used to determine if the event should be included in the elastic sample.

Three of these criteria were geometrical: the reconstructed trajectories should meet in the hydrogen target and the trajectories through each spectrometer should be continuous. The remaining four criteria were kinematic and corresponded to conservation of four-momentum in the two particle system. Because there were extraneous cluster coordinates in the wire chambers, it was possible to reconstruct approximately 50% of the events in more than one way. To remedy this problem the event selection was done in two passes. In the first pass possible reconstructions were identified and loose criteria were applied. Next small changes were made to the analysis constants to center the kinematic and geometrical distributions. These changes were necessary because of small deviations of the proportional wire chamber positions and incident beam angle. Final cuts were made at approximately three standard deviations. Finally, fiducial cuts were applied to eliminate events near the edges of the apparatus and events which originated from the hydrogen target flask ends. Accepted events were separated by incident beam particle on the basis of the Cerenkov counter data.

To calculate the detection efficiency of the apparatus, as determined by the selection criteria and spectrometer geometry, a Monte Carlo computer program was used to simulate the response of the apparatus to elastic events. The simulated events were processed with the same analysis programs as the real data.

Cross sections were calculated from the real event t distributions, the Monte Carlo efficiency and the incident beam flux. The incident beam flux was defined as the number of incident beam particles defined as the number of B1, B2 coincidences weighted by the fraction of each particle in the beam as measured by the differential Cerenkov counter (CB) during special runs. Corrections were made for the small background under the kinematic signals, imperfect particle separation, measurement resolution of t and counting losses at high rate. Details of the data reduction may be found in Appendices 10-12.

V. Results

The measured cross sections are listed in Tables 5.1 to 5.4 and plotted in figures 5.1-5.12 where they are compared with the lower -t measurements of reference 1. Not all data points of reference 1 have been plotted to ensure clarity of the figures. The well measured pp cross section is plotted along with data from three other references. Bins which contain no events are quoted with an error corresponding to the cross-section if one event had been observed in the bin. The errors quoted are statistical only. The statistical error in the acceptance has been added in quadrature with the statistical error of the data. The estimated overall normalization errors are tabulated in Table 5.5. These errors are due to the uncertainty in the corrections mentioned previously.

As seen in figure A5.4 the 200 GeV/c pp data agree both in form and normalization with the measurements of references 1-3. At 100 GeV/c there is some additional uncertainty in the first few ($-t < 0.8$ $(GeV/c)^2$) bins. (The 200 GeV/c measurements start at $-t = 0.9$ $(GeV/c)^2$.) This is attributed to the uncertainty in the efficiency of the recoil spectrometer.

The largest contribution to the overall normalization error was due to the extrapolation of the event yield per incident beam particle to low intensity. This correction, described in Appendix 12 was typically 5-30%. The error in this correction was largest for

the $\pi^- p$ data. Even within this error the -200 GeV/c $\pi^- p$ data appear low with respect to the data of reference 1. The 200 GeV/c $\pi^+ p$ and $\pi^- p$ are equal within the normalization errors quoted in Table A5.5, however. This follows a trend observed at lower -t where the particle and antiparticle-proton cross sections are approximately equal. The data of reference 1 agree with this postulate over most of the range of t but the $\pi^- p$ data is slightly higher than the $\pi^+ p$ data in the last (high -t) bins. A change in the slope of the cross section between low -t and higher -t precludes a comparison of normalization with the data of reference 9.

The 200 GeV/c $\pi^- p$ cross section falls 8 decades from $-t = 0$ to $-t = 3.8\ (\mathrm{GeV/c})^2$. There is a dip in the vicinity of $-t = 3.8\ (\mathrm{GeV/c})^2$ followed by a secondary maximum at $-t = 5.5\ (\mathrm{GeV/c})^2$. At larger values of -t the cross section falls more slowly than in the low -t region. Figure 5.13 shows that the background is small everywhere. In the region of the dip the elastic signal is small, however, when compared to the background. All of these cross sections display a change of slope between the beginning of the diffraction peak and higher -t. The measurements of the $\pi^- p$ cross section at 100 GeV/c and $\pi^+ p$ cross section at both 100 and 200 GeV/c do not extend to values of -t beyond $3.4\ (\mathrm{GeV/c})^2$.

The 200 GeV/c $\bar{p}p$ cross section has low statistics but the data in the high -t region are consistent with an enhancement of the

cross section in this region. A dip bump structure in the $\bar{p}p$ cross section has recently been observed at incident momentum of 50 GeV/c.[11] This experiment's 100 GeV/c $\bar{p}p$ cross section is consistent with a dip at $-t = 1.4\ (\mathrm{GeV}/c)^2$. The $K^{\pm}$ cross sections show a slightly wider diffraction peak then the pion diffraction peak. This corresponds to the kaon radius being slightly smaller than the pion radius.

Table 5.1

Elastic differential cross sections for negative 200 GeV/c beam. t is the bin center expressed in $(GeV/c)^2$. Δt is the bin width. The differential cross section is expressed in $\mu b/(GeV/c)^2$.

t	Δt	σ_{π^-}	$\delta\sigma_{\pi^-}$	σ_{K^-}	$\delta\sigma_{K^-}$	$\sigma_{\bar{p}}$	$\delta\sigma_{\bar{p}}$
.895	.068	30.98	.38	48.	11.	4.8	1.9
.966	.073	22.14	.26	23.3	6.4	1.17	.81
1.042	.080	14.59	.18	23.3	5.6	1.29	.73
1.125	.085	9.48	.13	25.0	5.1	.71	.50
1.214	.093	5.802	.092	10.1	3.0	–	.34
1.311	.102	3.300	.062	4.2	1.7	–	.22
1.417	.109	2.006	.045	2.9	1.3	–	.21
1.531	.119	1.072	.029	4.3	1.5	–	.17
1.655	.130	.596	.019	.84	.60	–	.23
1.793	.146	.336	.013	.32	.32	.094	.095
1.923	.134	.1607	.0082	–	.32	–	.10
2.100	.200	.0669	.0039	.22	.22	.074	.074
2.300	.200	.0264	.0022	.18	.18	.051	.051
2.500	.200	.0107	.0013	–	.19	.040	.039
2.700	.200	.00334	.00068	–	.12	.038	.038
2.900	.200	.00162	.00044	–	.15	–	.028
3.100	.200	.00054	.00025	–	.16	–	.036
3.350	.300	.00014	.00010	–	.077	–	.022
3.650	.300	–	.000070	–	.087	–	.021
4.000	.400	–	.000050	–	.057	–	.016
4.400	.400	.000047	.000047	–	.060	–	.016
4.800	.400	.000187	.000090	–	.056	–	.014
5.500	1.000	.000088	.000040	–	.022	–	.0050
6.500	1.000	.000088	.000040	–	.022	–	.0052
7.500	1.000	–	.000020	–	.020	–	.0049
8.500	1.000	–	.000020	–	.018	–	.0046
9.500	1.000	.000015	.000015	–	.019	–	.0044
10.500	1.000	.000017	.000017	–	.019	–	.0051

Table 5.2

Elastic differential cross sections for positive 200 GeV/c beam.

t	Δt	σ_{π^+}	$\delta\sigma_{\pi^+}$	σ_{K^+}	$\delta\sigma_{K^+}$	σ_p	$\delta\sigma_p$
.895	.068	36.1	1.5	44.0	8.9	10.70	.34
.966	.073	21.60	.93	19.6	4.8	5.37	.19
1.042	.080	14.84	.66	24.5	4.6	2.94	.13
1.125	.085	9.21	.46	13.6	3.1	1.206	.071
1.214	.093	5.81	.33	3.2	1.3	.475	.041
1.311	.102	3.57	.23	5.9	1.7	.141	.020
1.417	.109	2.03	.16	2.6	1.0	.0243	.0074
1.531	.119	.933	.100	1.99	.82	.0241	.0066
1.655	.130	.679	.076	1.20	.55	.0256	.0063
1.793	.146	.219	.039	.43	.31	.0391	.0069
1.933	.134	.193	.038	.65	.38	.0447	.0075
2.100	.200	.054	.015	–	.13	.0493	.0063
2.300	.200	.031	.011	.20	.14	.0202	.0038
2.500	.200	.0143	.0068	.10	.11	.0262	.0041
2.700	.200	.0068	.0046	–	.098	.0197	.0034
2.900	.200	–	.0029	–	.081	.0116	.0025
3.100	.200	–	.0027	–	.087	.0050	.0016
3.350	.300	–	.0017	–	.051	.0100	.0017
3.650	.300	–	.0016	–	.057	–	.00029
4.000	.400	.0011	.0012	–	.037	.00066	.00038
4.400	.400	–	.0011	–	.034	.00042	.00029
4.800	.400	–	.0011	–	.034	.00080	.00040
5.500	1.000	–	.00043	–	.013	–	.000077
6.500	1.000	–	.00043	–	.015	.000080	.000079
7.500	1.000	–	.00039	–	.012	.00015	.00010
8.500	1.000	–	.00036	–	.011	–	.000066
9.500	1.000	–	.00036	–	.012	–	.000065
10.500	1.000	–	.00044	–	.014	–	.000077

Table 5.3

Elastic differential cross sections for negative 100 GeV/c beam.

t	Δt	σ_{π^-}	$\delta\sigma_{\pi^-}$	σ_{K^-}	$\delta\sigma_{K^-}$	$\sigma_{\bar{p}}$	$\delta\sigma_{\bar{p}}$
.447	.035	561.0	6.8	630.	33.	475.	24.
.483	.037	438.5	4.8	475.	24.	403.	19.
.521	.040	361.1	3.9	399.	19.	222.	12.
.563	.043	310.2	3.3	384.	17.	228.	12.
.607	.045	223.9	2.4	262.	12.	125.2	7.6
.654	.050	167.5	1.8	188.8	9.2	92.0	5.9
.706	.053	129.3	1.4	152.4	7.4	48.2	3.8
.761	.058	94.7	1.1	103.3	5.3	31.7	2.7
.821	.061	66.54	.77	89.6	4.6	24.2	2.3
.885	.067	45.48	.54	43.3	2.6	13.6	1.5
.955	.073	29.59	.38	40.5	2.3	6.48	.86
1.030	.078	19.68	.28	25.6	1.7	3.20	.51
1.112	.085	11.95	.18	16.4	1.1	1.13	.23
1.200	.091	7.62	.13	12.41	.92	.45	.14
1.295	.099	4.565	.088	6.41	.59	.106	.060
1.399	.109	2.659	.056	5.01	.49	–	.030
1.512	.117	1.479	.035	1.92	.25	–	.024
1.634	.127	.823	.022	1.80	.23	.022	.022
1.766	.138	.449	.014	.82	.14	.036	.025
1.912	.153	.2193	.0084	.385	.086	.031	.021
2.071	.166	.1074	.0052	.227	.058	.069	.027
2.246	.184	.0471	.0030	.185	.047	.020	.013
2.437	.198	.0149	.0016	.086	.030	.017	.011
2.644	.216	.00658	.00097	.029	.016	.037	.016
2.868	.232	.00344	.00096	.018	.017	.040	.022

Table 5.4

Elastic differential cross sections for positive 100 GeV/c beam.

t	Δt	σ_{π^+}	$\delta\sigma_{\pi^+}$	σ_{K^+}	$\delta\sigma_{K^+}$	σ_p	$\delta\sigma_p$
.447	.035	634.	17.	671.	71.	751.	23.
.483	.037	506.	13.	473.	48.	608.	18.
.521	.040	389.3	9.8	322.	36.	422.	13.
.563	.043	340.3	8.3	414.	37.	321.	10.
.607	.045	243.3	6.2	174.	20.	187.1	6.9
.654	.050	175.9	4.5	175.	18.	135.2	5.2
.706	.053	137.9	3.6	160.	16.	73.2	3.3
.761	.058	93.5	2.6	98.	11.	54.1	2.7
.821	.061	73.6	2.1	83.0	9.3	33.6	1.8
.885	.067	45.2	1.4	64.1	6.9	16.9	1.1
.955	.073	28.15	.97	32.9	4.4	8.44	.70
1.030	.078	20.53	.76	27.1	3.7	4.31	.43
1.112	.085	12.76	.52	19.0	2.7	2.41	.28
1.200	.091	8.86	.40	9.3	1.7	.94	.15
1.295	.099	5.30	.28	5.7	1.2	.364	.083
1.399	.109	2.95	.19	5.4	1.0	.073	.033
1.512	.117	1.74	.13	1.65	.53	.107	.037
1.634	.127	1.090	.093	1.35	.43	.092	.031
1.766	.138	.521	.058	.77	.29	.096	.030
1.912	.153	.248	.035	.56	.23	.084	.025
2.071	.166	.151	.025	.078	.080	.079	.022
2.246	.184	.055	.014	.074	.070	.065	.018
2.437	.198	.0322	.0097	–	.055	.037	.012
2.644	.216	.0334	.0092	.055	.051	.0260	.0098
2.868	.232	.0051	.0051	–	.095	.056	.020

Table 5.5

Error in normalization

Beam momentum (GeV/c)	Reaction	Error
-100	$\pi^- p$	8%
	$K^- p$	8%
	$\bar{p}p$	8%
+100	$\pi^+ p$	9%
	$K^+ p$	9%
	$\bar{p}p$ no bar	10%
-200	$\pi^- p$	18%
	$K^- p$	8%
	$\bar{p}p$	27%
+200	$\pi^+ p$	13%
	$K^+ p$	13%
	pp	13%

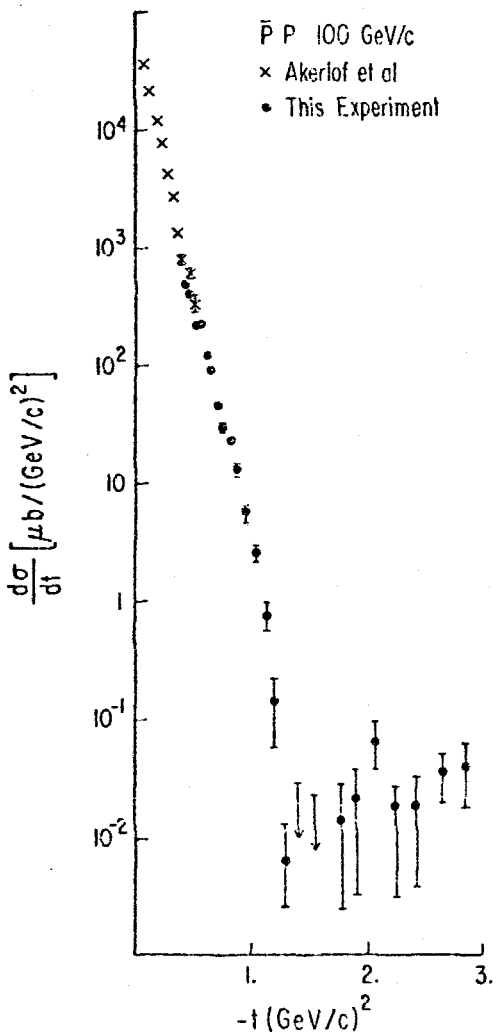

Figure 5.1. 100 GeV/c $\bar{p}p$ elastic differential cross section.

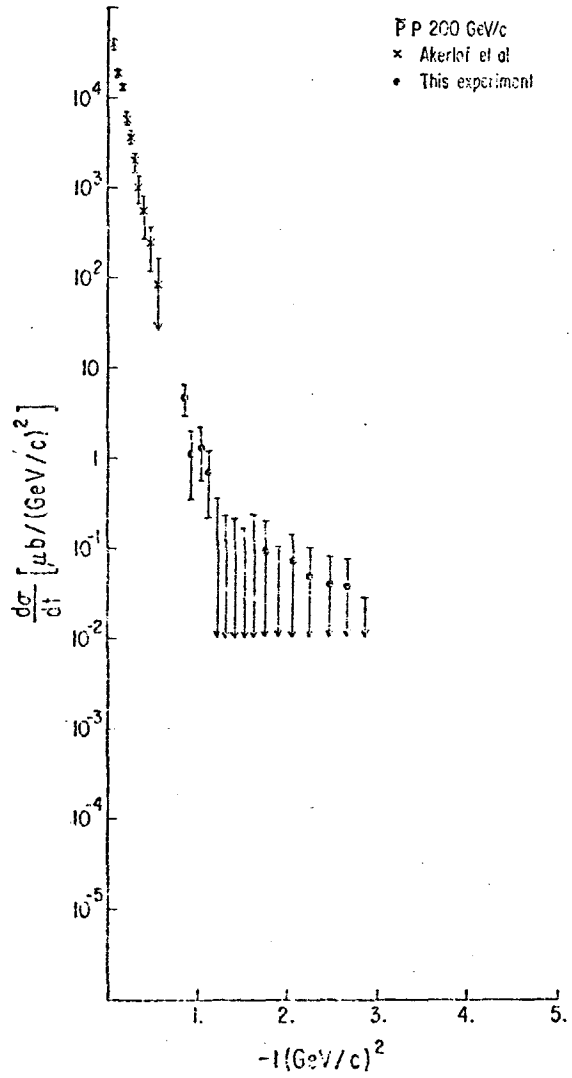

Figure 5.2. 200 GeV/c $\bar{p}p$ elastic differential cross section.

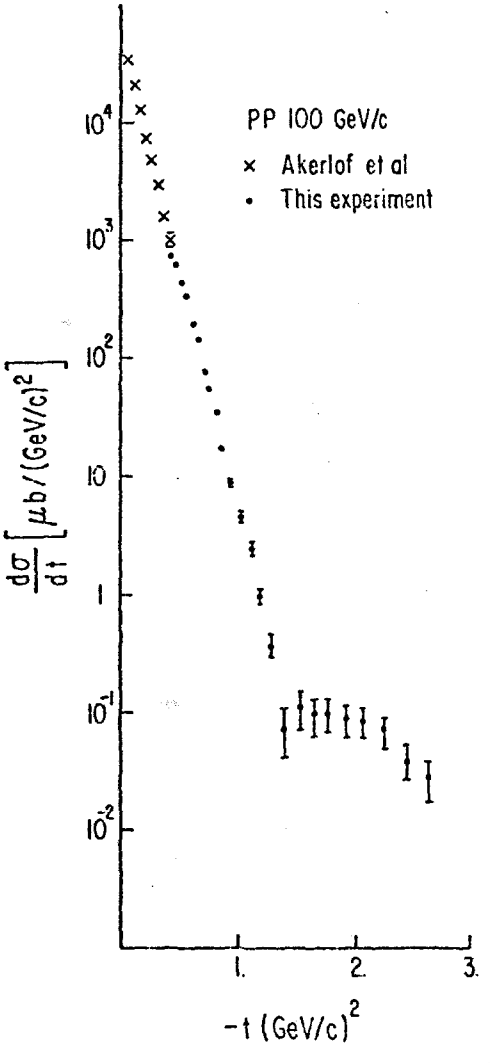

Figure 5.3. 100 GeV/c pp elastic differential cross section.

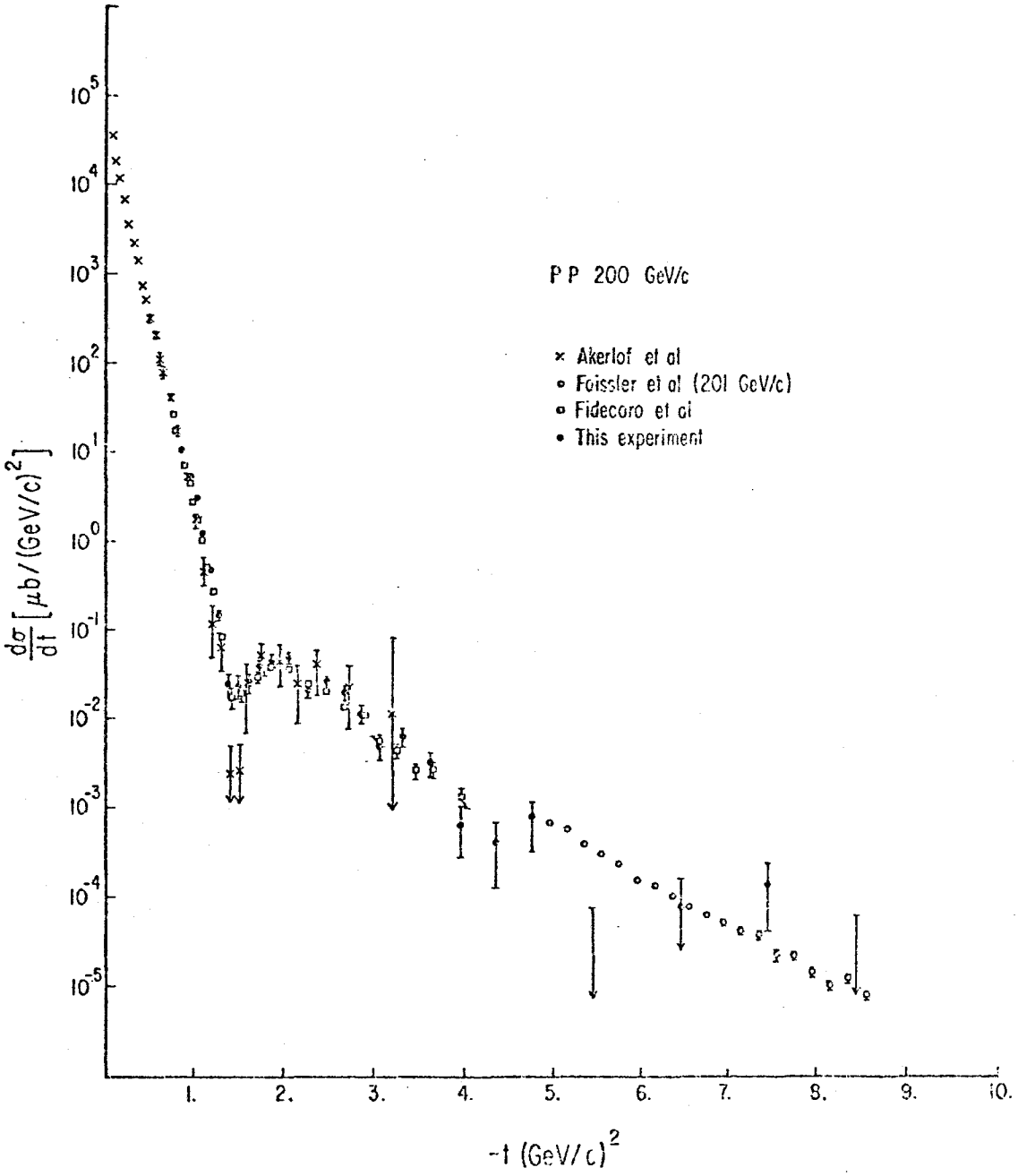

Figure 5.4. 200 GeV/c pp elastic differential cross section.

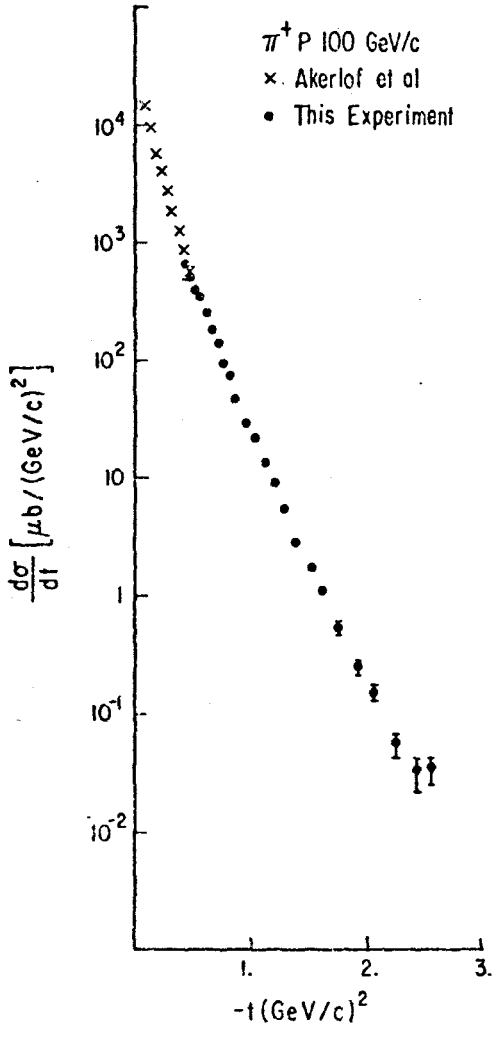

Figure 5.5. 100 GeV/c $\pi^- p$ elastic differential cross section.

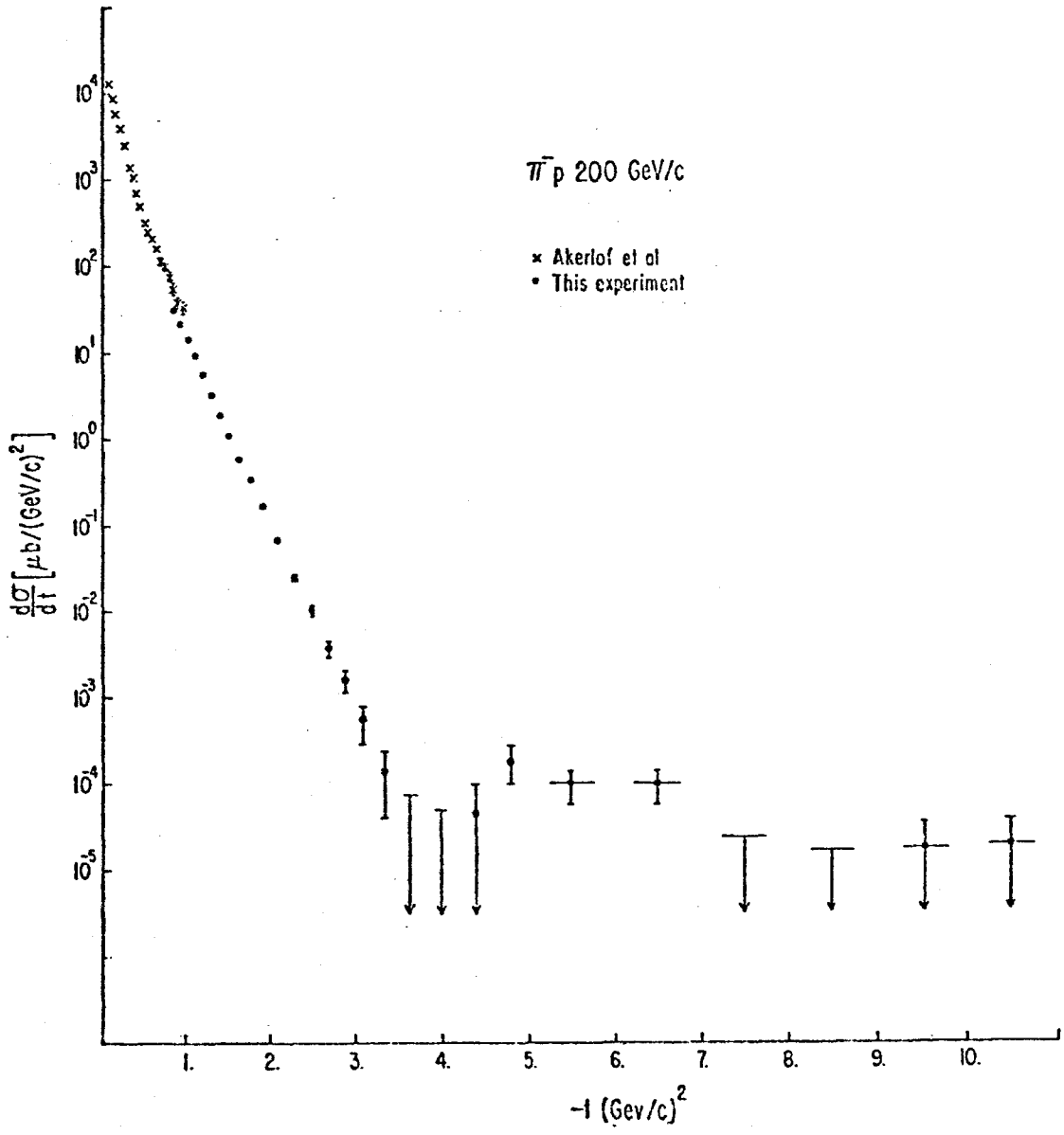

Figure 5.6. 200 GeV/c $\pi^- p$ elastic differential cross section.

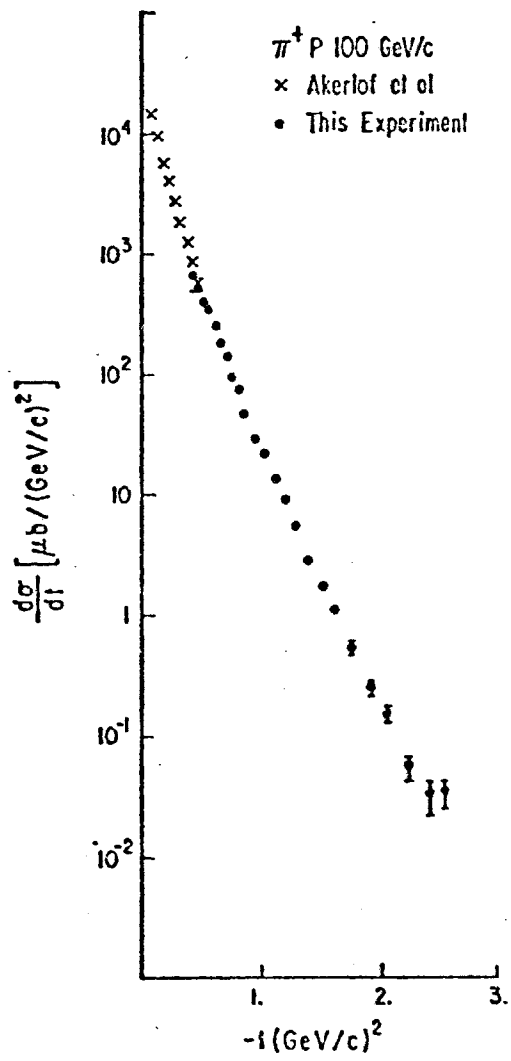

Figure 5.7. 100 GeV/c π^+p elastic differential cross section.

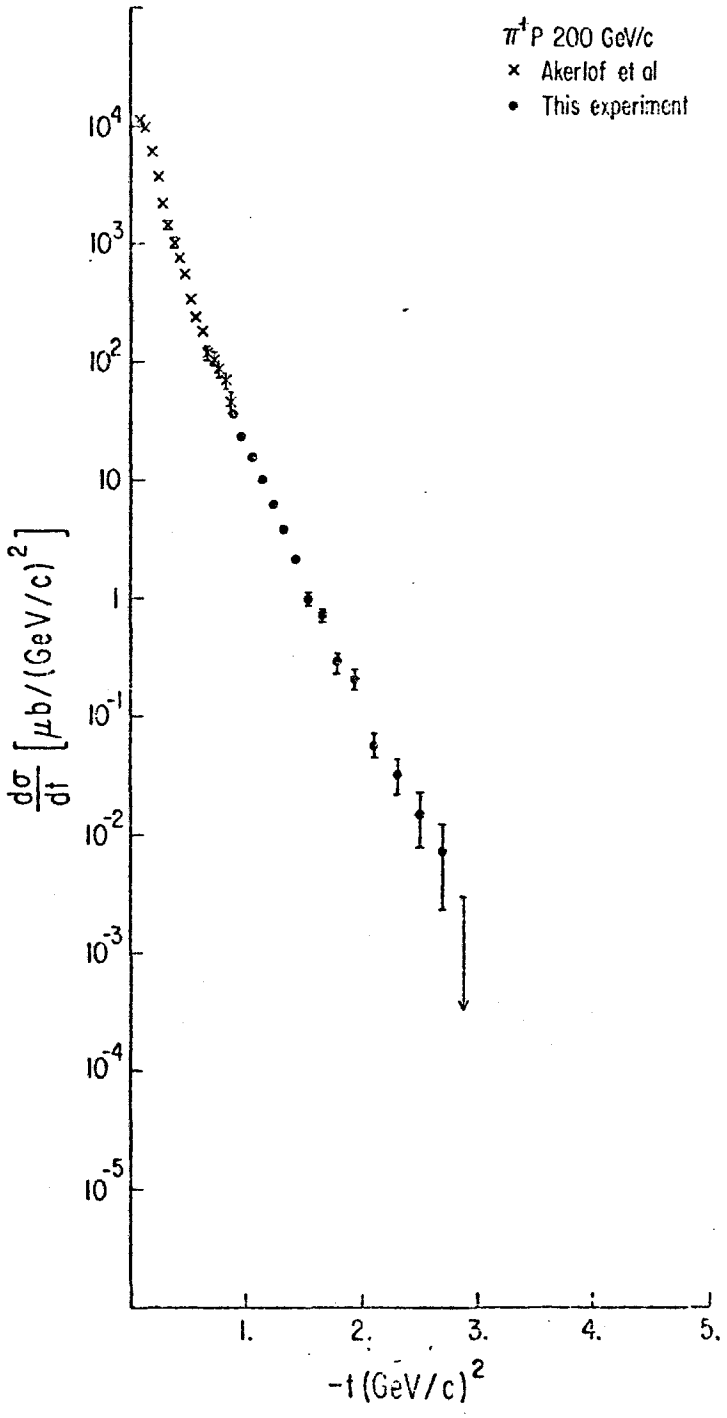

Figure 5.8. 200 GeV/c π^+p elastic differential cross section.

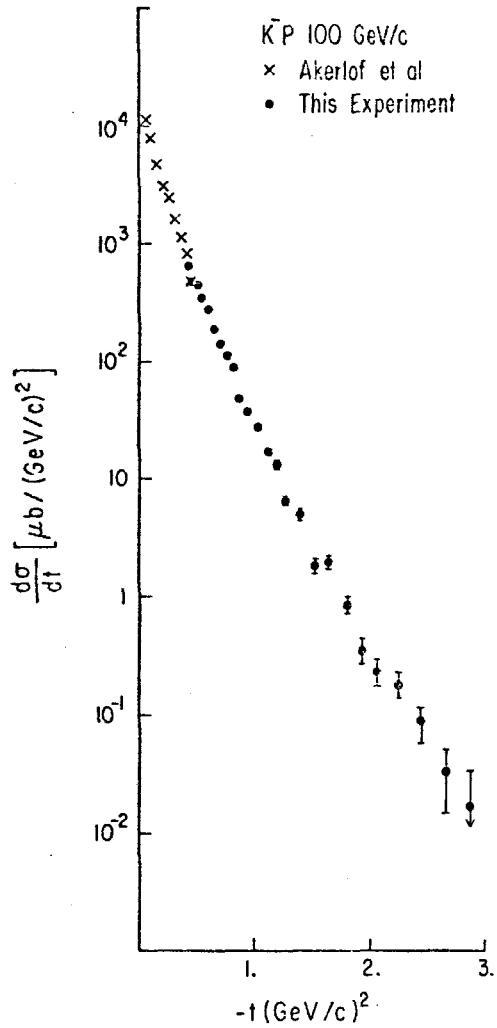

Figure 5.9. 100 GeV/c K^-p elastic differential cross section.

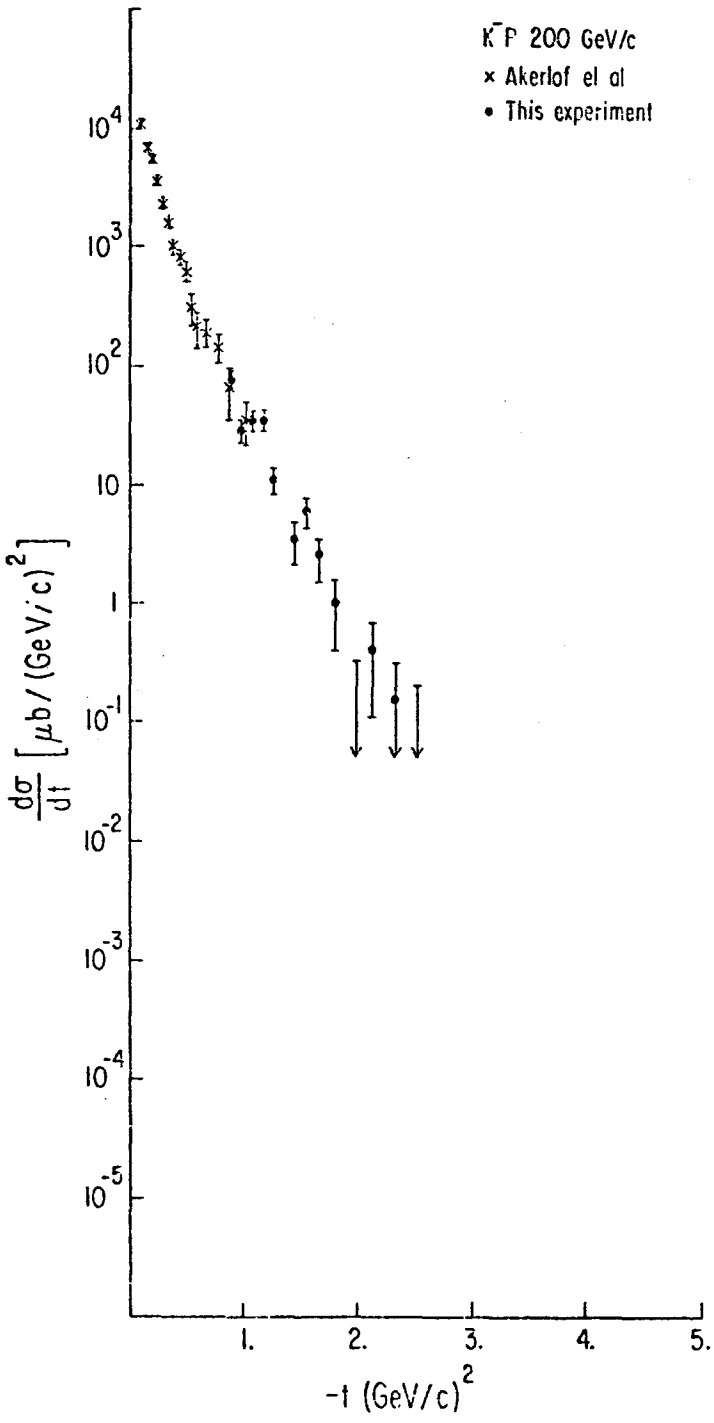

Figure 5.10. 200 GeV/c K^-p elastic differential cross section.

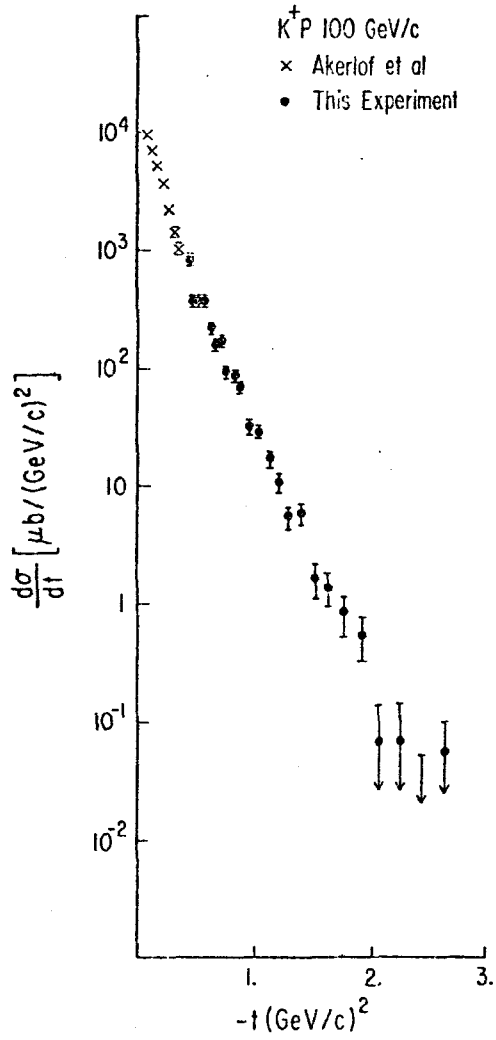

Figure 5.11. 100 GeV/c K^+p elastic differential cross section.

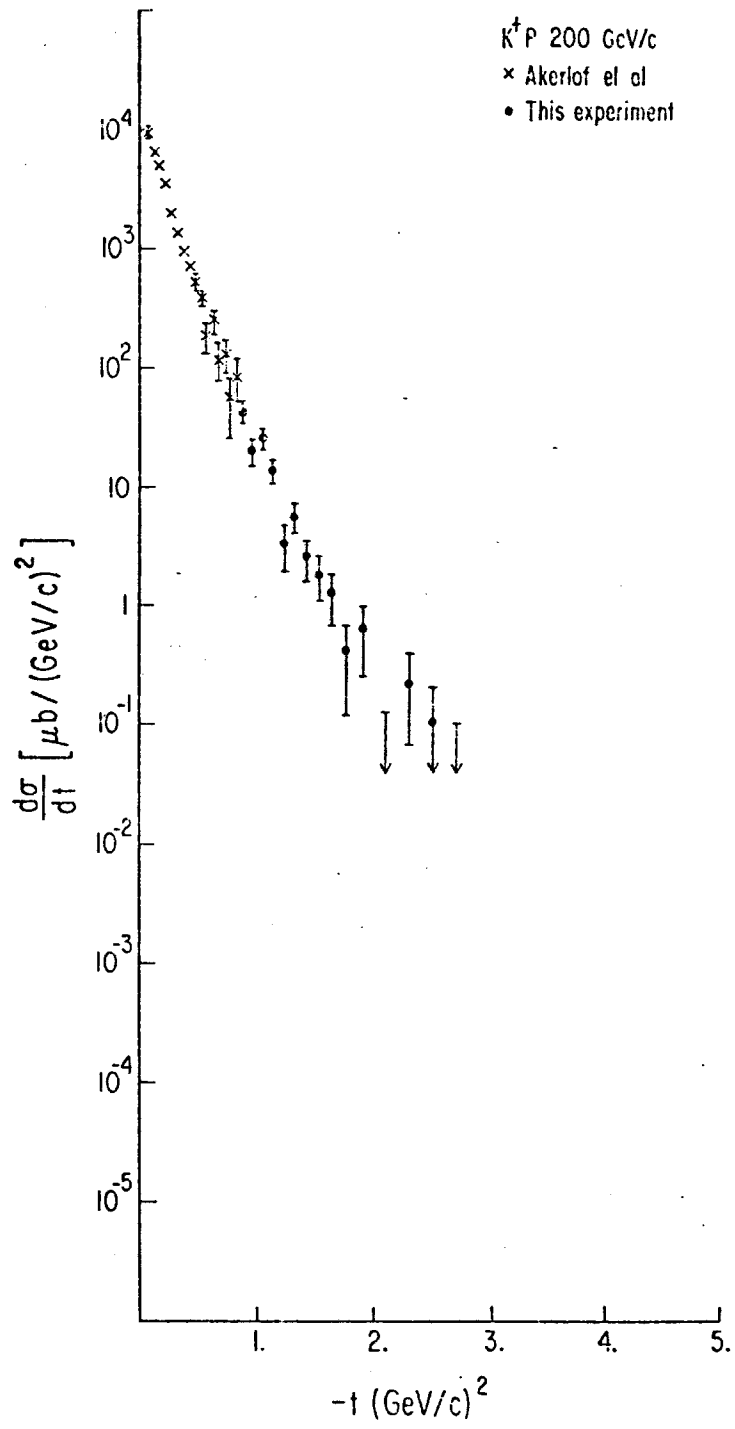

Figure 5.12. 200 GeV/c K^+p elastic differential cross section.

Figure 5.13. The coplanarity elastic signal in four ranges of t.

The data sample is 200 GeV/c πp . The ranges are

a) $1.362 < -t < 1.866$, b) $1.866 < -t < 3.0$,

c) $3.0 < -t < 4.2$, d) $4.2 < -t < 11.5$.

Here -t is expressed in $(\mathrm{GeV}/c)^2$.

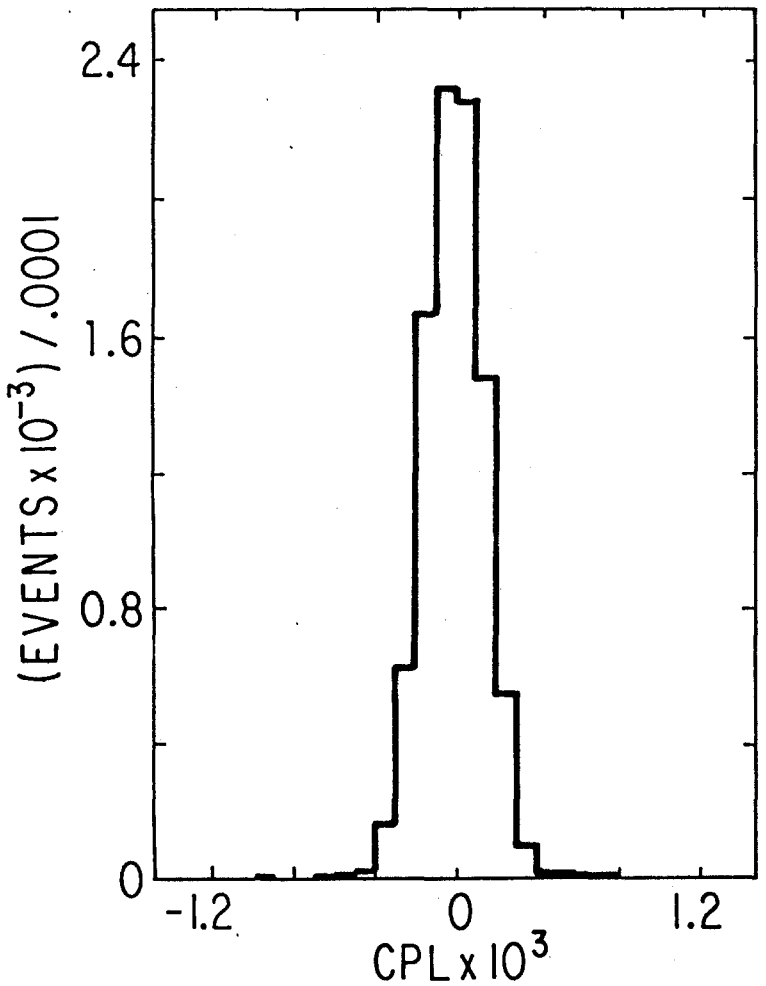

Figure 5.13 (a)

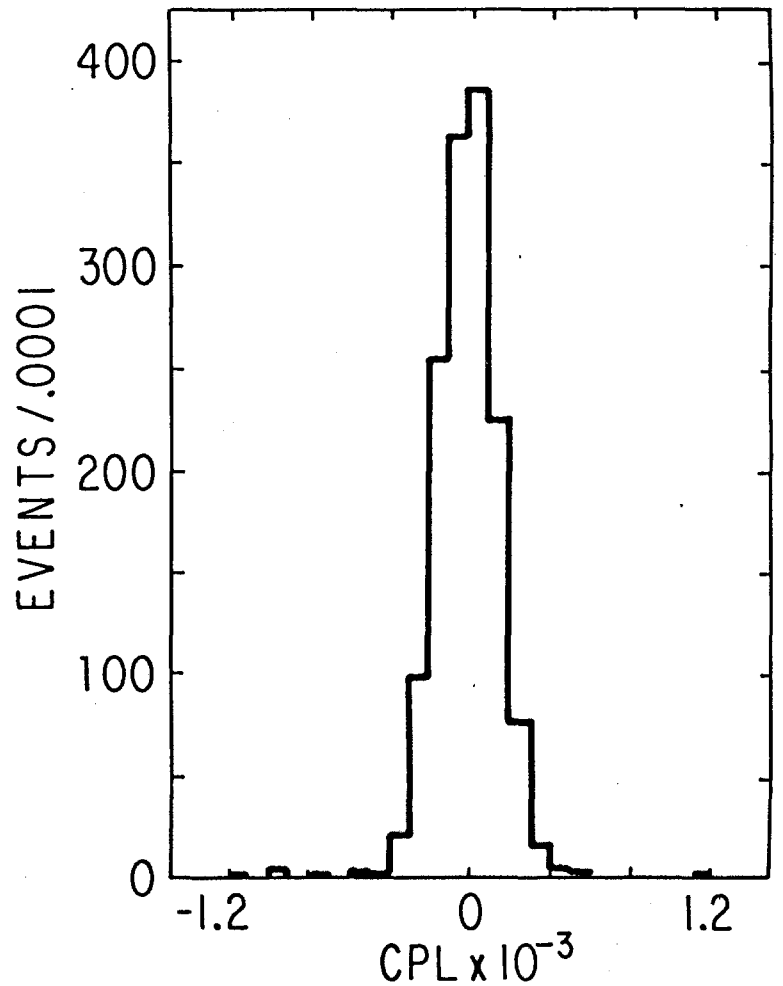

Figure 5.13 (b)

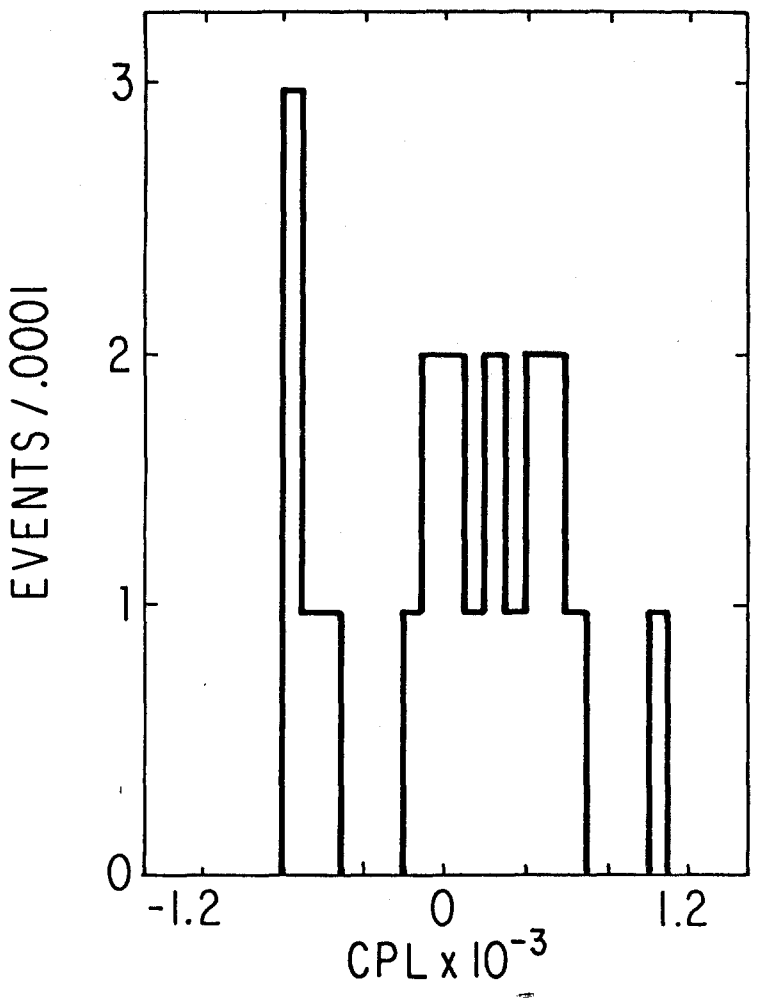

Figure 5.13 (c)

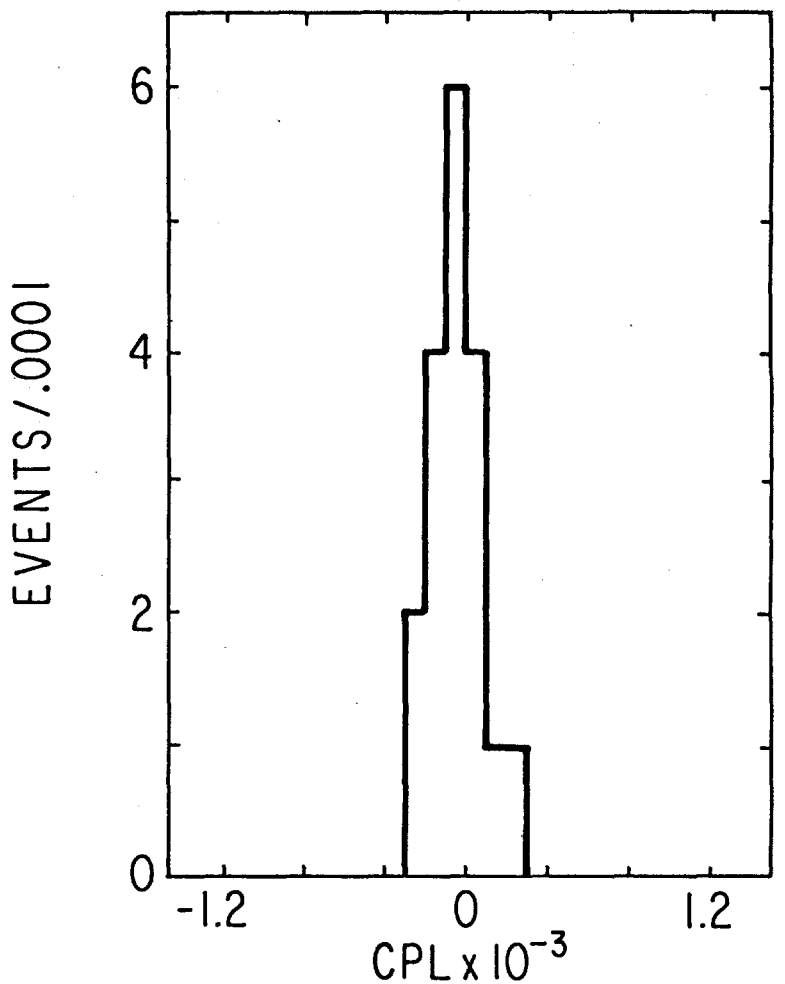

Figure 5.13 (d)

VI. Conclusions

The meson-proton cross sections are approximately equal to the anti-meson cross sections in the range of t covered by this experiment. The proton-proton and antiproton-proton cross sections differ, with the antiproton diffraction peak being slightly narrower than the proton peak. The Chou-Yang model does not distinguish between particle and antiparticle cross sections except for the total cross sections. If the model is correct and the antiproton and proton on proton total cross sections approach each other at high energy, then the difference between the antiproton and proton differential cross sections should disappear at higher energy.

The Chou-Yang model has been used to extract (see Appendix 14) the π^- and p form factors from the scattering data. In this analysis, it is assumed that the scattering amplitude is purely imaginary. The ratio of the real part to the imaginary part of the scattering amplitude has been measured near $-t = 0$. At 200 GeV/c this ratio differs from zero by about 6% for pion-proton scattering and by less than 4% for proton-proton scattering.[26]

The results of the calculation of the profile function is shown in figure 6.1 for the $\pi^- p$ and p reaction. At small impact parameter the pion is less absorptive than the proton. The proton form factor is shown in figure 6.2 along with the dipole fit to the electromagnetic form factor. This fit is given by

$$F(t) = \frac{1}{\left(1 + \frac{|t|}{.71}\right)^2} \tag{1}$$

and is obtained from $e^- p$ scattering data. The agreement between the two is good with the form factor being $\sim$ 15% higher than the dipole form factor around 2 $(\mathrm{GeV}/c)^2$ and a few percent lower at 4 $(\mathrm{GeV}/c)^2$. Figure 6.3 shows the pion form factor obtained from the 200 GeV/c π^- data. The analysis yields the product of the pion and proton form factors. The dipole fit to the electromagnetic form factor was used to determine the pion form factor from this product. The pion form factor falls more slowly than that of the proton indicating that the pion is a smaller object than the proton. Also shown in the figure is a fit to the electromagnetic form factor from reference 20 which obtained the electromagnetic pion form factor in an electroproduction experiment.

The extension of the $\pi^- p$ diffraction peak to $-t > 3.0$ $(\mathrm{GeV}/c)^2$ and the existence of the secondary maximum indicate that diffractive phenomena may be the dominant process in the region $-t < 6$ GeV/c. In this range the QCD arguments of section 2.B are not valid. At larger values of $-t$ the data indicate a slow drop off, but the statistical quality of our data is not good enough for a comparison with the predictions. The data do indicate, however, that there is an enhancement (compared to the exponential form of the diffraction peak) of

the cross section at large values of $-t$. It may be possible to measure the slope of the cross section in this region more precisely in the future.

Figure 6.1. The profile function, $\Gamma(b)$, for the 200 GeV/c for the pp and $\pi^- p$ elastic scattering systems. $\Gamma(b) \equiv 1 - S(b)$ where $S(b)$ is the transmission coefficient at impact parameter b.

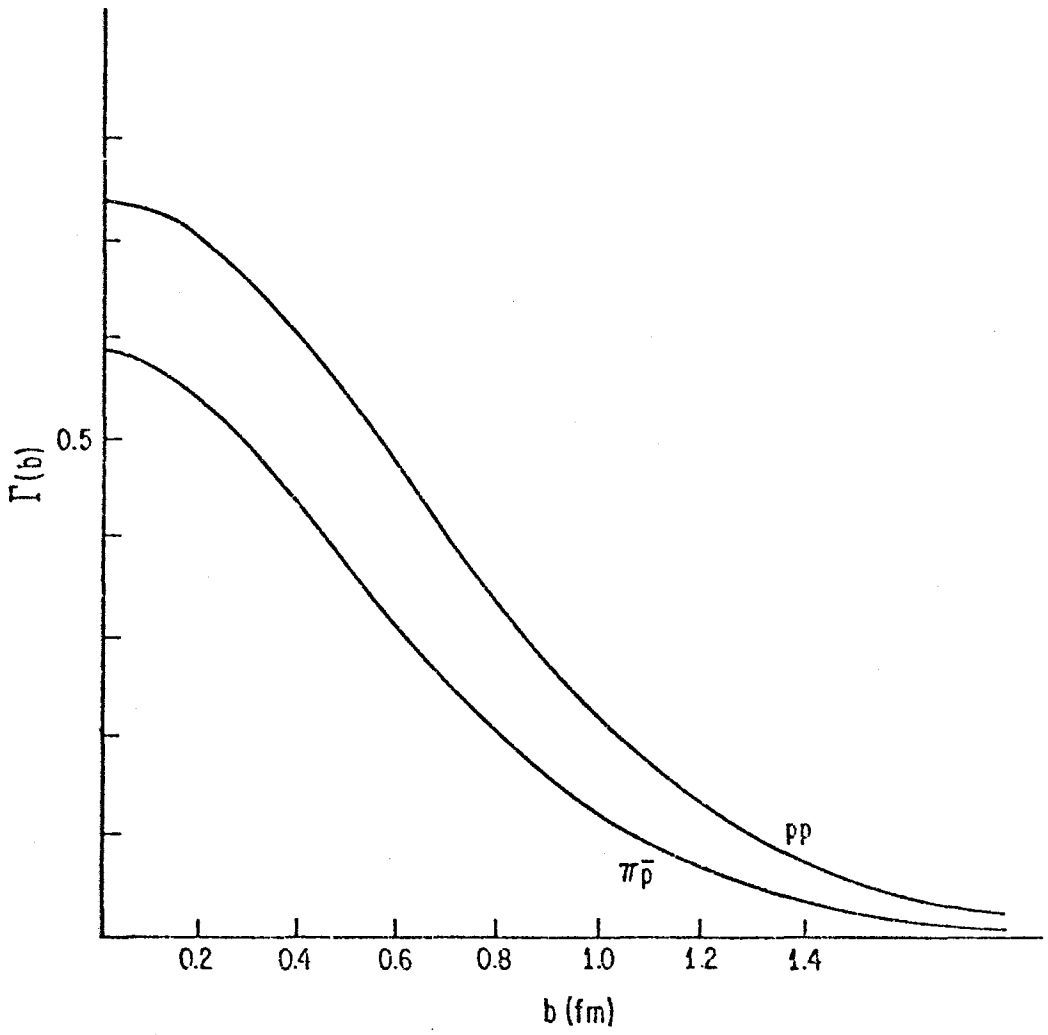
Γ(b)
0.5
pp
$\pi\bar{p}$
0.2
0.4
0.6
0.8
1.0
1.2
1.4
b (fm)

Figure 6.2. The proton form factor. The proton form factor, F(t), is calculated from 200 GeV/c pp elastic scattering data with Chou-Yang theory. The result is compared to the dipole fit of the electromagnetic form factor.

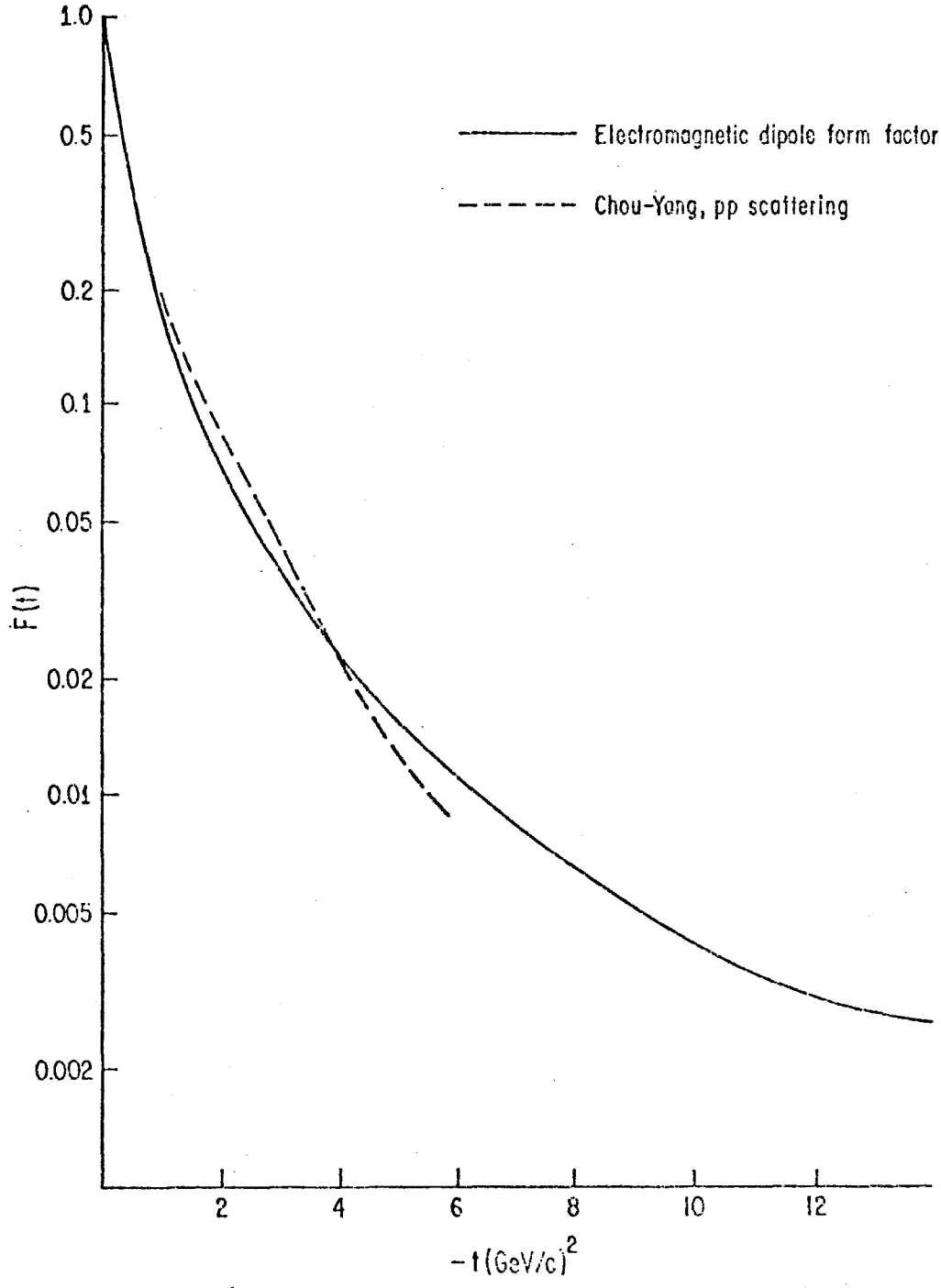
1.0
0.5
0.2
0.1
0.05
0.02
0.01
0.005
0.002
F(t)
Electromagnetic dipole form factor
Chou-Yang, pp scattering
2
4
6
8
10
12
$-t\,(\mathrm{GeV}/c)^2$

Figure 6.3. The pion form factor. The pion form factor, F(t), is calculated from 200 GeV/c $\pi^- p$ elastic scattering data with Chou-Yang theory. The result is compared to a fit given in the last of reference 20.

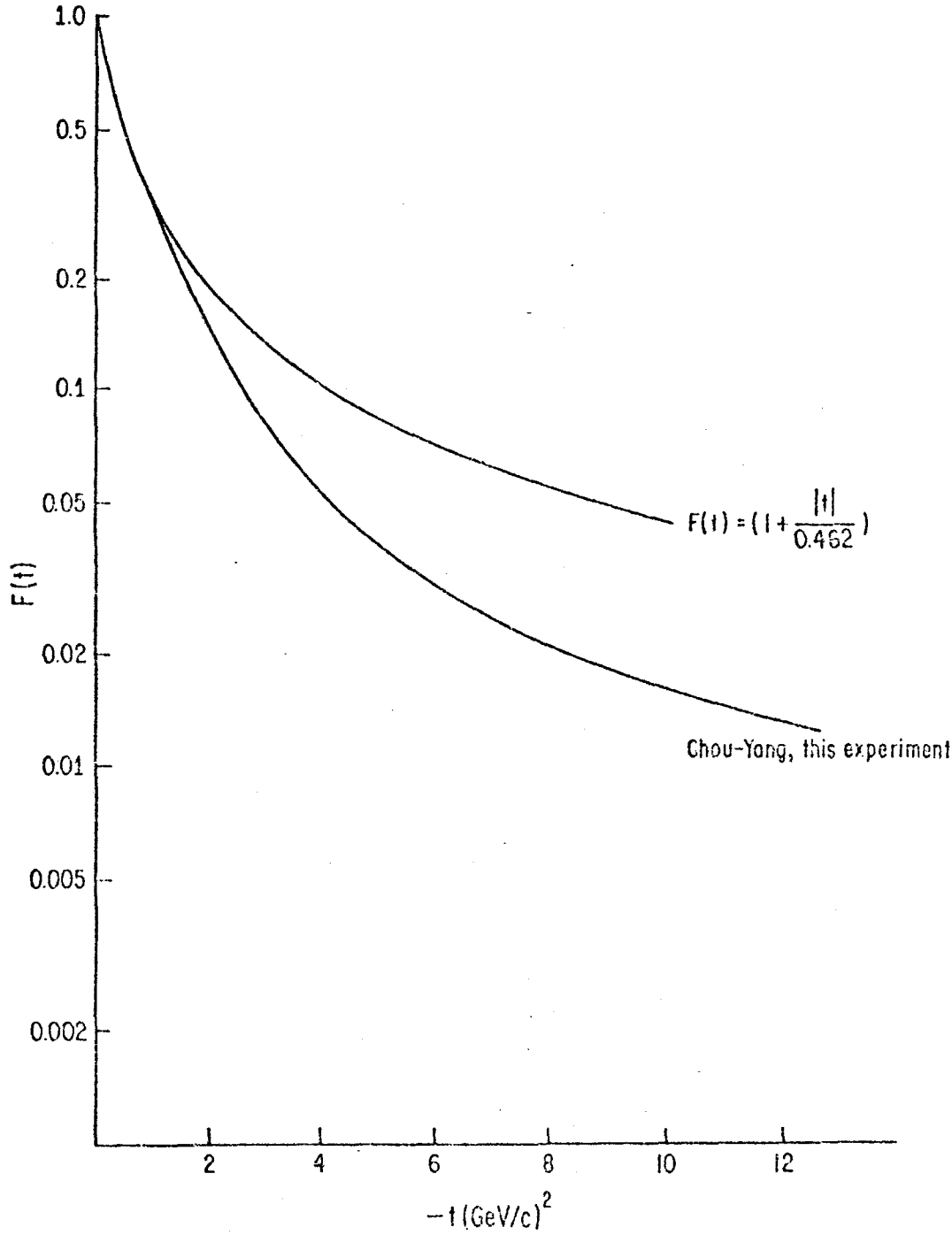
1.0
0.5
0.2
0.1
0.05
0.02
0.01
0.005
0.002
F(t)
2
4
6
8
10
12
−t (GeV/c)²
F(t) = (1 + |t| / 0.462)
Chou-Yang, this experiment

References

1. C. W. Akerloff et al., Phys. Rev. D14 (1976) 2864.

2. G. Fidecaro et al., Phys. Lett. 105b (1981) 309.

3. J. L. Hartmann et al., Phys. Rev. Lett. 39 (1977) 975; W. Faissler et al., Phys. Rev. D23 (1981) 33.

4. E. Nagy et al., Nucl. Phys. B150 (1979) 221.

5. R. Rubinstein et al., Phys. Rev. Lett. 30 (1973) 1010.

6. P. Cornillon et al., Phys. Rev. Lett. 30 (1973) 403.

7. R. J. Miller et al., Phys. Lett. 34B (1971) 230.

8. A. Berlund et al., Nucl. Phys. B176 (1980) 346.

9. A. Schiz et al., Phys. Rev. D24 (1981) 26.

10. D. S. Ayres et al., Phys. Lett. 105B (1981). 309.

11. Z. Aza'd et al., Phys. Lett. 108B (1982) 51; Phys. Lett. 118B (1982) 442.

12. R. Rusack et al., Phys. Rev. Lett. 41 (1978) 1632.

13. Martin L. Perl, High Energy Hadron Physics, John Wiley & Sons, 1974.

14. A. S. Carroll et al., Phys. Rev. Lett. 33 (1974) 928.

15. G. Alberi and G. Goggi, Phys. Rep. 74 (1981) 1.

16. G. L. Kane and A. Seidl, Rev. Mod. Phys. 48 (1976) 309.

17. Seiichi Wakaizumi, Prog. of Theo. Phys. 60 (1978) 1040.

18. L. Van Hove, Nucl. Phys. B122 (1977) 525.

19. T. T. Chou and C. N. Yang, Phys. Rev. 170 (1968) 1591.

20. E. B. Dally et al., Phys. Rev. Lett. 39 (1977) 1176; Phys. Rev. D24 (1981) 1718; Phys. Rev. Lett. 48 (1982) 375, for pion electron scattering and C. J. Bebek et al., Phys. Rev. D17 (1978) 1693, for pion electroproduction.

21. N. F. Mott and H. S. W. Massey, The Theory of Atomic Collisions, Oxford University Press, 1952; Leonard I. Schiff, Quantum Mechanics, McGraw-Hill Book Company, Inc., 1949.

22. R. G. Sachs, Phys. Rev. 126 (1962) 2256.

23. G. Peter LePage and Stanley J. Brodsky, Phys. Rev. D22 (1980) 2157.

24. V. A. Mateev et al., Nuovo Cimento Lett. 7 (1973) 719.

25. P. V. Landshoff, Phys. Rev. D10 (1974) 1024; A. Donnachie and P. V. Landshoff, Z. Physic C2 (1979) 55.

26. L. A. Fajardo et al., Phys. Rev. D24 (1981) 46.

27. Stanley J. Brodsky and G. Peter Lepage, Anne Mosher, eds., Proceedings of the Summer Institute on Particle Physics - Quantum Chromodynamics, Stanford Linear Accelerator Center, SLAC-224 (1980) 133.

28. P. V. Landshoff and J. C. Polkinghorne, Phys. Lett. 44B (1973) 293.

Appendix 1

The M6 Beam

The M6 beam was produced by the interaction of protons, extracted from the accelerator, with the Meson West target. This target, made of beryllium, measured 305 mm along the beam direction and its cross section was 1.5 mm × 1.5 mm. The momentum of the primary proton beam was 350 GeV/c in May-June 1980 and 400 GeV/c in January-March 1981. The secondary beam was selected by collimation at 2.5 mr with respect to the incident protons. During short periods this production angle was reduced to increase the yield of secondary particles.

A series of dipole magnets deflected the secondary beam to beam left, then to beam right. After these bends the beam was approximately parallel to, and about 21 meters to beam left of, the incident proton beam line. The dipoles were placed so that the combined effect of the bends and magnet apertures selected only those particles with momentum within 0.8% of the central beam momentum. Quadrupole magnets were arranged in an optical system with two intermediate foci and a final focus (see Figure A1.1). The system was tuned to meet the following requirements:

1) The beam flux passing through the hydrogen target was maximized.

2) The angular divergence of the beam was minimized at the differential Cerenkov counter.

3) To clear detector support frames, the transverse dimensions of the beam were minimized at the forward spectrometer.

The beam was designed by Fermilab personnel with the aid of the computer programs TRANSPORT and TURTLE.[1, 2] The details of the beam line elements and their tune are given in Table A1.1. The effects of imperfections and misalignments of the beam line elements were compensated with small vernier dipole magnets. During data taking, the beam was fine tuned by monitoring its position with proportional chambers (Fermilab Type A chambers) or SWICs (Segmented Wire Ionization Chambers) at five locations:

Second horizontal focus (z = 300 m)

Second vertical focus (z = 312 m)

Just upstream of the hydrogen target (z = 443 m)

In the forward spectrometer (z = 478 m)

Beam dump (z = 548 m)

Under typical running conditions, the average beam intensity was 8×10^6 particles per accelerator spill (1.5 seconds in 1980, 1.0 seconds in 1981). This beam was modulated by the 53 MHz accelerator radio frequency into bunches 0.5 nanoseconds wide, at approximately 19 nanosecond intervals. Approximately 15-25% of the occupied beam bunches contained more than one particle.

The beam intensity was monitored in two ways:

1) A fast coincidence between signals from two scintillation counters in the beam (B1, B2) assured that the current bunch contained at least one particle. This signal was part of the data acquisition trigger. The bunch width of 0.5 ns made it impractical to count the number of particles in the bunch and hence the total number of beam particles used in the experiment.

2) Two "scatter hodoscopes," (N, M) were used to count, at greatly reduced rates, the number of particles produced at wide angles by the beam during its traversal of a beamline scintillation hodoscope (M) and the hydrogen target (N). The N and M counters were calibrated by extrapolating the ratio of hodoscope counts to beam counts (B1, B2) to low intensity.

The beam was also monitored with two sets of narrow scintillation counters:

P - hodoscope,	32 scintillators	3 mm wide at 2 mm intervals
X - hodoscope,	16 scintillators	4.5 mm wide at 3 mm intervals

These hodoscopes are described in Ref. 3 and gave a coarse determination of the beam particle position and the rate of multiparticle bunches.

References

1. K. L. Brown et al., "TRANSPORT: A Computer Program for Designing Charged Particle Beam Transport Systems," NAL-91 2041.000, SLAC 91, CERN 73-16, March 1974.

2. D. C. Carey, "TURTLE: A Computer Program for Simulating Charged Particle Beam Transport System," NAL-64 2041.000, pm, 9 May 1978.

3. J. E. Elias et al., "A Novel Design for a Hodoscope with 1 mm Granularity," FN-297 2524.000, September 1976.

Table A1.1

Properties of the M6 beam as determined by program TURTLE[1]

Beam at parallel section	Δx	16 mm
	Δy	24 mm
	θ_x	.03 mr
	θ_y	.05 mr
Beam at hydrogen target	Δx	9.0 mm
	Δy	13.0 mm
	θ_x	.14 mr
	θ_y	.28 mr

[1] Δ denotes the full width at half maximum of the envelope of the following variables: x and y are the horizontal and vertical beam locations and θ_x and θ_y are the horizontal and vertical beam angles.

Table A1.2

M6 beam line elements[1]

z (m)	x (m)	Design transverse momentum kick (GeV/c)[2]	Element
0.0	.00		Be target
21.8	.05	.873	dipole
30.2	.11	-.266	quadrupole
33.7	.13	-.266	quadrupole
37.2	.16	.227	quadrupole
40.7	.18	.227	quadrupole
43.1	.20		vertical vernier[3]
47.0	.22		vertical collimator
49.0	.24		horizontal collimator
60.3	.34	3.694	dipole
67.0	.51	3.694	dipole
73.7	.80	3.694	dipole
168.8	6.70	.183	quadrupole
171.5	6.88		horizontal collimator
173.2	6.98		horizontal vernier
174.7	7.08		vertical collimator
176.1	7.16		vertical vernier
178.5	7.31	-.183	quadrupole
240.8	11.20	1.198	dipole
247.0	11.65	1.198	dipole
252.4	12.02	.164	quadrupole
252.9	12.29	.164	quadrupole
261.0	12.67		vertical vernier
263.4	12.84	-.164	quadrupole
266.9	13.10	-.164	quadrupole

Table A1.2 (continued)

z (m)	x (m)	Design transverse momentum kick (GeV/c)[2]	Element
295.1	15.20		horizontal collimator
297.2	15.36		horizontal vernier
314.0	16.60		vertical collimator
315.7	16.73		vertical vernier
318.0	16.90	.231	quadrupole
354.2	19.59	-.261	quadrupole
356.9	19.80	-.130	quadrupole
358.9	19.95	.102	quadrupole
361.7	20.15	.204	quadrupole
368.2	20.61	3.275	dipole
374.9	21.01	3.275	dipole
381.6	21.28	3.275	dipole
388.3	21.45	3.275	dipole
395.0	21.51	3.275	dipole
420.0	21.34	.306	quadrupole
423.5	21.31	-.306	quadrupole
425.8	21.30		horizontal vernier
427.2	21.29		vertical vernier
448.2	21.13		hydrogen target center

[1] The coordinates are: z: the distance along the proton (primary) beam axis; x: the horizontal displacement of the element center from the proton beam axis.

[2] The transverse momentum kicks are the design values for a 200 GeV beam. For dipoles a positive value indicates beam left deflection. The transverse momentum kick for quadrupoles is given at 2.54 cm from the magnet center. A positive value of this kick indicates focusing in the horizontal plane.

[3] A typical vernier adjustment was approximately .005 GeV/c in magnitude.

Figure A1.1. M6 beam optics. The equivalent optic system of the M6 beam line is shown with the horizontal displacement beam envelope for particles with the central momentum. Displacement by the bends is not shown. A, C, and F are focusing quadrupole doublets. B and D are field lenses. The hydrogen target was located at $z = 450$ meters.

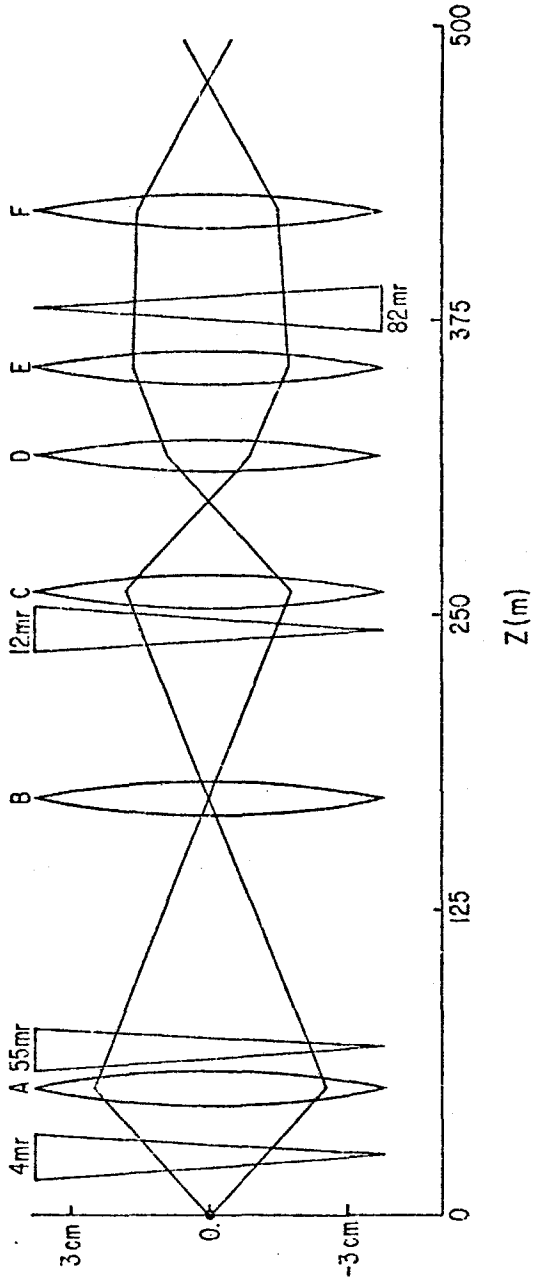
3cm
0.
-3cm
4mr
A
55mr
B
12mr
C
D
E
82mr
F
0
125
250
375
500
Z(m)

Appendix 2

Beam Differential Cerenkov Counter

The differential Cerenkov counter (CB), located in the parallel section of the beam line, is of the DISC type and is described in references 1, 2 and 3. Cerenkov light at 24.5 mr was focused onto an annular diaphragm of 107 mm radius. Eight C31000M photomultiplier tubes were symmetrically located behind the diaphragm. The counter was set to "tag" either pions, kaons or protons by adjusting the density of the helium radiator. This density was monitored with an interferometer. Figure A2.1 is a "pressure curve" which shows the number of CB counts (in coincidence with B1, B2) as a function of the radiator density. The density is given in terms of the interferometer fringe count which has an arbitrary origin. These curves were made at each beam momentum and were used to determine the beam composition. Table A2.1 is a compilation of these results.

For most efficient operation the counter required a beam with angular divergence of less than .02 mr. During data taking the M6 beam line often exceeded this limit resulting in less than optimal efficiency of the counter. The efficiency of the counter could be improved by opening up a diaphragm in the counter, but at the cost of decreased particle separation. The counter was operated so that less than 0.5% of the tagged particles were misidentified. To tag

a particle, six of the eight phototubes were required to be in fast coincidence with the master trigger. A latch, the result of this coincidence, was the only information recorded at each event. Efficiencies for the counter were defined as the number of CB counts in coincidence with the beam counters divided by the appropriate beam fraction times the number of beam counts (Table A2. 2).

References

1. Benot, M. et al., "A Manual for the CERN/NAL High Resolution DISC Cerenkov Counter," CERN, 1973.

2. Bovet, C. et al., "The CEDAR Project, Cerenkov Differential Counters with Achromatic Ring Focus," CERN II/EA/74-4, CERN.

3. Litt, J. and Meunier, R., "Cerenkov Counter Technique in High-Energy Physics," Ann. Rev. Nuclear Science, 23, 1, 1973.

4. More information about our use of the Cerenkov counter may be found in Keith Krueger, Ph.D. thesis, University of Arizona, 1983.

Table A2.1

Beam composition[1]

Beam	Year	% π	% K	% P
-200	1980	95.58 ± .07	3.9 ± .2	.50 ± .08
-200	1981	95.86 ± .06	3.4 ± .3	.77 ± .03
-100	1980	92.9 ± .1	4.6 ± .4	2.5 ± .1
-100	1981	92.4 ± .3	4.7 ± .4	2.9 ± .3
+100	1980	52.1 ± .7	4.3 ± .1	43.6 ± .8
+100	1981	64.2 ± .3	5.1 ± .4	30.7 ± 1.3
+200	1980	12.8 ± .3	2.5 ± .2	84.7 ± .5
+200	1981	17.1 ± .4	2.8 ± .1	80.1 ± .3

[1]The errors are systematic and are derived from the estimated error from the pressure curves. A correction was made for the high beam rate when the +200 1980 pressure curve was taken.

Table A2.2

CB efficiency

Beam	π	K	P
-200	-	.07	.82
-100	.69	.79	.61
+100	-	.73	.68
+200	-	.24	.59

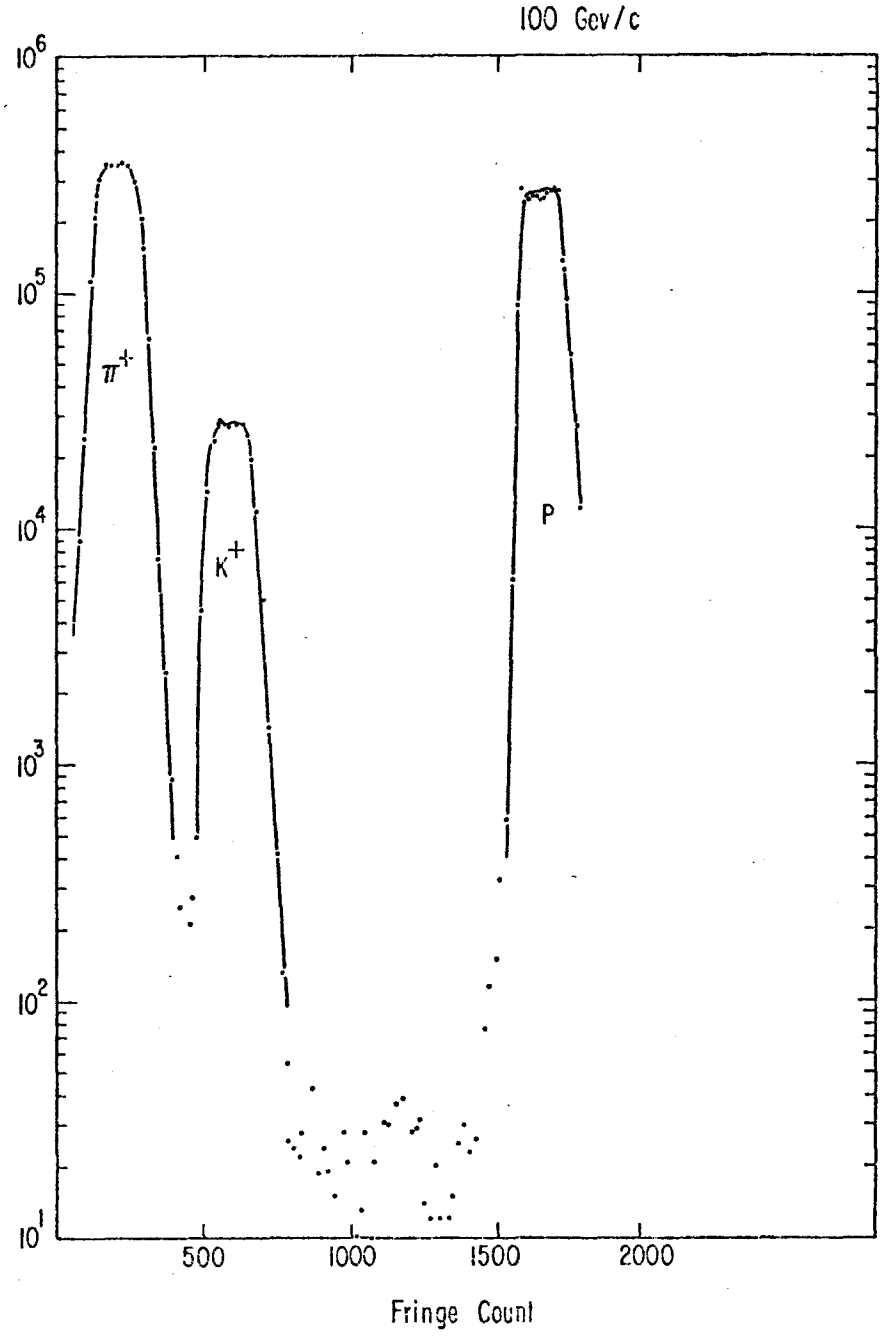

Figure A2.1. Cerenkov counter pressure curve.

Appendix 3

Threshold Cerenkov Counter

The threshold counter (CF), located in the forward spectrometer, used helium as a radiator and was 27.7 m long. Cerenkov light from the scattered hadron was collected by the four horizontally adjacent spherical (radius 27.9 m) mirrors each 30.5 cm wide and 40.6 cm high. The first 22 cm of the mirror closest to the beam line was masked to render the counter insensitive to the unscattered beam. The light was focused onto a single RCA C31000M phototube. The counter was operated below atmospheric pressure. At 200 GeV/c beam momentum the counter was just insensitive to particles with proton velocities or less. At 100 GeV/c beam momentum the counter was operated between the proton and kaon thresholds for sensitivity. Figure A3.1 shows the response of the counter to protons, kaons, and pions at 100 GeV/c. These graphs show the pulse height of the phototube during an elastic event in which CB tagged the presence of the particle in the beam. Figure A3.2 shows the response of the counter at 200 GeV/c. These measurements were made during special runs in which the forward analysis magnets (M1, M2) were turned off (so that the beam traversed the sensitive region of CF) and the apparatus triggered on a coincidence between beam and CB. In both cases it was required that both the P and X hodoscope register at most one beam particle.

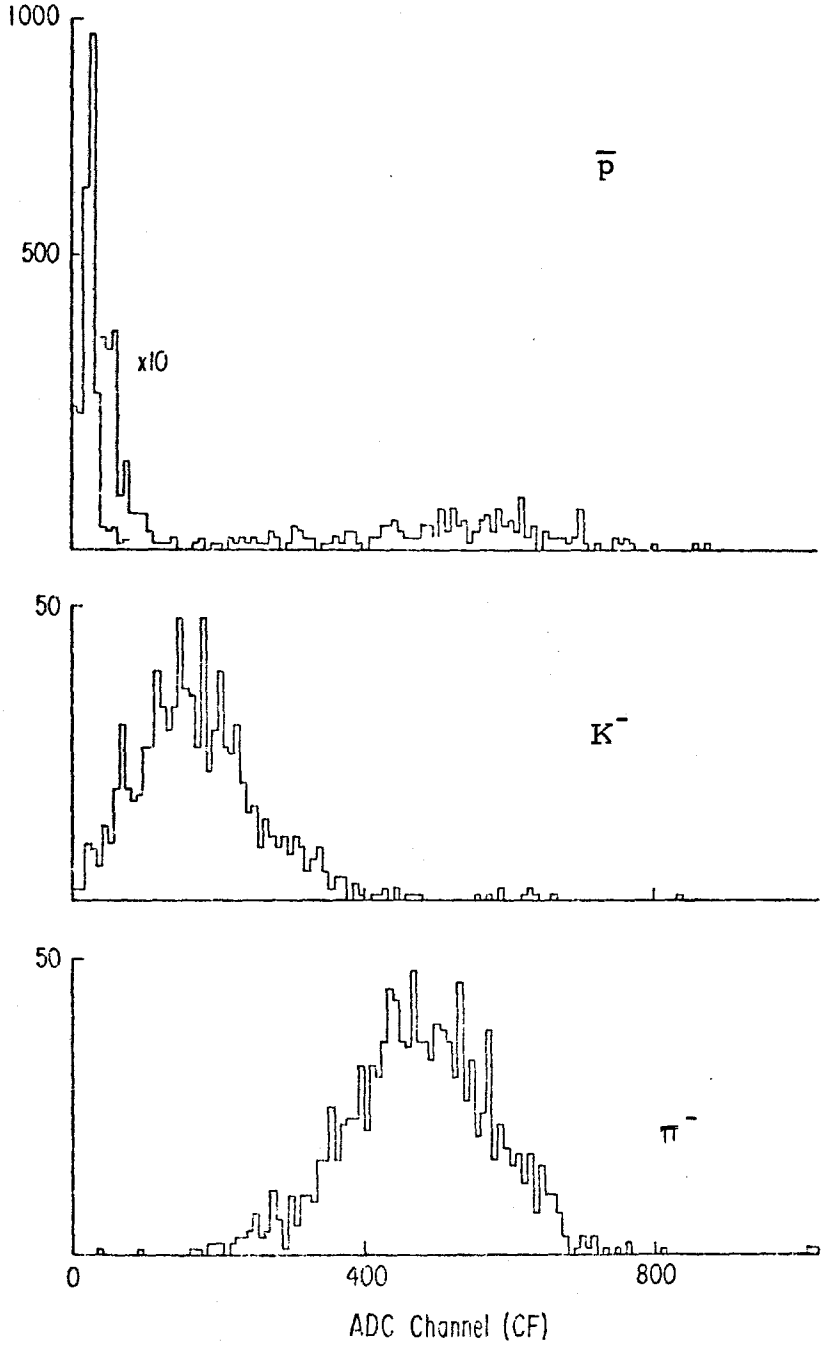

Figure A3.1. Response of the threshold Cerenkov counter to 100 GeV/c, $\bar{p}$, K^- and π^-.

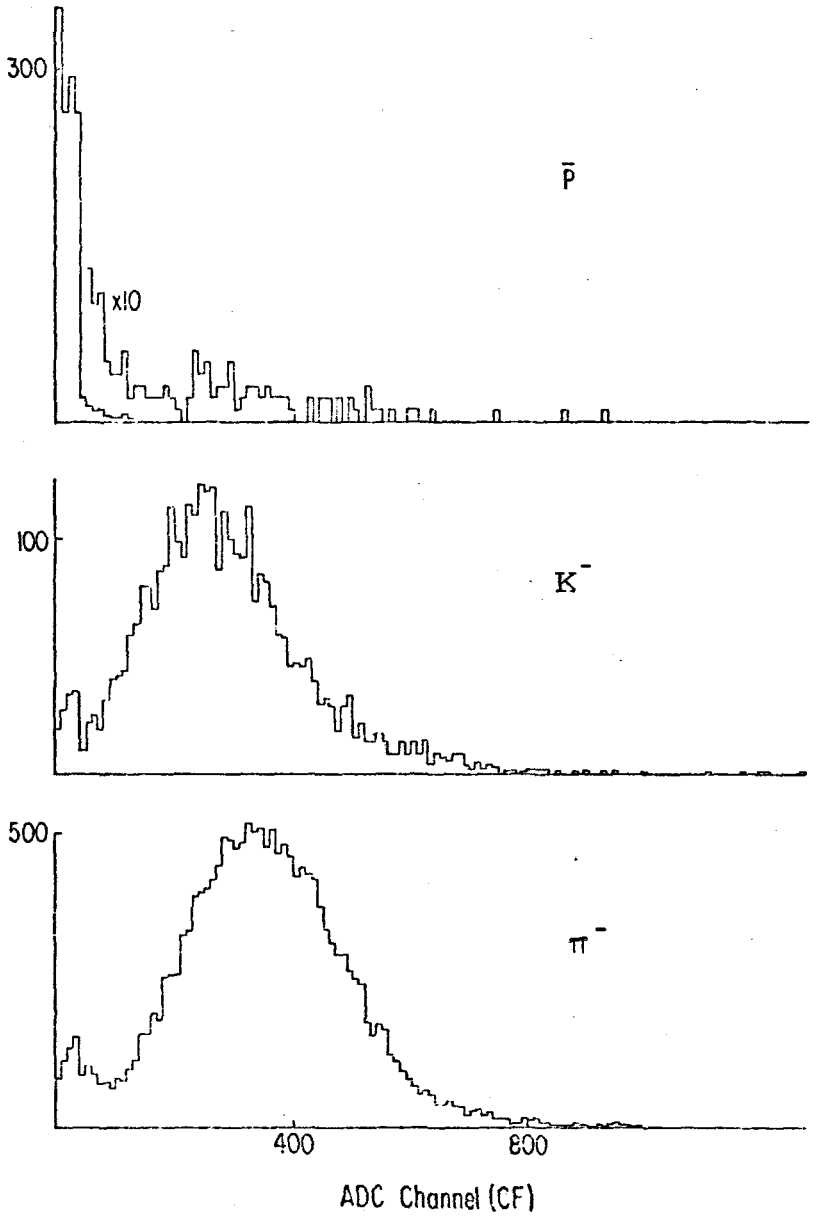

Figure A3.2. Response of the threshold Cerenkov counter to 200 GeV/c, $\bar{p}$, K^- and π^-.

Appendix 4

Liquid Hydrogen Target and Target Veto Counters

The liquid hydrogen target was built and maintained by the Hydrogen Target Group at Fermilab. Design parameters for the target flask are given in Table A4.1. The flask was wrapped in 20 layers of superinsulation and the space surrounding the target was evacuated. This space was contained by an aluminum block whose walls were 38 mm or more thick except for the front, back and beam right sides which were made of 0.39 mm thick mylar. The top, bottom and beam left sides of the target block were covered with veto scintillation counters. The aluminum kept electrons, scattered by the beam, from the veto counters but allowed high energy recoil protons and charged secondaries to hit the counters.

Table A4.1

Hydrogen target

Flask length	101.6 cm
Flask radius	3.8 cm
Flask material	.25 mm mylar
Liquid hydrogen density	.0708 g/cm^3
Number of protons contained in flask during running	4.28×10^{24} cm^{-2}

Appendix 5

Forward and Recoil Spectrometers

The acceptance of the spectrometers was optimized for 200 GeV/c beam momentum, although no change to the geometry was made for the 100 GeV/c running. The design was subject to the following constraints.

1. Only existing proportional wire chambers and analysis magnets were to be used.
2. The unscattered beam had to clear all magnet yokes and support frames.
3. The lever arms between the chamber stations in the forward spectrometer were to be made long, in order to maximize the angular resolution, but the apparatus had to fit inside the Meson laboratory and M6 extension tunnel.
4. The forward analysis magnets could not be placed so far downstream as to limit the acceptance in the desired range of measurement.
5. The recoil analysis magnet was to be placed as close as possible to the hydrogen target in order to maximize the azimuthal acceptance.
6. Proportional wire chambers which measure the recoil proton trajectory were to cover as much of the magnet aperture as possible.

The constraints on the forward arm were solved by having the beam pass through the magnet gaps. Proportional wire chambers were placed as close to the beam as possible. Helium bags were placed in the forward spectrometer to minimize multiple scattering and absorption of the scattered hadron. A hole for the beam and scattered hadron was made in the recoil magnet yoke. The recoil apparatus was aligned along an axis 25 degrees from the forward beam (z) axis (see Figure 3.3). To maximize the efficiency of event reconstruction and to be able to determine chamber efficiencies all available chambers were used. The positions of the chambers is listed in Table A5.2. The chambers have been named with an f, r or b denoting forward spectrometer, recoil spectrometer and beam. The names end with an x or y to denote measurement of the horizontal or vertical coordinate respectively. The recoil positions are in terms of the recoil coordinate system. With the exception of the downstream recoil chambers, the length of the signal wires was more than sufficient to cover the required aperture. The downstream x recoil chambers had a transverse (y) dimension of 70 cm which was just sufficient to cover the 70 cm vertical aperture defined by the H2 hodoscope. Because there were small misalignments a fiducial cut was made on the data to limit the vertical aperture. Two y chambers were placed to cover the apertures defined by r10x and r11x.

Two forward chambers, f7x and f8y, were placed in the beam just before the M2 analysis magnet. Two additional chambers, b1x

and b2y, were placed in the beam upstream of the liquid hydrogen target. During special alignment runs the analysis magnets were turned off and the beam intensity lowered. The undeflected beam went through the above chambers and also through f14x, f15y and f16x. This enabled the forward chamber positions to be aligned with respect to the beam. The recoil chambers were aligned by turning the M1 analysis magnet off, but absolute alignment between the recoil and forward arm used survey data which was checked with elastic scattering kinematics.

Table A5.1

Analysis magnets

Name	Type	Location	Center x or x′ (m)	Position z or z′ (m)	Aperture (horiz. × vert.) (m)	(m)	Depth (m)	Field integral (GeV/c)
M1	72D18	Recoil	1.53	-2.10	.183	.305	.457	.270
M2	BM109	Forward	30.48	.254	.610	.203	1.880	
M3	BM109	Forward	32.92	.244	.610	.203	1.880	(2.050/1.031)[1]

[1] This is the combined field integral of M2 and M3. The first value is for 200 GeV running and the second for 100 GeV/c running.

Table A5.2

Chamber deployment

Name	Type[1]	z or z′ position (m)	Wire spacing (mm)	Number wires	1st wire position (cm)	Last wire position (cm)
f1y	FNAL	12.62	2.00	64	-6.75	5.85
f2x	FNAL	12.74	2.00	96	4.15	23.15
f3y	FNAL	12.88	2.00	64	-6.64	5.96
f4x	FNAL	13.01	2.00	96	4.31	23.31
f5x	CBUG	28.53	1.59	256	14.11	54.59
f6y	CBUG	28.64	1.59	144	-11.86	10.84
f7x	CLASP	20.61	1.27	496	-10.65	52.34
f8y	CLASP	28.82	1.27	144	-9.75	16.90
f9x	FNAL	29.05	2.00	192	11.84	50.04
f10y	FNAL	29.15	2.00	96	-9.62	9.38
f11x	CBUG	34.58	1.59	320	13.55	64.19
f12y	CBUG	34.68	1.59	144	-12.29	10.41
f13x	FNAL	34.91	2.00	248	12.29	61.69
f14x	CLASP	66.72	1.27	720	-5.54	85.78
f15y	CLASP	66.83	1.27	320	-21.16	19.34
f16x	FNAL	67.00	2.00	448	-8.60	80.80
r1x	FNAL	.67	2.00	432	-59.28	26.92
r2y	FNAL	.70	2.00	88	-8.42	8.98
r3y	FNAL	.87	2.00	96	-8.86	10.14
r4x	FNAL	1.07	2.00	504	-81.05	19.55
r5y	FNAL	1.10	2.00	112	-10.93	11.27
r6x	FNAL	2.17	4.00	312	-105.80	18.60
r7x	FNAL	2.32	4.00	320	-109.09	18.51
r8x	CLASP	2.86	1.27	304	-147.57	-109.09
r9x	FNAL	2.92	4.00	296	-93.42	24.58
r10x	FNAL	3.07	4.00	120	-157.34	-109.73
r11x	FNAL	3.14	4.00	296	-94.74	23.26
r12y	CLASP	3.41	1.27	480	-30.34	30.49
r13y	CLASP	3.44	1.27	480	-29.89	30.94
b1x	FNAL	-17.904	2.00	48	-3.10	6.30
b2y	FNAL	-17.986	2.00	48	-4.29	5.11

[1]The types of chambers are described in Appendix 6.

Appendix 6

Proportional Wire Chambers

Two types of proportional wire chambers were used in this experiment. Chambers of the first type were built by Fermilab (FNAL) and used in previous experiment E-290.[1] These chambers used a gas mixture of 80% argon and 20% carbon dioxide with a trace (0.1%) of freon 13B1. The .02 mm diameter gold plated tungsten signal wires were spaced at 2 mm intervals. The downstream recoil FNAL chambers had adjacent signal wires connected giving an effective wire spacing of 4 mm. The high voltage planes were .08 mm diameter Cu-Be alloy wires spaced .5 mm apart. The signal plane to high voltage plane gap was 6 mm. Signals from each wire were amplified and transmitted to the experimental control room on striplines. Here coincidences between the wire signals and the master trigger were made and the data encoded and stored in memory. This memory was subsequently accessed via a CAMAC command from the data acquisition computer. Details of these chambers may be found in reference 2.

The second type of chamber was built at Cornell University. These chambers were first used by the CBUG[3] group and the CLASP[4] group. The sensitive area of the CBUG chambers was 55 cm × 33 cm (horizontal × vertical as used in this experiment) and the signal wire spacing was 1.27 mm. The CLASP chambers had a sensitive area

of 90 cm ×58 cm and signal wire spacing of 1.59 mm. The signal wires were .02 mm diameter gold plated tungsten. Two high voltage planes of .025 mm aluminum foil were spaced 6.3 mm on either side of the signal wire plane. The gas enclosure was made with .008 or .013 mm mylar spaced 6.3 mm from each high voltage plane. The chambers used a gas mixture of argon (76%), isobutane (19.5%), methylal (4%) and freon 13B1 (.5%).

One special "driver card" was used in each chamber. The purpose of this card was to regenerate signals going to and from the chamber. The wire signals were amplified by a circuit designed by Browman.[5] The adjustable threshold voltage on the cards was set at -2 volts. With this threshold the chambers reached maximum efficiency at about 4.5 kV (CBUG) and 5.5 kV (CLASP). The signal was amplified and delayed by a one shot. A bias voltage on each chamber was used to adjust this delay. This particular set of Browman cards used RC timing of 180 ns. Because long delays caused bad time jitter, the pretrigger logic was duplicated close to the spectrometers (outside pretrigger). The needed delays were about 300 ns (forward) and 350 ns (recoil). In each channel the coincidence of the amplified signal and an enable gate (the pretrigger with 120 ns duration) was latched and strobed into a shift register by a clock pulse. This clock pulse was generated on the driver card from the trailing edge of the enable pulse. The serial output of one shift register was connected to

the input of the next shift register. All shift registers in the forward spectrometer were chained in this way. The recoil chambers had a separate shift register chain.

A master trigger initiated the readout by two "wire chamber scanners."[6] The trigger caused each scanner (forward and recoil) to generate a 5 MHz clock which was transmitted to the end of each spectrometer. The clock was used to step the shift register chain. The clock and serial data were transmitted in synchronism from chamber station to chamber station and then back to the scanner. When the Nth clock pulse arrived back at the scanner the data line was high if the Nth shift register bit had been set. A scaler in the scanner counted each clock pulse. When the data line was high a second scaler began counting clock pulses until the data line went low or seven clock pulses were counted. The first scaler was the address of the last wire in a "cluster" and the second gave the number of wires in the cluster. At this point the contents of both scalers were stored, as one word, in a 64 word memory. The data was retrieved by a subsequent CAMAC command generated by the data acquisition computer.

Efficiencies of the wire chambers were calculated from the elastic event sample in which a latch from the outside pretrigger was present. The "raw" efficiency of a chamber in an N chamber pattern recognition group was defined as the number of times the chamber was used in an N or N-1 track segment divided by the number of N and

N-1 track segments. The raw efficiency was corrected by assuming that the inefficiencies between chambers were uncorrelated. The outside pretrigger efficiency was calculated from the sample of elastic events in which all the FNAL chambers were used. The FNAL chambers were sufficient to reconstruct an event so this was an unbiased sample. The efficiencies are shown in Table A6.1.

References

1. W. F. Baker et al., "Measurement of π^+-p Backward Elastic Scattering between 30 and 90 GeV/c," Phys. Rev. Lett. 43, 22 (1979).

2. Dave Kaplan, Ph.D. Thesis, Cornell University, 1983.

3. R. Galik, "Spectrometer Study of the Electroproduction of the Phi Vector Meson," Ph.D. Thesis, Cornell University, 1977.

4. J. L. Hartman et al., "201-GeV/c Proton-Proton Elastic Scattering at Large Momentum Transfer," Phys. Rev. Lett. 39, 975 (1977).

5. A. Browman, "Wire Chamber Amplifier Board," Cornell Lab. of Nucl. Sci. Memo TOP-6006-14 and drawing DMO 6006-14, Cornell University, 1972.

7. These scanners were designed by Thomas Nunamaker and manufactured by Nanometric Systems, Inc., Oak Park, IL.

Table A6.1

Chamber efficiencies

Period	1	2	3	4	5	6	7	8	9	10	11	12	13	14	15
f1x	.93	.97	.96	.95	.97	.98	.97	.90	.94	.72	.94	.95	.97	.97	.96
f2y	.98	.99	.86	.97	.96	.94	.98	.96	.98	.97	.97	.97	.99	.97	.97
f3x	.98	.98	.97	.97	.97	.99	.98	.96	.97	.96	.96	.96	.97	.97	.96
f4y	.96	.97	.81	.93	.89	.93	.94	.91	.95	.95	.93	.94	.94	.96	.95
f5x	.99	.99	.99	.98	.98	1.0	.98	.97	.99	.98	.97	.98	.98	.98	.96
f6y	.97	.99	.80	.95	.98	.96	.98	.92	.98	.98	.97	.97	.87	.98	.97
f9x	.93	.92	.94	.85	.90	.89	.90	.94	.97	.89	.91	.90	.97	.96	.97
f10y	.83	.56	.79	.80	.85	.81	.87	.98	.99	.88	.91	.90	.90	.97	.98
f11x	.95	.97	.84	.95	.95	.90	.92	.97	.96	.96	.93	.95	.98	.95	.96
f12y	.99	.99	.86	.95	.94	.95	.96	.97	.98	.92	.94	.92	.95	.95	.95
f13x	.98	.90	.65	.97	.98	.98	.98	.96	.98	.96	.98	.96	.98	.89	.96
f14x	.91	.91	.78	.86	.80	.87	.87	.90	.95	.85	.91	.91	.92	.88	.88
f15y	.94	.94	.83	.87	.86	.94	.93	.90	.95	.88	.89	.90	.92	.92	.91
f16x	.96	.98	.85	.98	.98	.98	.99	.97	.97	.96	.97	.98	.98	.94	.94
r1x	.98	.94	.96	.96	.95	.93	.96	.96	.96	.95	.99	.99	.99	1.0	1.0
r2y	.92	.92	.85	.89	.88	.91	.91	.94	.96	.98	.94	.92	.92	.96	.88
r3y	.97	.96	.96	.94	.95	.95	.96	.95	.97	.94	.91	.95	.97	.98	.97
r4x	.94	.92	.98	.93	.98	.96	.99	.95	.97	.95	.93	.96	.98	.97	.97
r5y	.88	.92	.85	.81	.82	.87	.88	.88	.94	.82	.75	.83	.87	.91	.86
r6x	.97	.00	.97	.95	.96	.97	.94	.92	.97	.00	.67	.76	.87	.86	.80
r7x	.92	-	.94	.93	.88	.88	.88	.93	.95	-	.80	.75	.70	.71	.66
r8x	.99	-	.89	.99	.96	.97	.98	.98	.99	-	.99	.99	.99	.99	.99
r9x	.82	.89	.70	.84	1.0	-	.88	.95	.89	.86	.94	.97	.93	1.0	.95
r10x	.99	-	.99	.99	.99	.99	.99	.99	.99	-	.98	.99	.99	.99	.99
r11x	.99	.89	.70	.83	.86	-	.87	.98	.97	.86	.93	.97	.90	1.0	.98
Pretrigger	.74	-	.83	.79	.96	.94	.96	.96	.95	-	.45	.96	.96	.96	.96

Appendix 7

Trigger Hodoscopes and Scintillation Counters

The deployment of the trigger hodoscopes is given in Table A7.1. These hodoscopes were designed to cover the full range of acceptance. The trigger hodoscopes H2, H3 and H4 were constructed for Fermilab experiment 290.[1] All elements of these hodoscopes used a 56AVP phototube and a resistive chain voltage divider. These counters used cast acrylic light guides and the phototubes were shielded with Co-Netic shielding.[2] The H2 hodoscope, because of its proximity to the recoil analysis magnet, had additional shielding of .76 cm of steel.

The H1 hodoscope was constructed for this experiment. The scintillators were made as thin as possible (3.2 mm) in order to minimize multiple scattering of the low energy recoil proton. Light from the scintillator was transported to the phototube through an adiabatic light guide and then a 22 mm radius cylindrical light guide to 8575 phototubes. This long (75 cm) light guide was needed to remove the phototube base from the vicinity of the field of the recoil analysis magnet. The phototubes were shielded with Co-Netic shielding and .76 cm of steel. These counters used a transistorized base designed after those of C. Kerns of Fermilab.[3]

References

1. W. F. Baker et al., "Measurement of π^+ - p Backward Elastic Scattering between 30 and 90 GeV/c," Phys. Rev. Lett. 43, 22 (1979).

2. This type of shield was manufactured by Magnetic Shield Division, Perfection Mica Company, Bensenville, IL.

3. C. R. Kerns, "A High-Rate Phototube Base," IEEE Transactions on Nuclear Science, Vol. NS-24, no. 1., February, 1977.

Table A7.1

Hodoscopes

Name	Number of Elements	Element	x min (cm)	x max (cm)	Scintillator thickness (mm)	Position z or z′ (m)	Height (cm)	Vertical Displacement (cm)
H1	6	1	-60.96	-45.72	3.2	6.22	15.24	0
		2	-45.72	-30.48			15.24	
		3	-30.48	-15.24			15.24	
		4	-15.24	0.00			12.70	
		5	0.00	15.24			12.70	
		6	15.24	22.86			7.62	
H2	12	U1, L1	-149.86	-121.92	12.7	3.30	30.48	U: +15.24
		U2, L2	-121.92	-97.98				L: -15.24
		U3, L3	-97.98	-66.04				
		U4, L4	-66.04	-38.10				
		U5, L5	-38.10	3.81				
		U6, L6	3.81	17.78				
H3	7	1	11.08	18.07	6.34	35.26	19.05	0
		2	18.07	25.06				
		3	25.06	32.04				
		4	32.04	39.03				
		5	39.03	46.01				
		6	46.01	53.00				
		7	53.00	59.88				
H4	7	1	-5.71	8.89	6.35	67.16	36.83	0
		2	.16	23.97				
		3	13.02	36.83				
		4	25.88	49.69				
		5	38.74	62.54				
		6	51.60	75.40				
		7	65.41	80.01				

Table A7.2

Additional scintillators

Name	Location	Position z or z′ (m)	Scintillator thickness (mm)	Dimensions (mm)
B1	Beam	-17.38	6.35	44.5 × 63.5
B2	Beam	-3.39	3.17	radius 25.4
A1	Beam	-3.49	6.35	203 × 203 w/25.4 hole
A2	Top target block		12.7	Covers target block
A3	Beam left side target block		12.7	Covers target block
A4	Bottom target block		12.7	Covers target block
N1	Target scatter monitor	~ 2.0	6.35	63.5 × 44.5
N2				
N3				
M1	Beam scatter monitor	~ -17.0	6.35	63.5 × 44.5
M2				
M3				

Appendix 8

Trigger Logic

The trigger logic is shown in Figure A8.1. The trigger is composed of a fast coincidence between the beam and hodoscope elements. In the figure lines with a subscript i, j, k. or ℓ represent parallel signals from each of the hodoscope elements. Intermediate signals used by the trigger are defined in Figure A8.2. Only major delays are shown in these figures.

The logic first defined the "beam" signal which was a fast coincidence between B1 and B2 with no signal in A1 (the beam halo veto counter). Next a coincidence between the appropriate elements in H1 and H2 was made. Only appropriate coincidences (those consistent with possible elastic scattering trajectories and the element positions) contributed to the trigger. The logic matrices are defined in Table A8.1. This coincidence was vetoed by any of the target anticounters (A2, A3, A4) or the detection of more than 1 particle by either H1 or H2 (H1, H2 multiplicity). This signal constituted a pretrigger which was used to enable the wire chambers. This coincidence started the logic gate which disabled durther pretriggers. If a master trigger was not completed in 670 ns then the logic gate was turned off and the trigger enabled. The signals from H3 and H4 arrived in the experimental control room approximately 240 ns and 630 ns later than

the beam signals respectively. A coincidence (matrix B) was made between the elements of H3 and H4. This coincidence was vetoed by the occurrence of more than one signal from H3 (H3 multiplicity) or more than 2 signals from the overlapping H4 elements (H4 multiplicity). The H4 elements were placed so that matrix B (H3, H4) was diagonal.

Finally, a coincidence (matrix C) was made between the H2 and H3 elements. With a master trigger the logic system remained disabled until the logic gate was reset by the data acquisition computer.

A trigger which resulted from the hodoscope coincidence was called a type 1 trigger. A second type of trigger (type 2) required only the coincidence between a pulse generator and the beam signal. About 5% of the triggers were type 2.

Table A8.1

Logic matrices[1]

200 GeV/c

A		H1 i = 1	2	3	4	5	6
H2	j = 1	1	1	1	1	1	0
	2	1	1	1	1	1	0
	3	0	1	1	1	1	1
	4	0	1	1	1	1	1
	5	0	0	1	1	1	1
	6	0	0	0	0	1	1

B		H3 k = 1	2	3	4	5	6	7
H4	l = 1	1	0	0	0	0	0	0
	2	0	1	0	0	0	0	0
	3	0	0	1	0	0	0	0
	4	0	0	0	1	0	0	0
	5	0	0	0	0	1	0	0
	6	0	0	0	0	0	1	0
	7	0	0	0	0	0	0	1

C		H3 k = 1	2	3	4	5	6	7
H2	j = 1	1	1	1	0	0	0	0
	2	1	1	1	1	0	0	0
	3	1	1	1	1	1	0	0
	4	0	0	1	1	1	1	1
	5	0	0	0	1	1	1	1
	6	0	0	0	0	1	1	1

100 GeV/c

A		H1 i = 1	2	3	4	5	6
H2	j = 1	1	1	1	1	1	0
	2	0	1	1	1	1	1
	3	0	0	1	1	1	1
	4	0	0	0	0	0	0
	5	0	0	0	0	0	0
	6	0	0	0	0	0	0

B		H3 k = 1	2	3	4	5	6	7
H4	l = 1	1	0	0	0	0	0	0
	2	0	1	0	0	0	0	0
	3	0	0	1	0	0	0	0
	4	0	0	0	1	0	0	0
	5	0	0	0	0	1	0	0
	6	0	0	0	0	0	1	0
	7	0	0	0	0	0	0	1

C		H3 k = 1	2	3	4	5	6	7
H2	j = 1	0	1	1	1	1	1	1
	2	0	0	0	1	1	1	1
	3	0	0	0	0	1	1	1
	4	0	0	0	0	0	0	0
	5	0	0	0	0	0	0	0
	6	0	0	0	0	0	0	0

[1] The symbol 1 indicates that the combination of hodoscope elements was used for the trigger. A 0 indicates that the combination was not used.

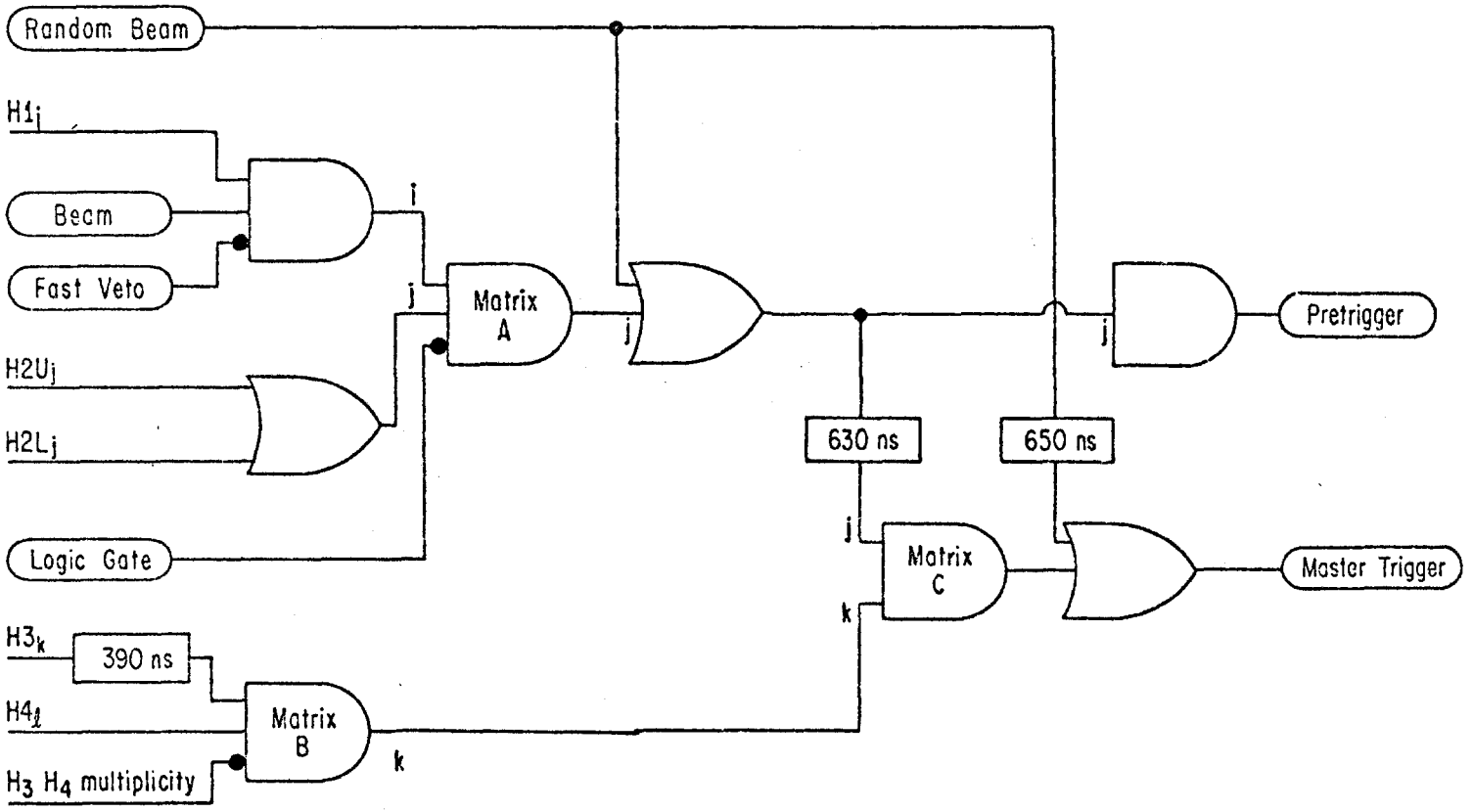

Figure A8.1. Trigger logic.

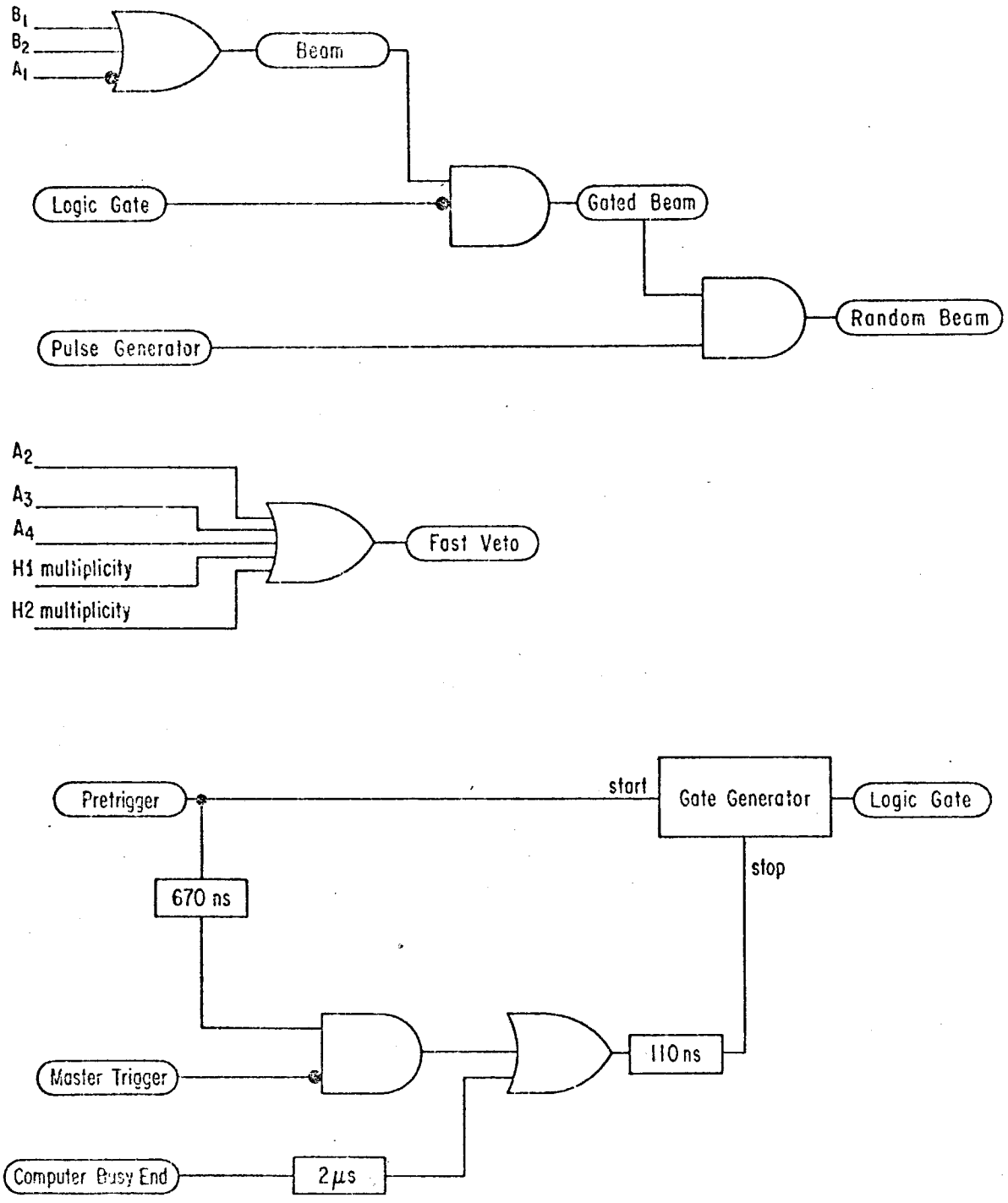

Figure A8. 2. Beam, fast veto and logic gate

Appendix 9

Elastic Two Body Kinematics

The scattering reaction

$$1 + 2 \longrightarrow 3 + 4 \tag{1}$$

can be described by the 16 components of the energy-momentum vectors $P_i = (E_i, \vec{p}_i)$ of the four particles. For an elastic reaction,

$$m_1 = m_3 \equiv m \quad \text{and} \quad m_2 = m_3 \equiv M \tag{2}$$

Conservation of energy and momentum,

$$P_1 + P_2 = P_3 + P_4 \tag{3}$$

and Lorentz invariance,

$$E_i^2 = \vec{p}_i^{\,2} + m_i^2 \tag{4}$$

specify eight constraints between the 16 components. Fixing the Lorentz frame provides five more constraints. For example, fixing the direction of $\vec{p}_1$ provides two constraints and choosing a laboratory reference frame where the target particle is at rest ($\vec{p}_2 = 0$) provides three more. The three remaining degrees of freedom can be given by the square of the center of mass energy,

$$s = (P_1 + P_2)^2 = (P_3 + P_4)^2 \tag{5}$$

the square of the four momentum transfer

$$t = (P_1 - P_3)^2 = (P_2 - P_4)^2 \tag{6}$$

and azimuthal angle ϕ, of a polar coordinate system with polar axis in the direction of $\vec{p}_1$. In such a system the final state azimuthal angles are related by

$$\phi_3 = \phi_4 - \pi \equiv \phi \tag{7}$$

If there are no polarization effects (there is no natural origin for ϕ) then s and t alone are sufficient to describe the reaction. In terms of the polar coordinate system:

$$s = m^2 + M^2 + 2ME_1 \tag{8}$$

$$t = 2m^2 - 2E_1E_3 + 2p_1p_3 \cos\theta_3 \tag{9}$$

$$= -2M(E_4 - M) \tag{10}$$

$$= \frac{-2ME_1\, p_4 \cos\theta_4}{E_1 + M} \tag{11}$$

The following approximations are useful:

$$-t = 2p_1\left(p_1 - \frac{t}{2M}\right)(1 - \cos\theta_3) \qquad m \ll p_1 \tag{12}$$

$$-t = \frac{2M\, p_1 p_4 \cos\theta_4}{(p_1 + M)} \qquad m \ll p_1 \tag{13}$$

$$s = 2ME_1 \qquad m \ll E_1,\ M \ll E_1 \tag{14}$$

$$-t = p_1^2\,\theta_3^2 \qquad -t \ll 2Mp_1,\ m \ll p_1 \tag{15}$$

$$-t = 4M^2 \cot^2\theta_4 \qquad M \ll p_1,\ m \ll p_1 \tag{16}$$

Equations (12) and (13) are valid to .01% over the range of this experiment so that the mass of the beam particle can be neglected in the data reduction. Equations (15) and (16) are valid to 4% in this range.

Appendix 10

Event Reconstruction and Selection

The master trigger initiated recording of the state of the detector onto magnetic tape ("raw data tape"). The first step in reducing the raw data to cross sections was to determine the particle trajectories of each event (event reconstruction) and to sift out those events that corresponded to elastic processes (event selection).

1. Event Reconstruction

In order to reconstruct tracks the proportional wire data were converted into real coordinates. A particle traversing a chamber normal to the wire plane set one or two wires. Low -t recoil protons, however, made a large angle (up to 45 degrees) to the wire plane and several adjacent wires could be set. The coordinate of this "cluster" was taken as the mean of the location of all set adjacent wires. Up to seven wires were used to define one cluster coordinate. If there were more than seven adjacent wires then two clusters were defined. If there was more than 14 clusters in one chamber then the chamber was not used in the reconstruction.

The track finding algorithm was designed to be as efficient as possible despite chamber inefficiencies (typically 5-20%), extraneous cluster coordinates and the gap between the wire

chambers in the downstream part of the recoil spectrometer. A track segment finding routine (Figure A10.3) was used, with the groups of chambers (Pattern Recognition Groups) and parameters defined in Table A10.1, to find two dimensional straight segments of the trajectories. Up to 60 slopes and intercepts were stored for each of the six pattern recognition groups.

The track finding algorithm can be summarized as follows:

The track segment finding routine was used to search for an elevation (y) track segment in the forward arm. Then it was used on the upstream forward plan (x) view. If between 1 and 14 track segments were defined then "dummy" clusters were defined as the position of each track segment at the z coordinate of the effective magnet center plane. Using the "dummy" clusters a search was made for track segments in the forward downstream plan (x) view. The downstream track segments were used to define dummy clusters at the magnet center plane and a search for x upstream track segments was done again. If track segments were not defined for all three views then the algorithm was not continued.

The recoil spectrometer presented problems, not only because of the large gap between the wire chambers but also because of the large angles of entry and exit to the magnetic field and a large amount of vertical focusing in the magnetic field. Because of this last problem the downstream recoil y chambers were not used in

the event reconstruction. The algorithm continued by searching for an elevation (y) view recoil track segment. Next the track segment routine was used to search for downstream x track segments with at least three chambers. Any track could go through at most four of the x downstream recoil chambers.

Next two chamber track segments were defined with the provision that they either went through the gap between the chambers (gap track segments) or missed the first two downstream recoil chambers r7x and r8x (wide track segments). To take into account the finite resolution of the wire chambers the gap and chamber edge apertures were taken to be 12.5 mm larger than actual size. If no track segment was defined at this point then two chamber track segments were defined first using the track segment finding routine (this limits the two chambers to the possible anchor chambers) and then using all other pairs of chambers.

Next all pairs of clusters between the two upstream recoil chambers were used, in turn, to define a slope and intercept. The pair was stored as a track segment if it intersected the fiducial volume of the hydrogen target (as defined in Figure A10.3) and matched at least one of the downstream segments. This test was relaxed if the downstream track segment was of the wide type defined above. The matching took into account the large angles of the trajectories to the field. To do this, the recoil magnet was considered

as producing a "square" field which vanished everywhere but between Z_{in} and Z_{out} (Figure A10.5), where it had only a vertical component and was uniform throughout this region. A charged particle traversing the field would move in a circular path and the intersection of the ingoing and outgoing particle trajectories occurred at a point

$$Z_{int} = Z_c + \frac{W}{2} \tan\left(\frac{\theta_{in} + \theta_{out}}{2}\right) \tan\left(\frac{\theta_{in} - \theta_{out}}{2}\right) \qquad (1)$$

where

$$Z_c = \frac{Z_{out} + Z_{in}}{2}$$

and

$$W = \frac{Z_{out} - Z_{in}}{2}$$

and θ_{in} and θ_{out} are the ingoing and outgoing angles respectively. The value of W was determined from the data by using a survey value of Zc and inverting equation (1). Reconstructed tracks were used to define the angles.

If no satisfactory pairs were found an attempt was made to define a track through the magnet with only one upstream chamber. This was necessary, not just to recover the tracks in which one of these chambers did not work, but also to determine the efficiency of these chambers. The upstream track segment was defined using a cluster in one of r1x or r3x and the x position of the downstream

track segment at Z_c. The slope of the upstream track segment was used with the downstream track segment and equation (1) to define Z_{int}. The slope and intercept was recalculated with the cluster and the position of the downstream track segment at Z_{int}. This procedure was iterated until the change in Z_{int} from step to step was less than .02 mm.

2. Event Selection

At this point only events with at least one track segment in each of the six views were retained. All combinations of track segments were tested. A given combination of track segments was used to define three dimensional trajectories (see Table A10.2) of the scattered hadron and recoil proton. The variables defined in Table A10.4 were calculated using the analysis constants in Table A10.3. The combination was tested with the seven functions defined in Table A10.5. The functions were expected to be zero on the basis of the expected event geometry (the tracks should be continuous through the analysis magnets and should meet in the hydrogen target) and elastic kinematics (four-momentum should be conserved by the two particle system). The distribution of these functions had finite width corresponding to the experimental resolution.

Events in which one or more combinations had function values falling within 9 of the initial resolution estimates given in Table A10.5 were written to a summary magnetic tape. Special allowances

were made for combinations which had wide or gap track segments and ones in which r4x was not used. The combinations within an event (if there was more than one) were ordered by a χ^2 like estimation defined as the sum of the square of the functions divided by their resolutions. Only the best 16 combinations were written to a summary tape. The summary tapes were studied and "fine-tuning" of the analysis constants was done to center the distributions of these functions. Typical adjustments are shown in Table A10.3. The adjustments to the beam angle parameters, DXB and DYB, were needed because of minor deviations of the incident beam angle. The measured direction cosines were rotated into the perturbed beam coordinate system.

Final cuts were made at three standard deviations and the closest approach of the tracks limited to the hydrogen target volume (Table A10.6). Finally, fiducial cuts were made (Table A10.7). The fiducial cuts limited the effective aperture of the spectrometer and in particular eliminated events with wide track segments. The target fiducial cut eliminated events that came from the interaction with the target flask ends rather than the hydrogen. The distributions are shown in Figures A10.6-A10.12. In these figures all cuts (including fiducial cuts) have been made except the one associated with the distribution.

The events were binned according to their value of t. This value was determined from the measured recoil scattering angle

because of the approximate independence of t, as a function of the recoil angle, on the incident momentum (Equation A9.16).

Table A10.1

Pattern recognition groups

View	Chamber	Road width (mm)	Anchor chambers 1	2	3	4	5	6	7	8	Required number
1 Recoil y	r2y	13.6	x		x						
	r3y	2.7		x	x						2
	r5y	13.6	x	x							
2 Forward[1] y	f1y	3.0	x		x		x		x		
	f3y	4.4		x		x		x		x	
	f6y	2.7							x	x	3/2
	f10y	3.4					x	x			
	f12y	3.3	x	x							
	f15y	7.8			x	x					
3 Recoil[2] up x	r1x										
	r2x										
4 Recoil[3] down x	r6x	9.5	x	x			x	x			
	r7x	10.9			x	x			x	x	
	r8x	8.1		x		x					3/2
	r9x	8.1					x		x		
	r10x	7.6	x		x						
	r11x	7.8					x		x		
5 Forward up x	f2x	6.2	x		x		x				
	f4x	4.4		x		x		x			2
	f5x	2.7			x	x					
	f9x	3.1	x	x							
	dummy	12.3					x	x			
6 Forward down x	dummy	12.3	x	x							
	f11x	3.3					x	x			2
	f13x	2.7			x	x					
	f14x	3.0		x		x		x			
	f16x	4.0	x		x		x				

[1] Three clusters were required if the outside pretrigger worked. If the pretrigger did not work then only two clusters were needed.

[2] This pattern recognition group was not used with the track segment algorithm.

[3] Three clusters were required on the first pass and only two on the next (see text).

Table A10.2

Trajectory parameterization

DXjk	the horizontal slope of the j = u, d (upstream, downstream) k = f, r (forward, recoil) trajectory
DYjk	the vertical slope
XOjk	the horizontal intercept at z (or z′) = 0
YOjk	the vertical intercept
DCjk = [DCjkx, DCjky, DCjkz]	the direction cosine vector $DC_{jk} = \frac{[DX_{jk}, DY_{jk}, 1]}{\sqrt{1 + DX_{jk}^2 + DY_{jk}^2}}$
POjk	the intercept vector defined by POjk = [XOjk, YOjk, O] DCjk and POjk are vectors and are denoted with a prime is expressed in the recoil coordinate system. The trajectories are parameterized by

Table A10.3

Analysis constants

		Initial value		Typical adjustment
P1	incident beam momentum	100.0	200.0 GeV/c	1 %
DXB	horizontal beam angle	0.0	0.0	.05 mr
DYB	vertical beam angle	0.0	0.0	.05 mr
FBDL	forward magnet field integral	1.02	2.04 GeV/c	.5 %
RBDL	recoil magnet field integral	.270	.270 GeV/c	.5%
W	recoil magnet width	76.2	76.2 cm	8 cm
ZF	forward magnet center plane	31.70	31.70 m	.02 m
ZR	recoil magnet center plane	1.53	1.53 m	-

Table A10.4

Measurement variable definitions

DXF	Forward track segment matching parameter. This is the difference between the position of the upstream and downstream track segments at the magnet center. $DXF = ZF(DX_{df}-DX_{uf}) + (XO_{df}-XO_{uf})$
DXR	Recoil track segment matching parameter. The difference in position is calculated at Z_{int} the expected position of meeting (see text). $DXR = Z_{int}(DX_{dr}-DX_{ur}) + (XO_{dr}-XO_{ur})$
PT = [XT, YT, ZT]	The coordinates of the center point of closest approach of the recoil and forward trajectories.
PD = [XD, YD, ZD]	Vector of this closest approach.
TF	The measured t based on the forward scattering angle and elastic kinetmatics.
TR	The measured t based on the recoil scattering angle.
PF	The expected momentum of the forward particle based on the forward scattering angle.
PFM	The measured forward momentum. $PFM = FBDL/(DC_{dfz}-DC_{duz})$
PR	The expected momentum of the recoil proton based on the recoil scattering angle
PRM	The measured recoil momentum. $PRM = RBDL/(DC'_{drz}-DC'_{drz})$
CPL	Coplanarity, i.e. the cosine of angle between the beam axis and the normal to the scattering plane.

$$CPL = (DC_{fux}DC_{ruy}-DC_{fuy}DC_{rux}) \Big/ \sqrt{1+\Sigma_{i=1}^{3} DC_{fui}DC_{rui}}$$

Table A10.4 (continued)

XRA, YRA	The position of the measured recoil trajectory at r6x, i.e. $z' = 2.17$ m.
XFA, YFA	The position of the measured forward trajectory at H3, i.e. $z = 35.26$ m.

Table A10.5

Resolutions used for initial cuts

Cut	Mnemonic name	Definition	Exceptions	± 100 GeV	± 200 GeV	Units
1	forward track	DXF		.686	.686	mm
2	recoil track	DXR		.315	.315	mm
			wide	4.32	4.32	mm
			gap	4.32	4.32	mm
3	forward momentum	$\frac{PF-PFM}{PF}$		.0075	.0075	
4	recoil momentum	$\frac{PR-PRM}{PR}$		.124	.124	
			wide	5.	5.	
			gap	5.	5.	
5	target closest approach	YD		2.72	2.72	mm
6	coplanarity	CPL		.00014	.00014	
7	t difference	$\frac{TF-TR}{a+b\lvert TF\rvert}$				
		$a = .013\,(GeV/c)^2$		1.		
		$b = .014\,(GeV/c)^2$				
			no r4x	1.533		
		$a = .033\,(GeV/c)^2$			1.	
		$b = .017\,(GeV/c)^2$				
			no r4x		1.533	

[1] Initial cuts were made at ± 9 times the above defined resolutions. The resolutions were widened for events which used wide or gap (defined in text) downstream x recoil track segments and events in which proportional wire chamber r4x was not used. The column headed "Definition" gives the distribution in terms of the measured variables defined in Table A10.4.

Table A10.6

Final event selection criteria

Cut	Mnemonic name	Definition	Exceptions	-200	-100	+100	+200	Units
1	forward track	DXF		2.44	2.06	2.06	2.44	mm
2	recoil track	DXR		17.5	23.6	26.4	13.2	mm
			wide gap	83.8 31.2	83.8 31.2	83.8 31.2	83.8 31.2	mm mm
3	forward momentum difference	$\frac{PF-PFM}{PF}$		.0207	.0225	.0225	.0207	
4	recoil momentum difference	$\frac{PR-PRM}{PR^2}$		.048	.099	.099	.048	$(GeV/c)^{-}$
			wide gap	.141 .105	.372 .186	.372 .186	.141 .105	$(GeV/c)^{-1}$ $(GeV/c)^{-1}$
5	target closest approach	YD		5.87	6.71	6.71	5.87	mm
6	target volume	XT YT ZT		38.1 38.1 50.8	38.1 38.1 50.8	38.1 38.1 50.8	38.1 38.1 50.8	mm mm cm
7	coplanarity	CPL		.420	.420	.354	.285	$\times 10^{-3}$
8	t difference	$\frac{TF-TR}{a+b\lvert TF\rvert}$						
		a = .0462 b = .0238		3.			3.	
			no r4x	5.1			5.1	
		a = .0182 $(GeV/c)^2$ b = .0154			3.		3.	
			no r4x		5.1		5.1	

Table A10.7

Fiducial cuts[1]

YRA	-29.85	29.85	cm
YFA	-8.13	8.13	cm
XRA	-109.22	-	cm
XFA	11.00	-	cm
ZT	-50.29	50.29	cm

[1]The quantities in the first column are defined in Table A10.4.

Table A10.8

Event selection history

	Beam momentum (GeV/c)	-200	-100	+100	+200
Initial criteria	Type 1 triggers	3,031,550	1,189,268	109,013	970,289
	With forward track	490,454	958,101	89,952	107,002
	With recoil track	340,898	871,021	82,712	70,358
	Forward momentum	234,852	793,605	72,551	33,768
	Recoil momentum	157,809	743,119	66,969	20,195
	Closest approach	154,890	739,956	66,711	19,725
	Target	148,967	738,581	66,574	19,559
	Coplanarity	143,765	721,105	64,635	17,379
	t difference	131,019	702,641	62,612	14,414
Final selection	One or less criteria not met	122,997	690,437	61,338	12,740
	All criteria met	113,803	651,788	57,989	11,506
	Fiducial cuts	102,788	456,742	39,924	9,866
	Particle separation and t range quoted in Tables 5.1-5.4	75,043	410,963	36,249	7,446
	p	18	3,834	11,412	3,431
	π	74,913	399,757	23,616	3,876
	K	112	7,372	1,221	139

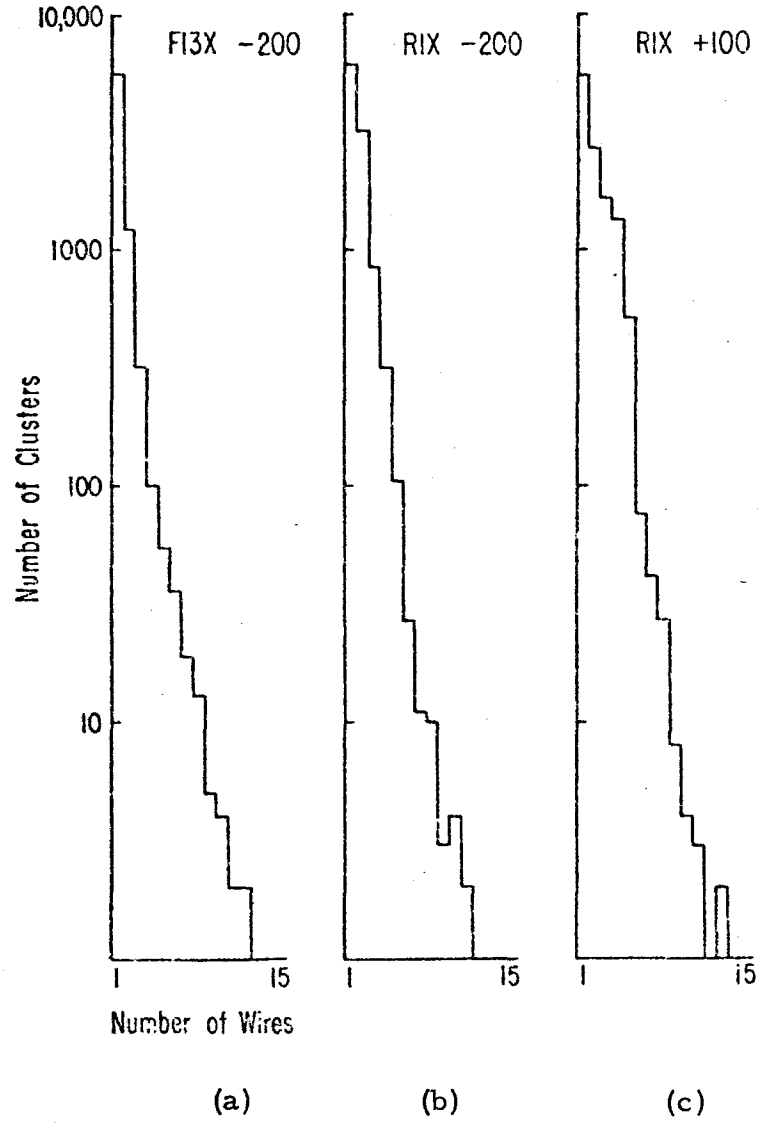

Figure A10.1. Cluster size distribution. The number of clusters is shown as a function of the number of wires in the cluster for:

a) chamber f13x at beam momentum -200 GeV/c
b) chamber r1x at beam momentum -200 GeV/c
c) chamber r1x at beam momentum +100 GeV/c .

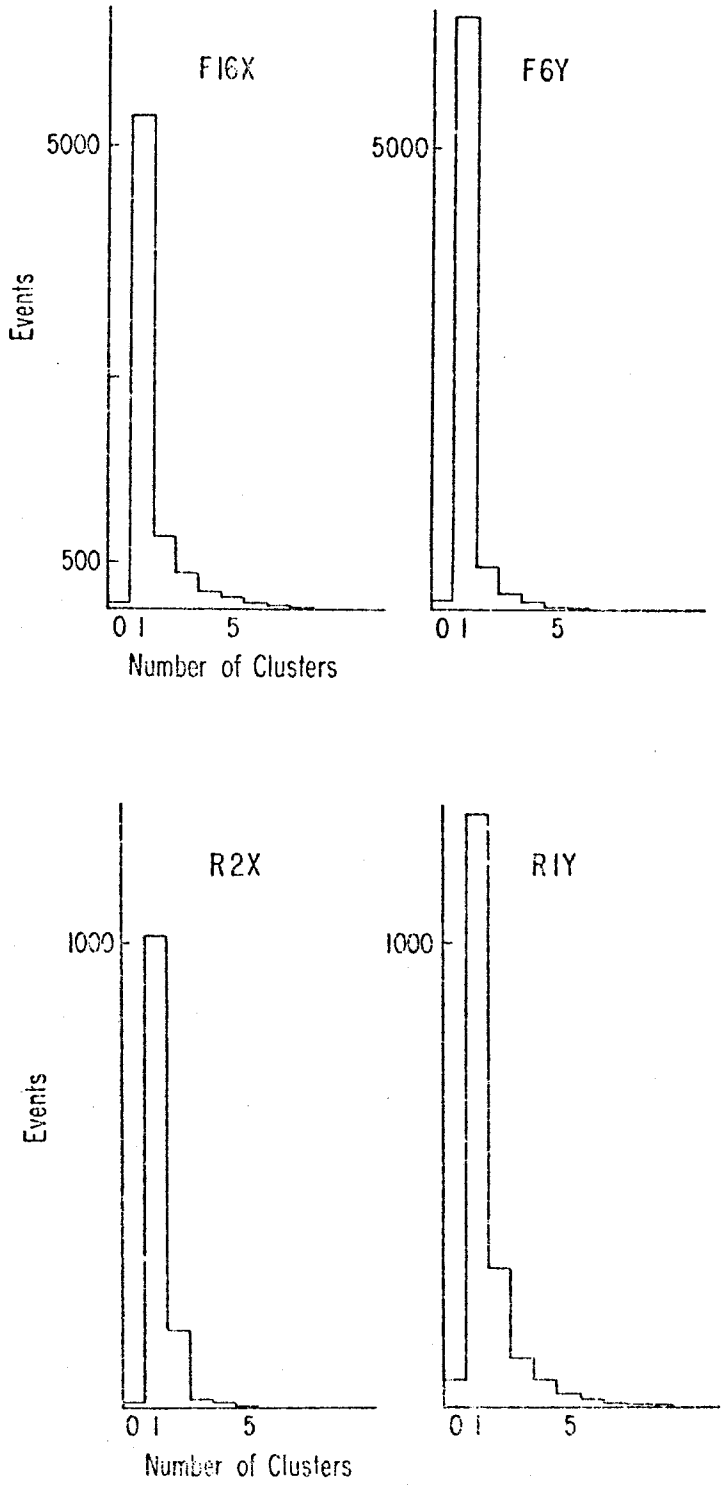

Figure A10.2. Number of clusters per chamber. The number of clusters in one chamber given that a track was reconstructed through its spectrometer is shown. The sample is a subset of the -200 GeV/c data.

Figure A10.3. Track segment algorithm. The following are defined:

I	Anchor pair sequence number. The anchor pair is specified in Table A10.1 by x's placed under the column headed by the sequence number.
J	Track segment candidate sequence number.
K	Sequence number of cluster in anchor chamber 1.
L	Sequence number of cluster in anchor chamber 2.
IMAX	Number of anchor pairs.
JMAX	Maximum allowed number of track segment candidates, JMAX = 60 for all pattern recognition groups.
KMAX	Number of clusters in anchor chamber 1.
LMAX	Number of clusters in anchor chamber 2.
NCH	Number of chambers in the pattern recognition group with at least one cluster.
NCM	Minimum number of clusters required to define a track segment candidate.
NHT	Number of clusters currently required to define a track segment candidate.
NHR	Number of clusters in the current road defined by the anchor chambers. The road for each chamber had a width given in Table A10.1 and was centered on the line segment joining the two clusters of the anchor chambers. If two clusters in one chamber were within the road width then the cluster closest to the road was included in the track segment. The road width value was determined from the distribution of residuals between the cluster coordinate and a fitted track segment defined by other chambers in the pattern recognition group. The value chosen was approximately four standard deviations of the signal. The road width values (divided by 4) were used as weights in a least squares fit of the track segment.
TARGET	Does the road intersect the target fiducial region? The road had to come within 38 mm of the target center at some point along the z axis within 56 mm from the target center.
SUBSET	Is the current track segment candidate a subset of a previously found track segment candidate?

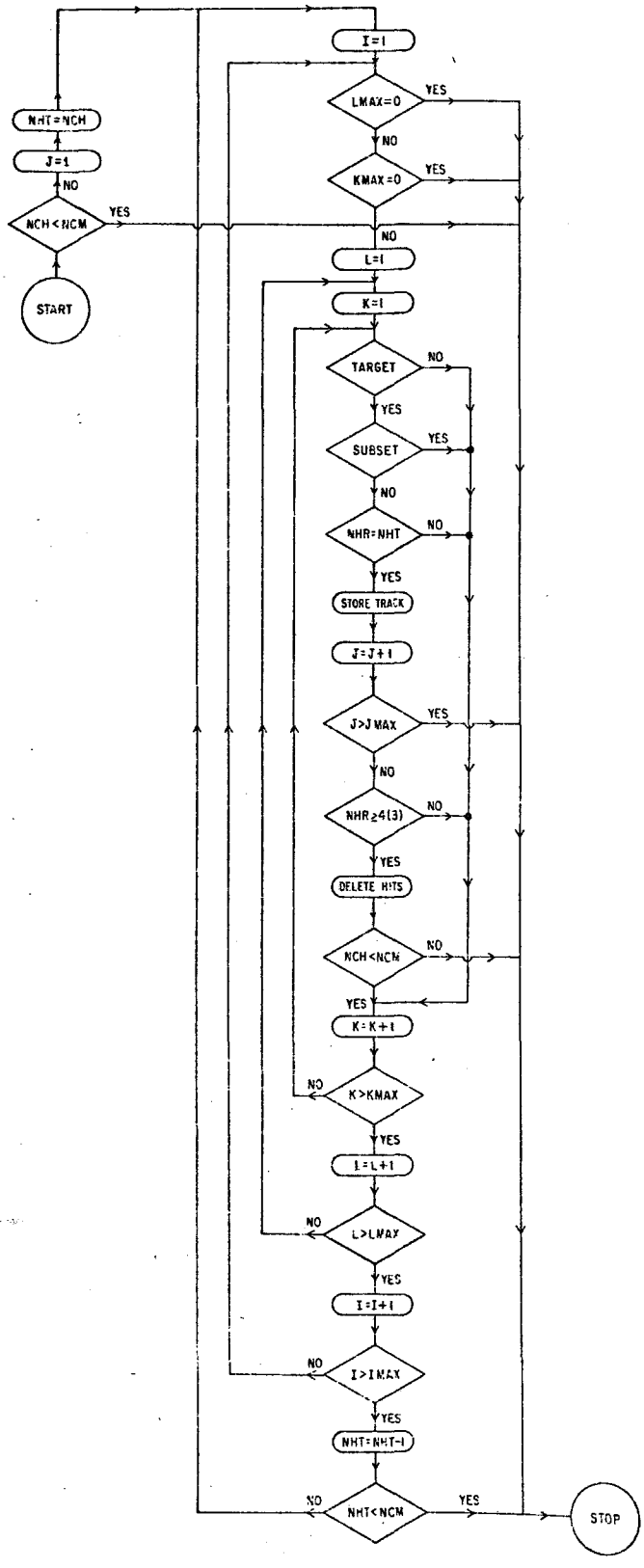
START
NCH<NCM
NO
YES
J=1
NHT=NCH
I=1
LMAX=0
KMAX=0
L=1
K=1
TARGET
SUBSET
NHR=NHT
STORE TRACK
J=J+1
J>JMAX
NHR≥4(3)
DELETE HITS
NCH<NCM
K=K+1
K>KMAX
I=L+1
L>LMAX
I=I+1
I>IMAX
NHT=NHT-1
NHT<NCM
STOP

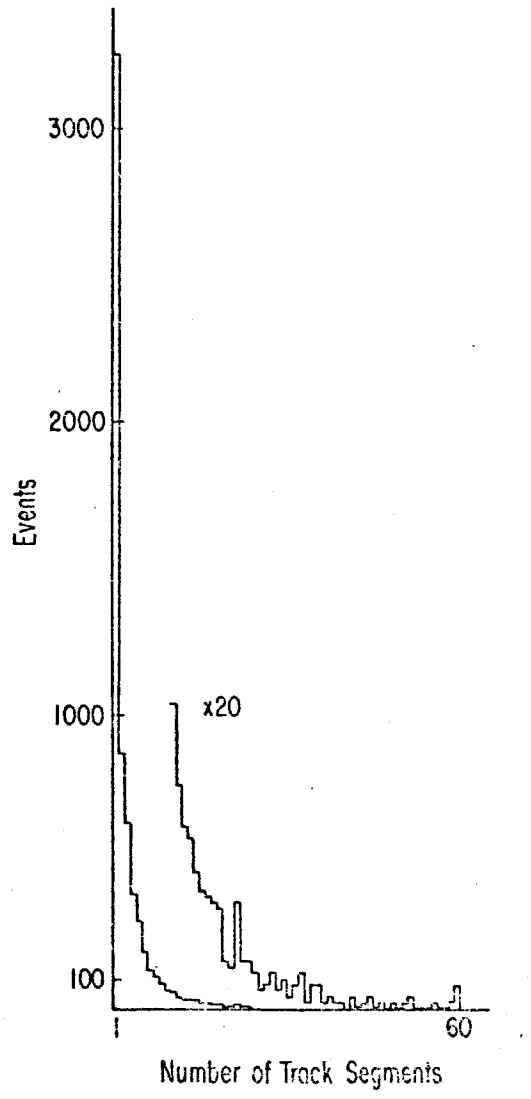

Figure A10.4. Number of track segment candidates. The number of track segment candidates stored for the Y recoil view is shown for a subset of the -200 GeV/c data.

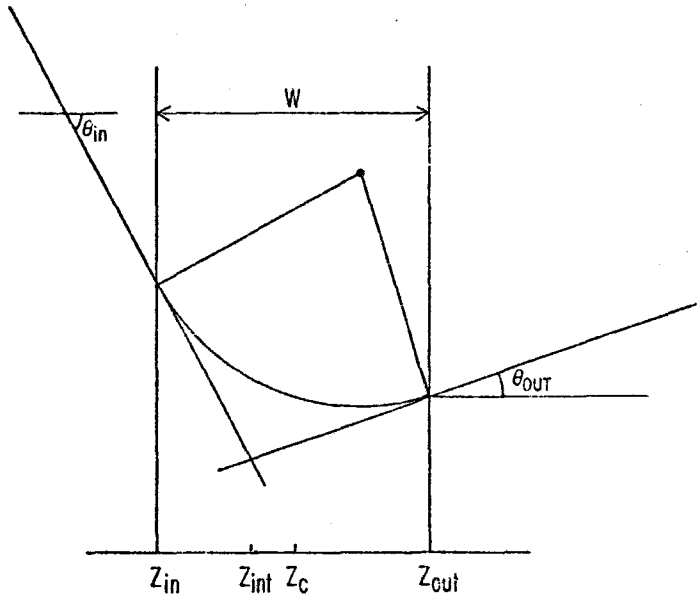

Figure A10.5. The effect of large angles on the magnetic center. The symbols are defined in the text.

Figures A10.6 - A10.12. Geometrical and kinematic distributions used in the event selection. The variables are defined in Table A10.4. In these distributions the data sample is restricted to $-t > .585\ (\mathrm{GeV}/c)^2$ at ± 100 GeV/c and to $-t > .861\ (\mathrm{GeV}/c)^2$ at ± 200 GeV/c. The data samples are for a beam momentum of:

a) +100 GeV/c, b) -100 GeV/c, c) +200 GeV/c and d) -200 GeV/c.

A10.6	DXF (mm)
A10.7	DXR (mm)
A10.8	(PF-PFM)/PF
A10.9	$(PR-PRM)/PR^2\ (\mathrm{GeV}/c)^{-1}$
A10.10	YD (mm)
A10.11	$(TF-TR)/a + b\,\lvert TF \rvert)$ (a, b defined in Table A10.5)
A10.12	CPL

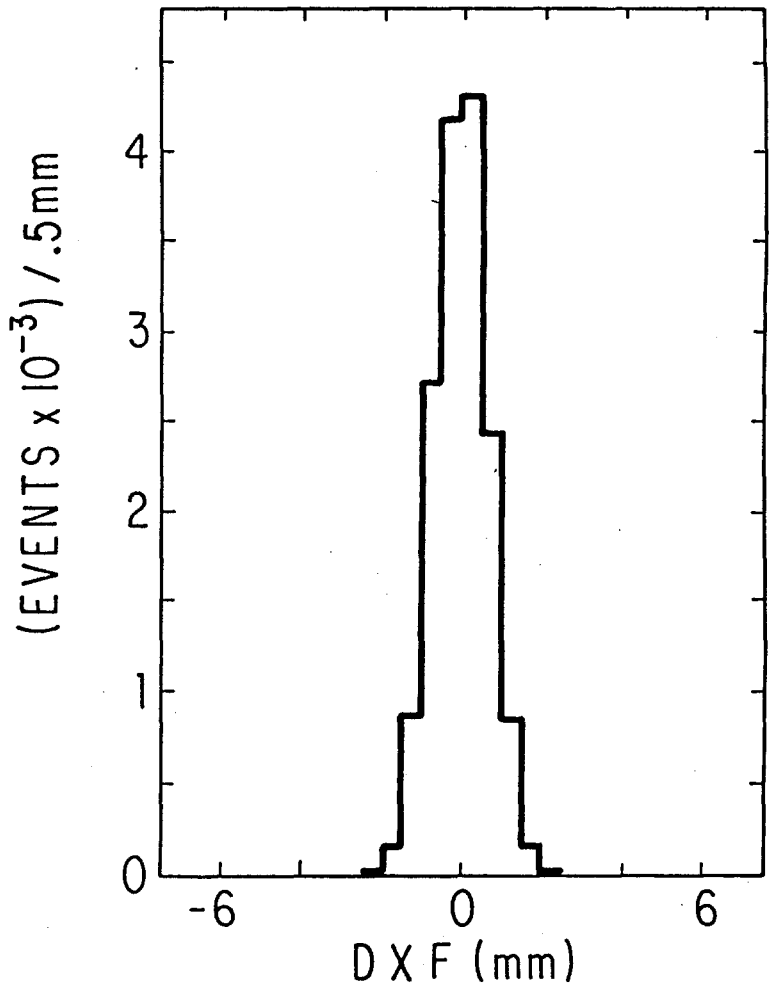

(a)

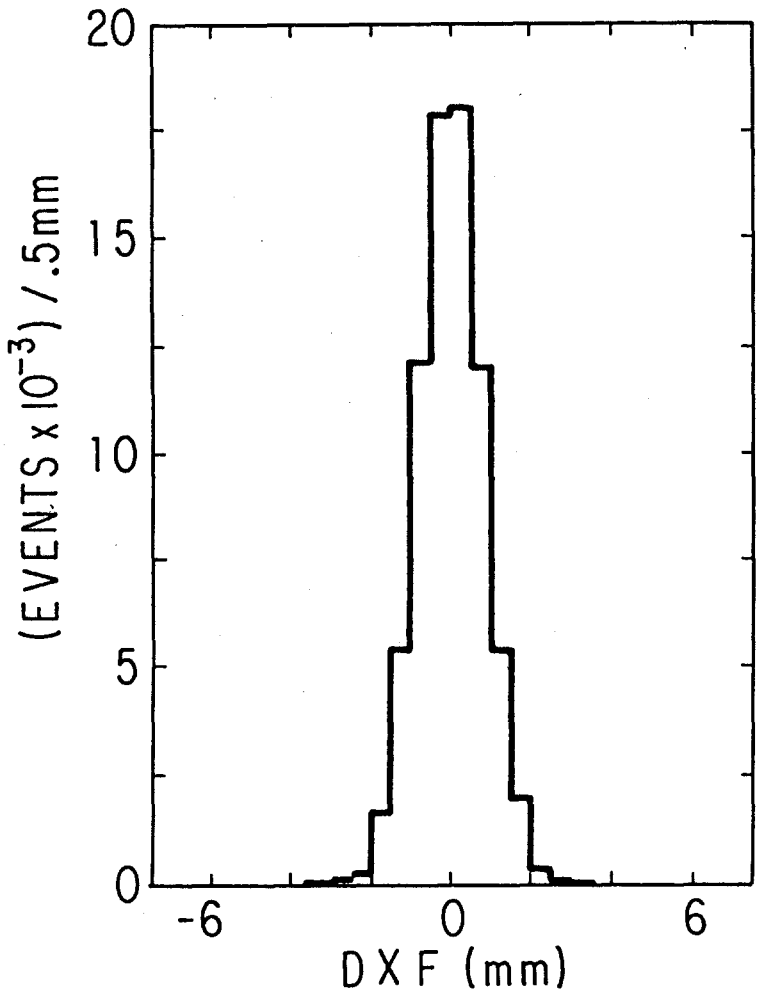

(b)

Figure A10.6

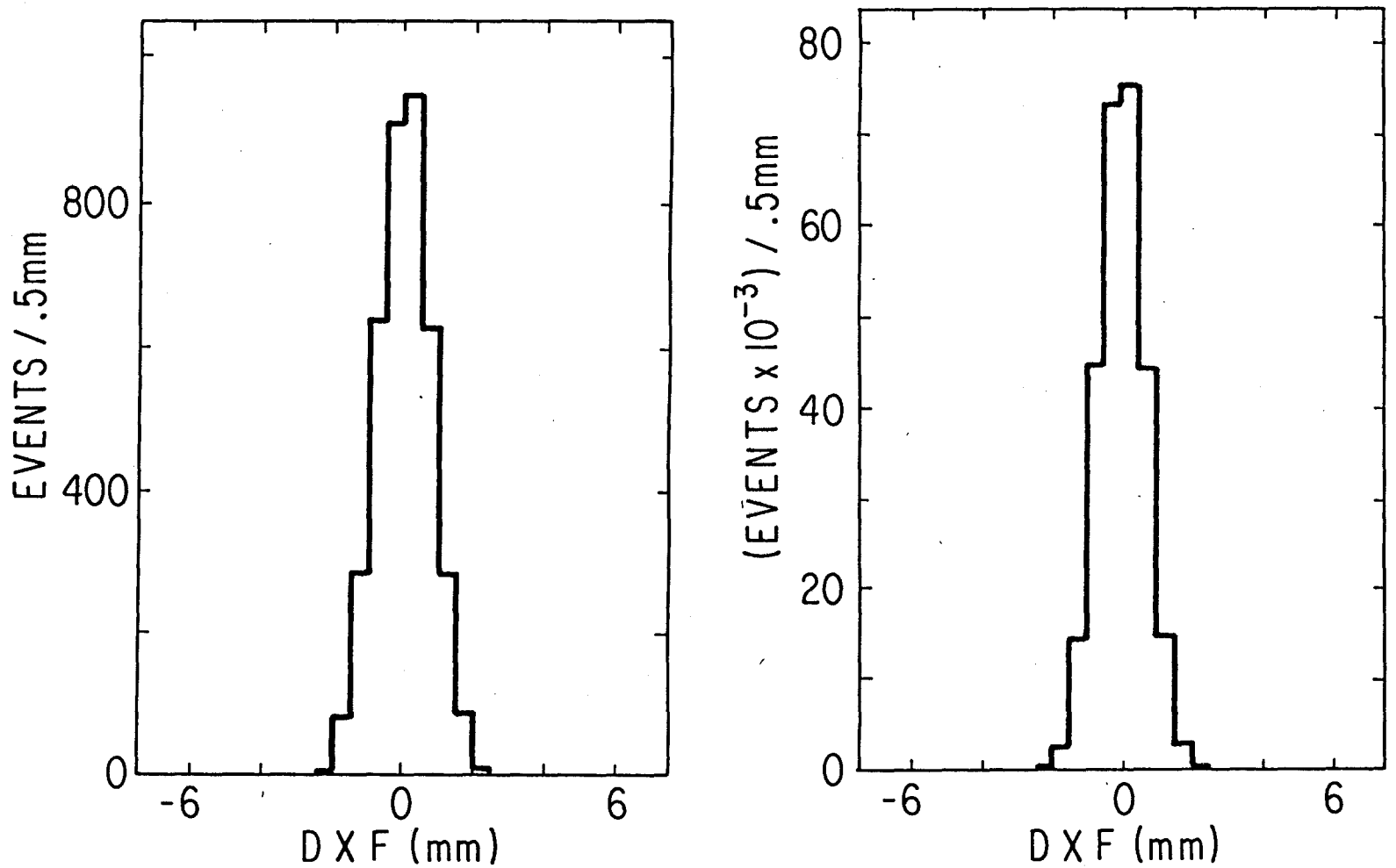

(c) (d)

Figure A10.6 (continued)

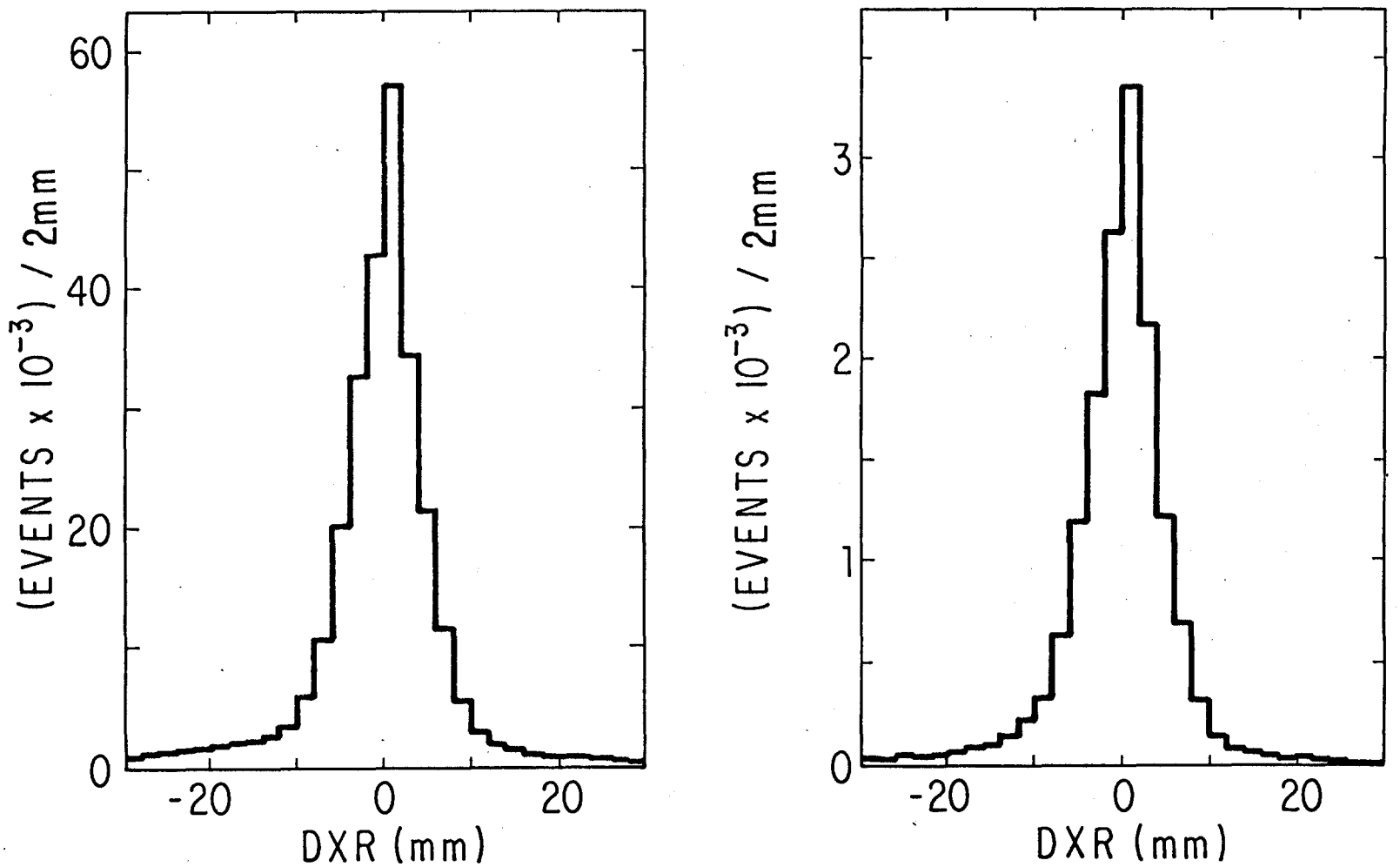
60
40
20
0
(EVENTS x 10^{-3}) / 2mm
-20
0
20
DXR (mm)
(a)
3
2
1
0
(EVENTS x 10^{-3}) / 2mm
-20
0
20
DXR (mm)
(b)

Figure A10.7

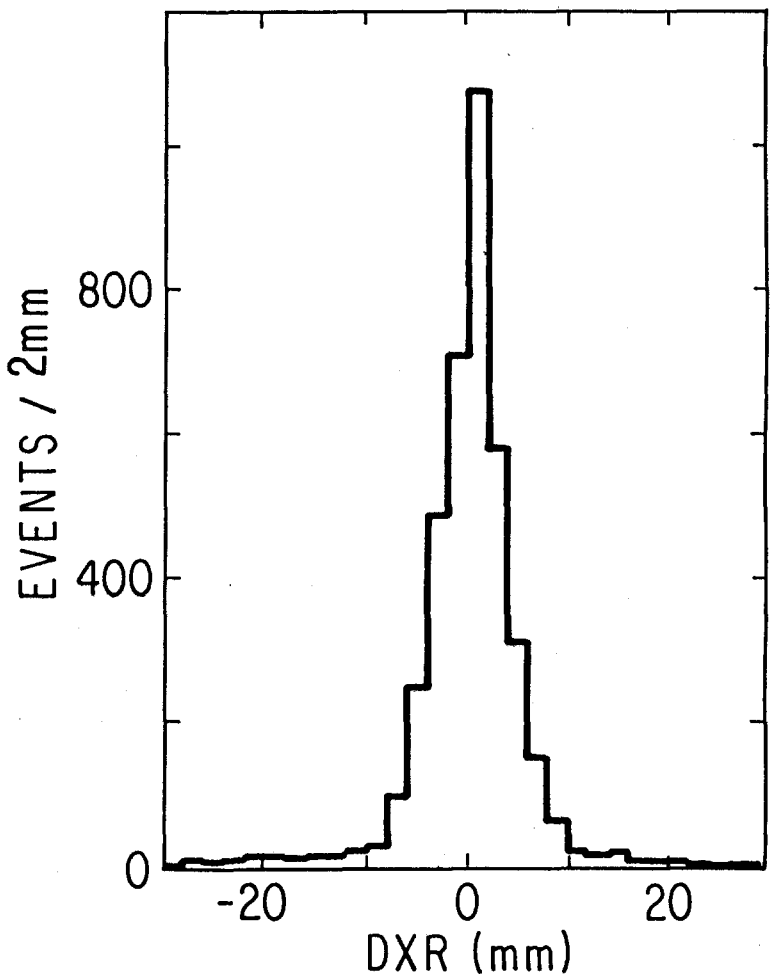

(c)

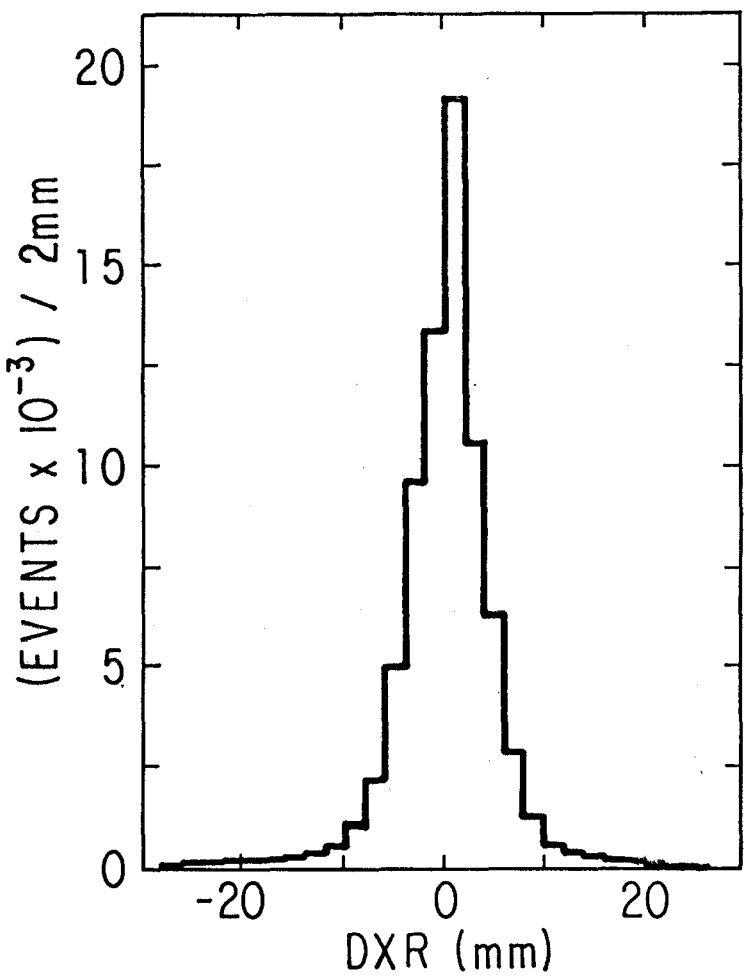

(d)

Figure A10.7 (continued)

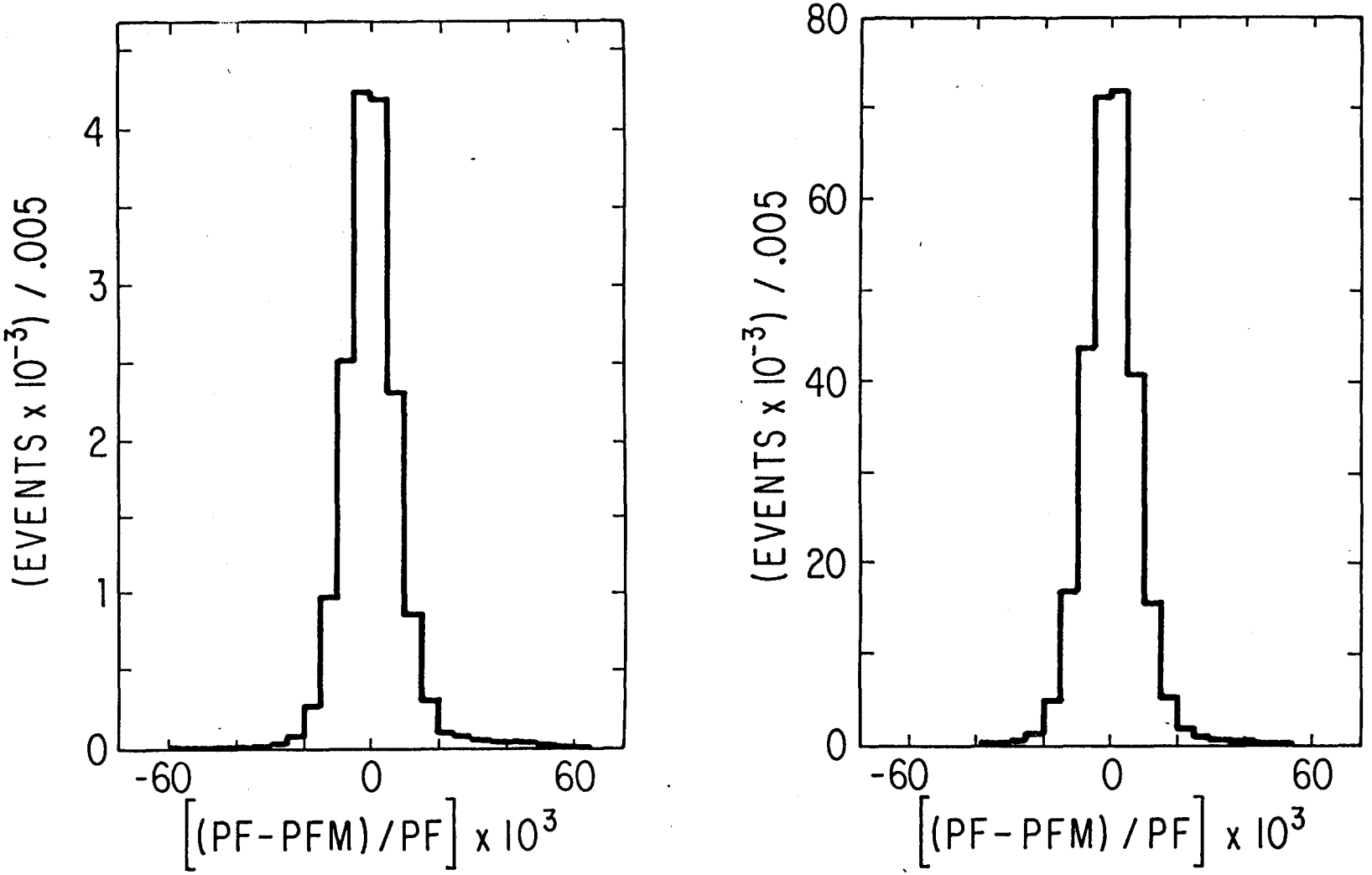
(EVENTS x 10^{-3}) / .005
0
1
2
3
4
-60
0
60
[(PF-PFM)/PF] x 10^3
(a)
(EVENTS x 10^{-3}) / .005
0
20
40
60
80
-60
0
60
[(PF-PFM) / PF] x 10^3
(b)

Figure A10.8

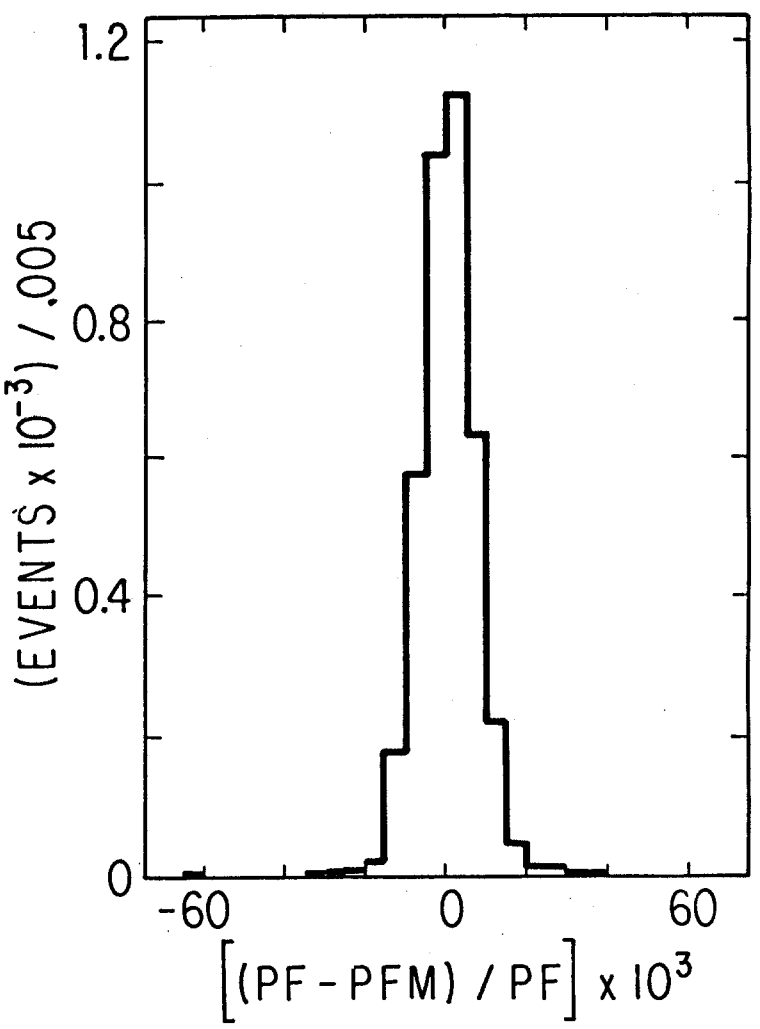

(c)

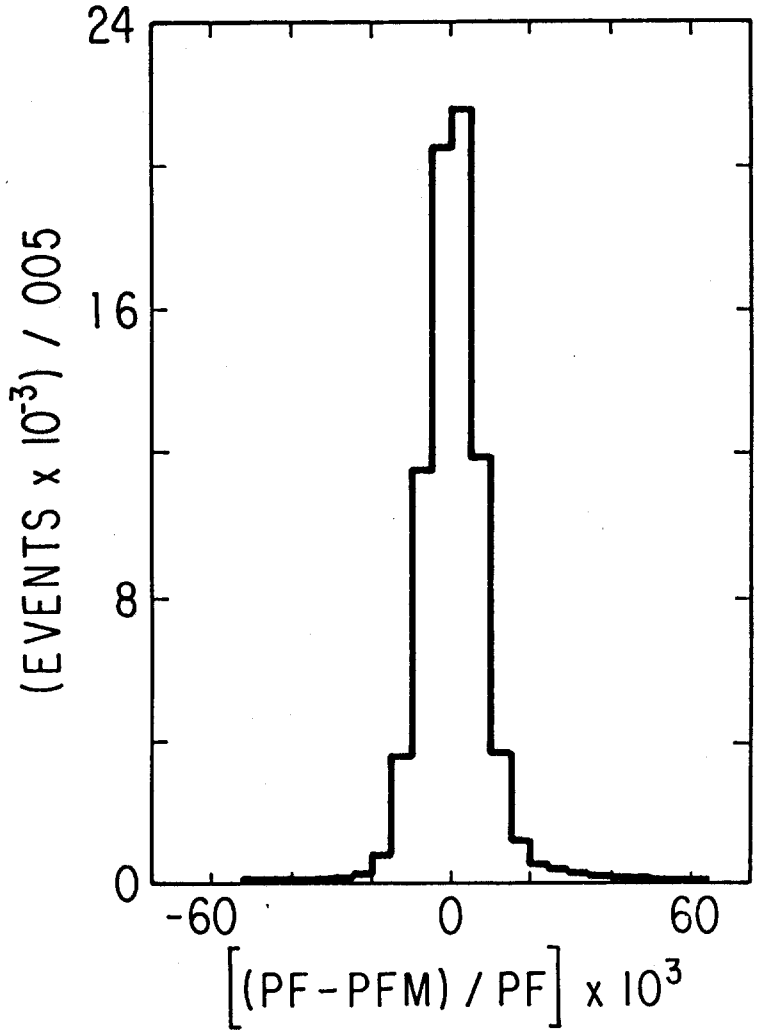

(d)

Figure A10.8 (continued)

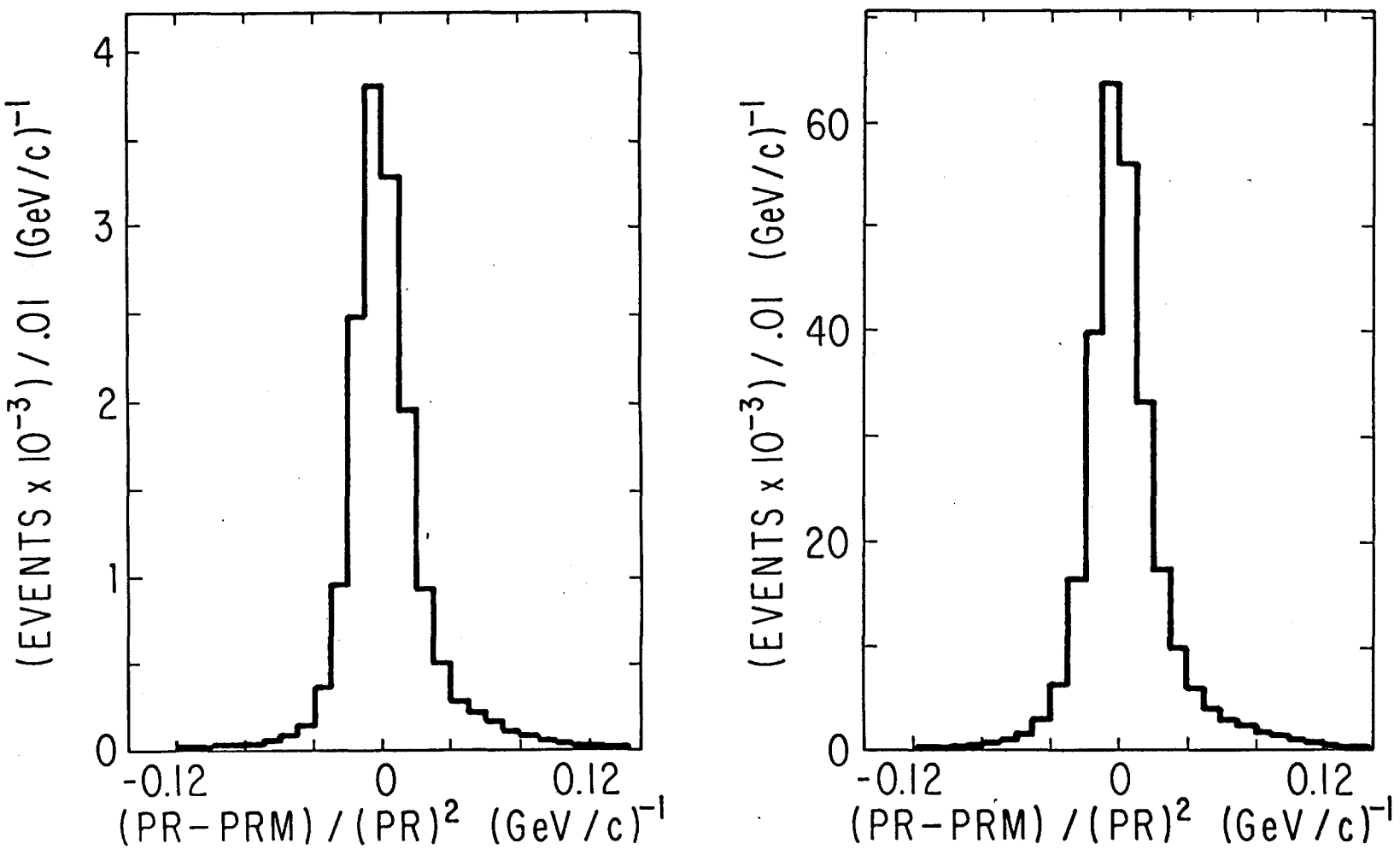

(a) (b)

Figure A10. 9

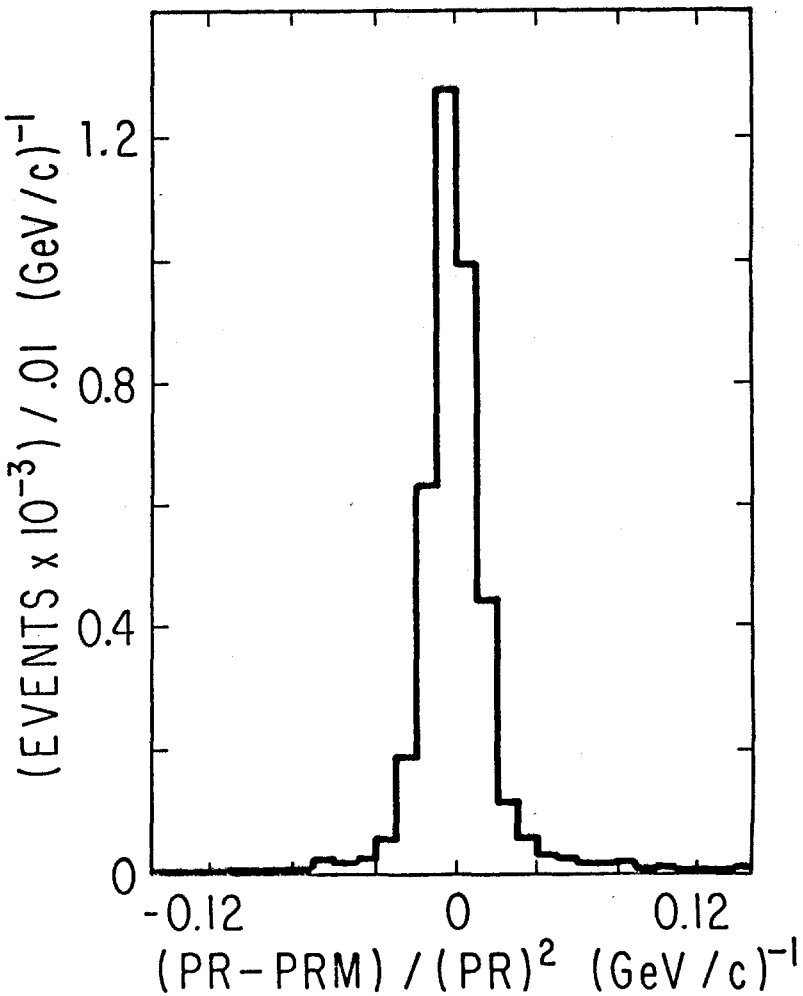

(c)

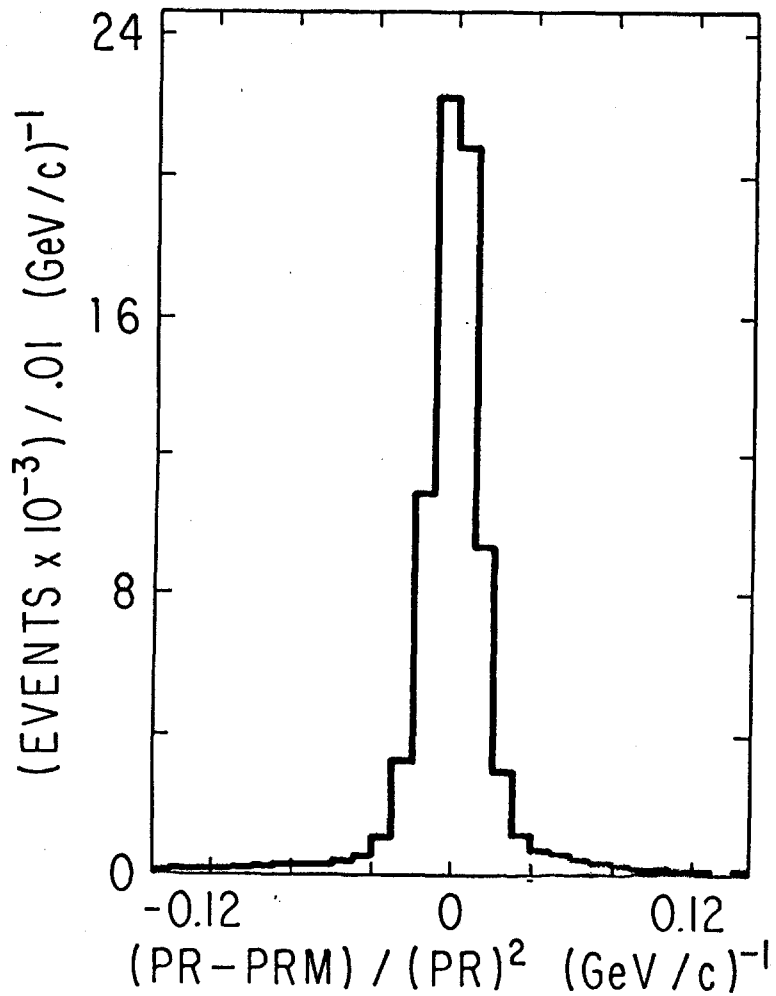

(d)

Figure A10.9 (continued)

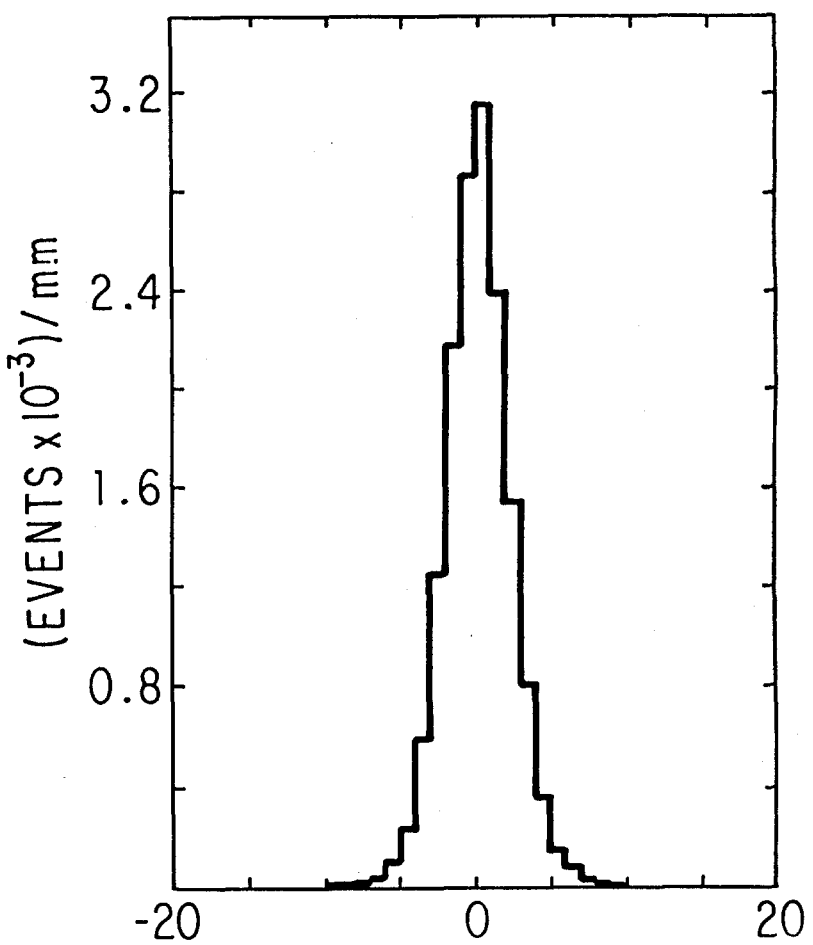

YD (mm)
(a)

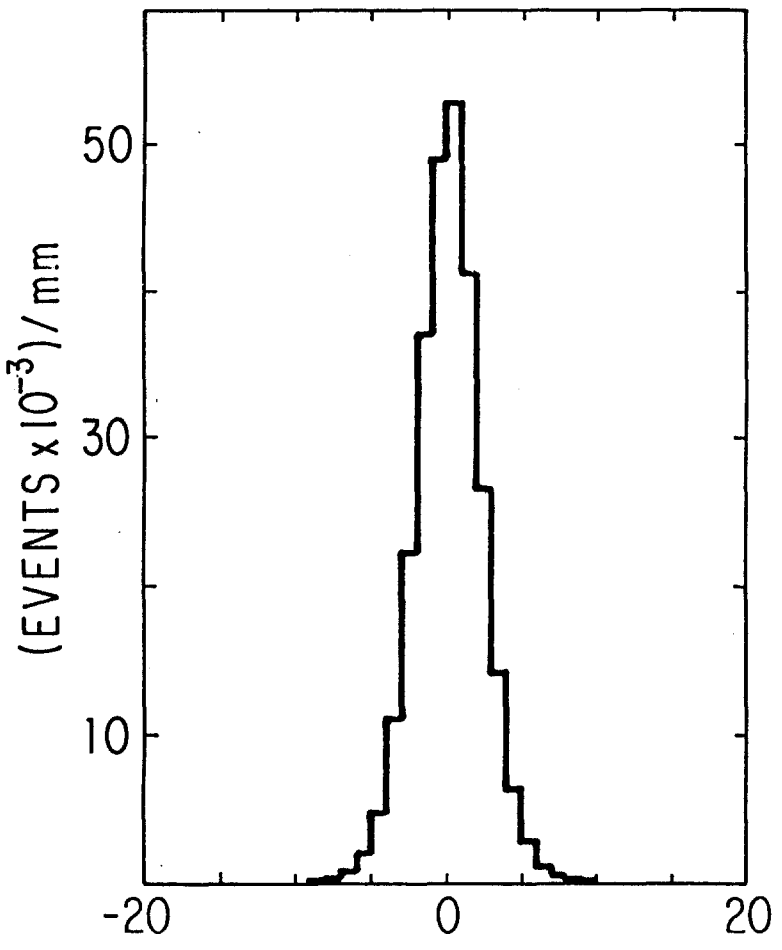

YD (mm)
(b)

Figure A10.10

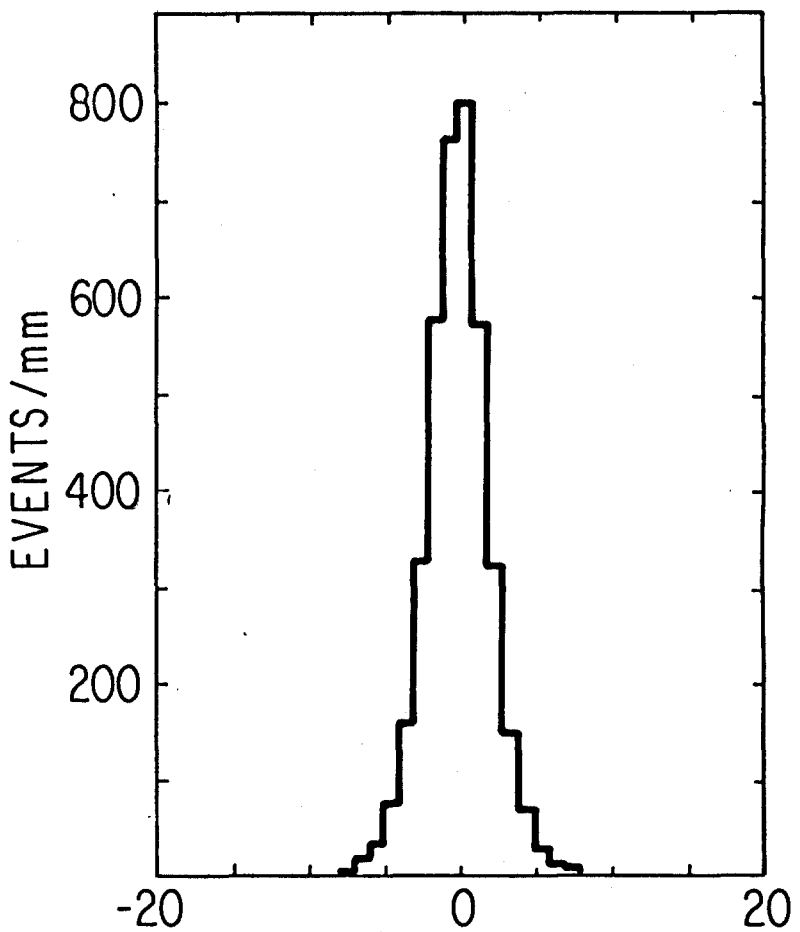

YD (mm)
(c)

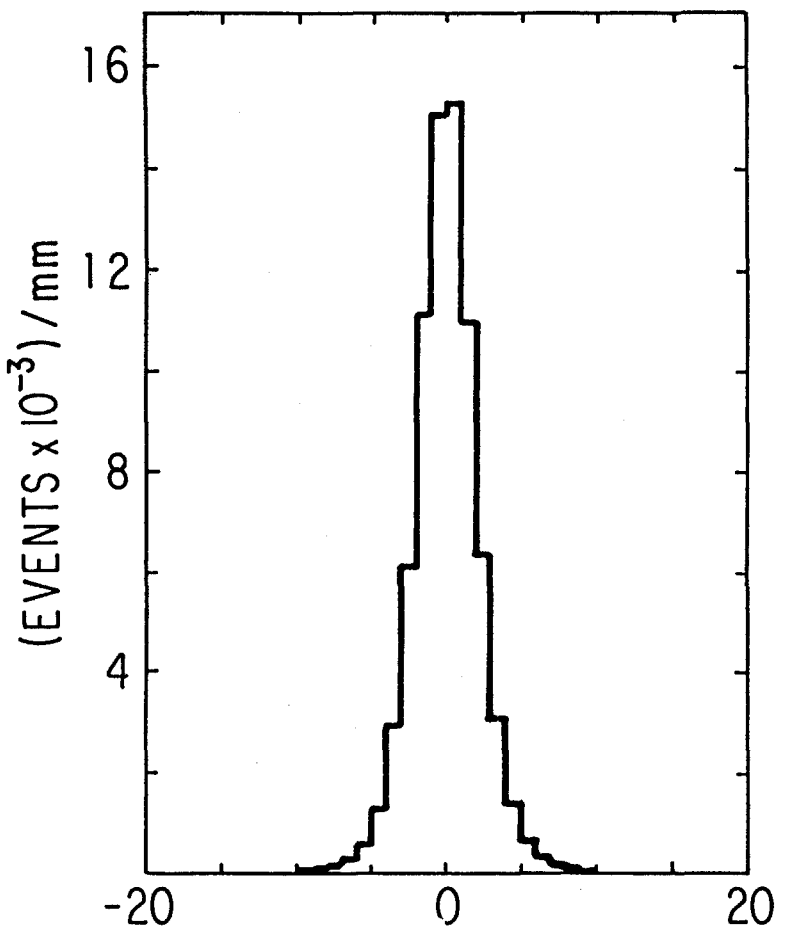

YD (mm)
(d)

Figure A10.10 (continued)

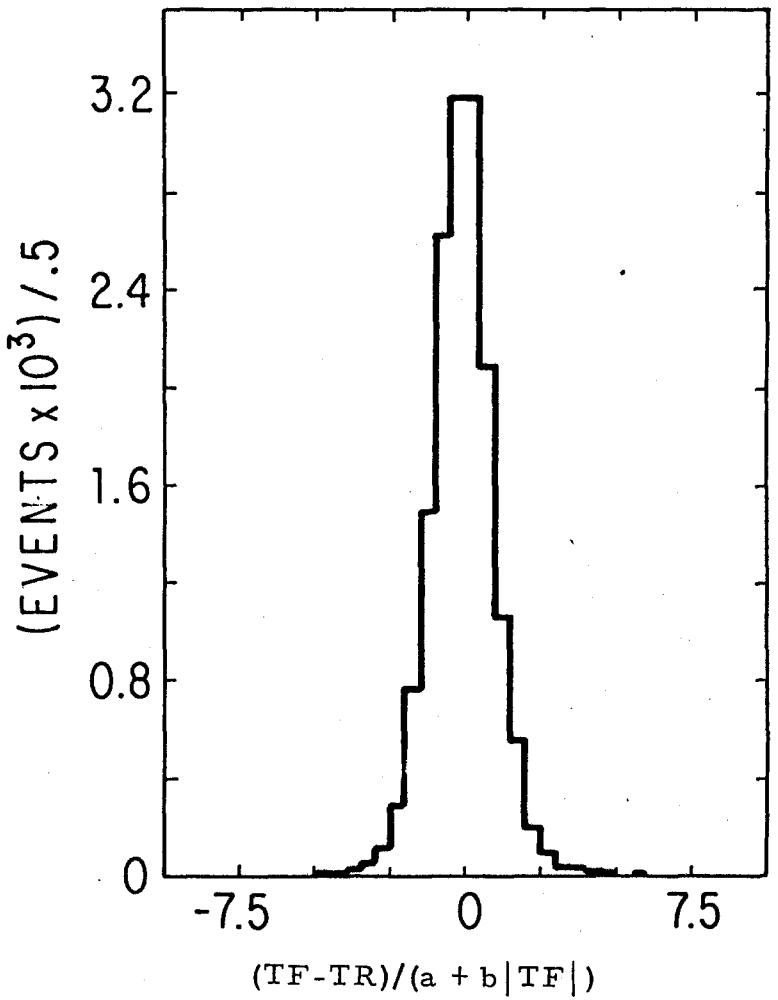

(a)

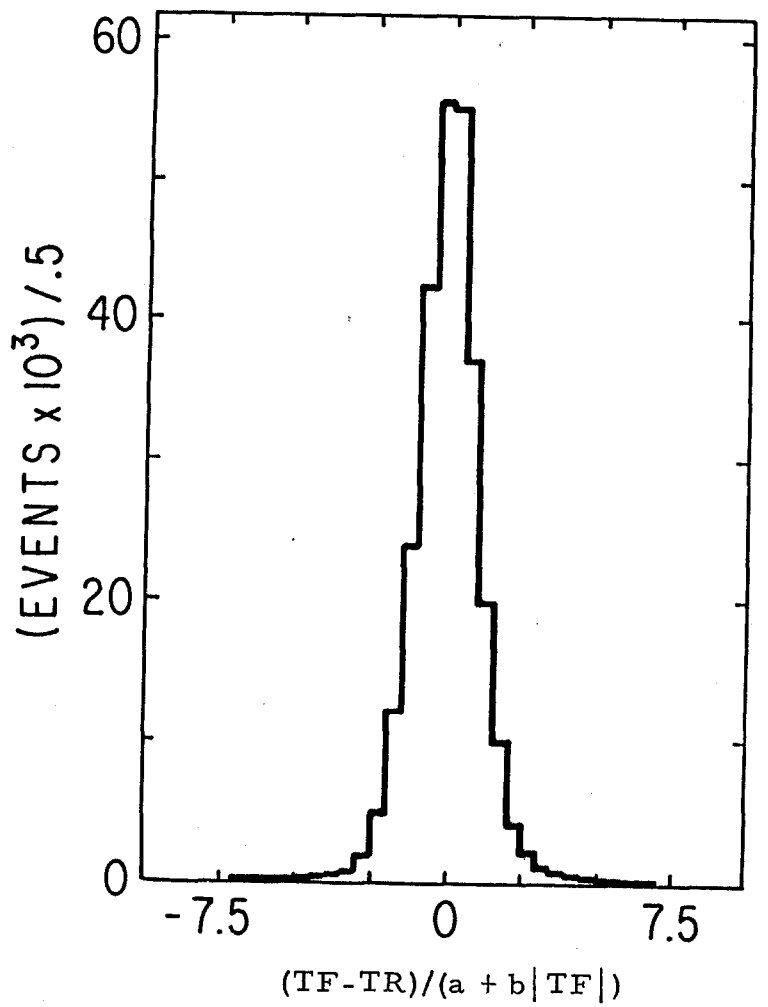

(b)

Figure A10.11

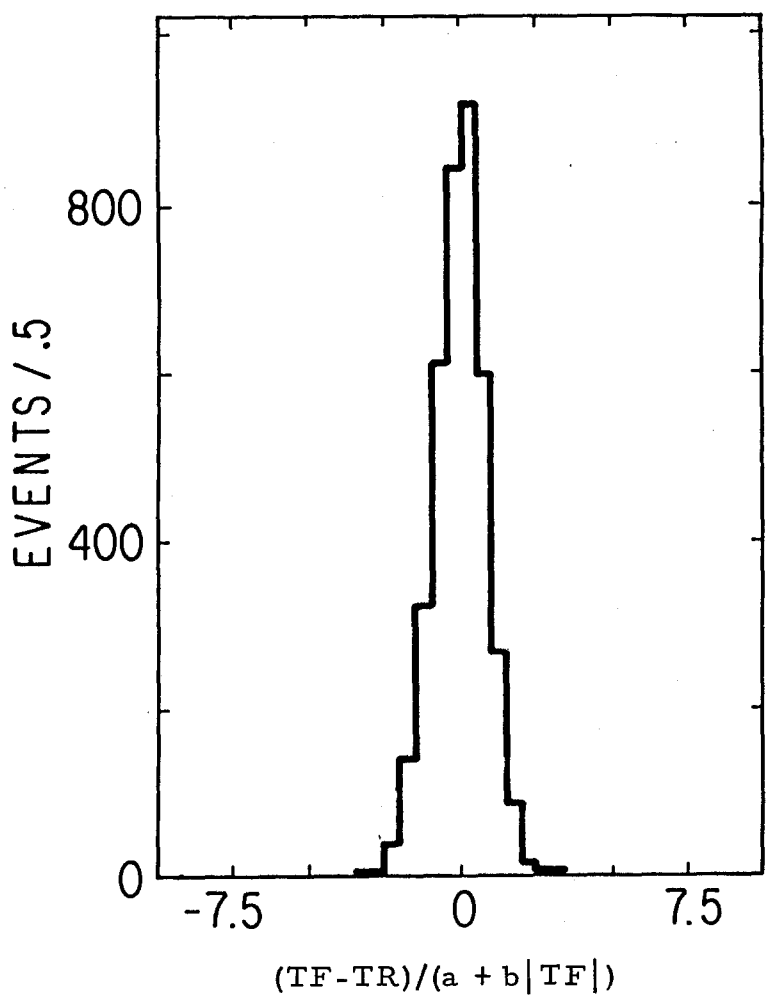

(c)

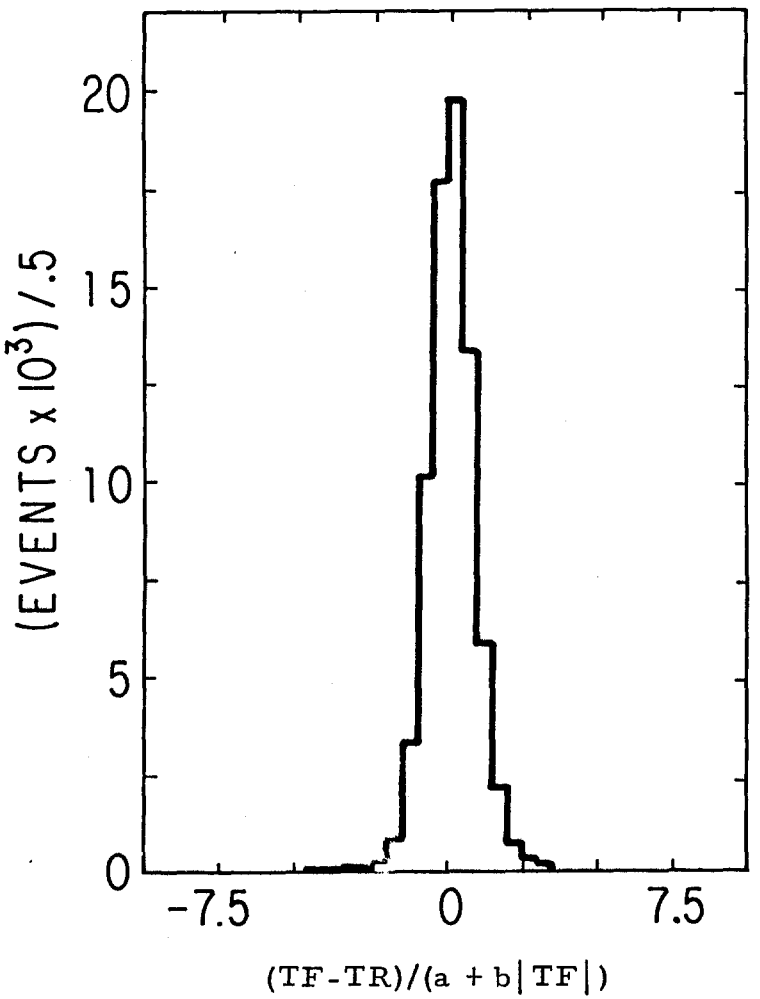

(d)

Figure A10.11 (continued)

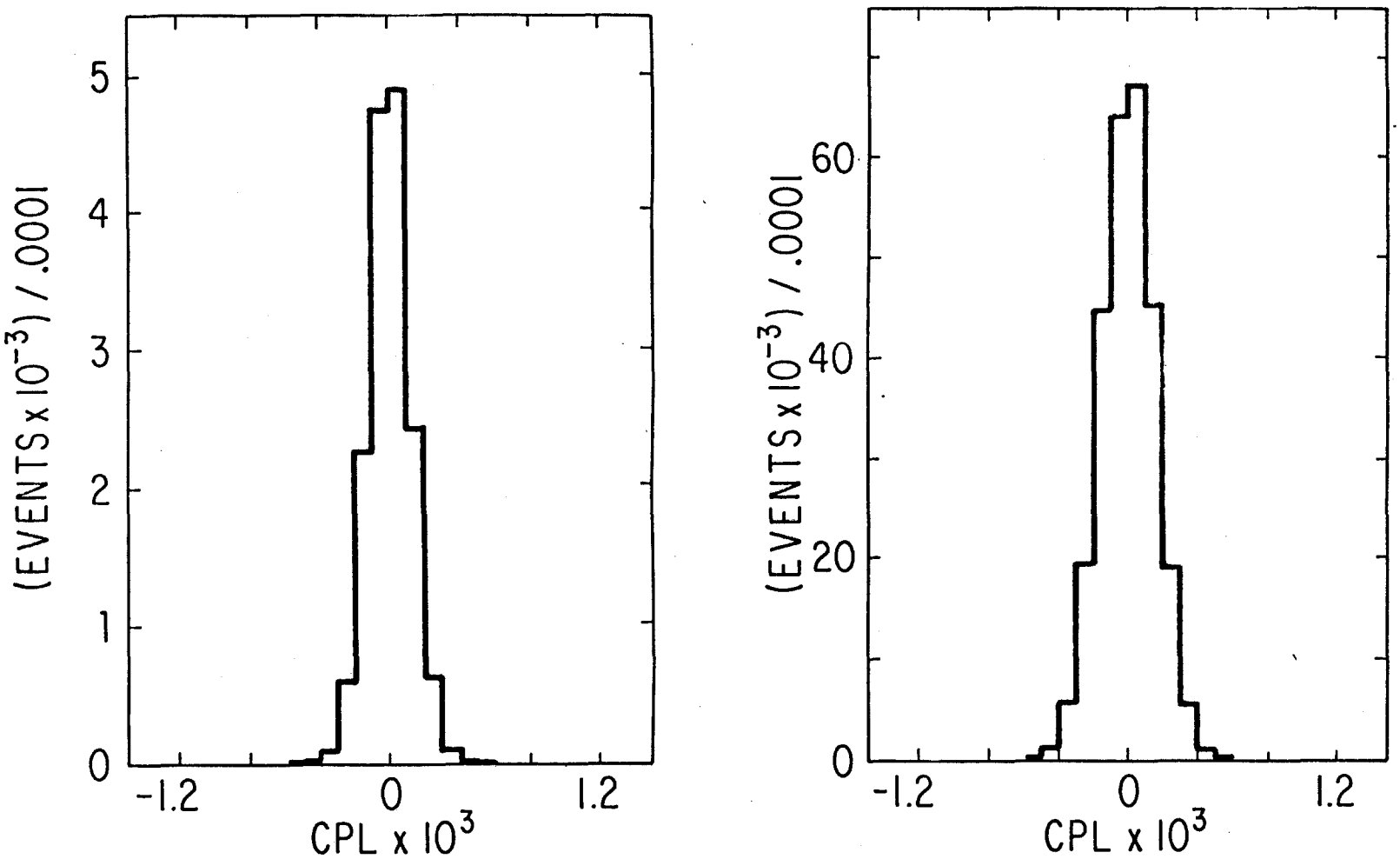

(a) (b)

Figure A10.12

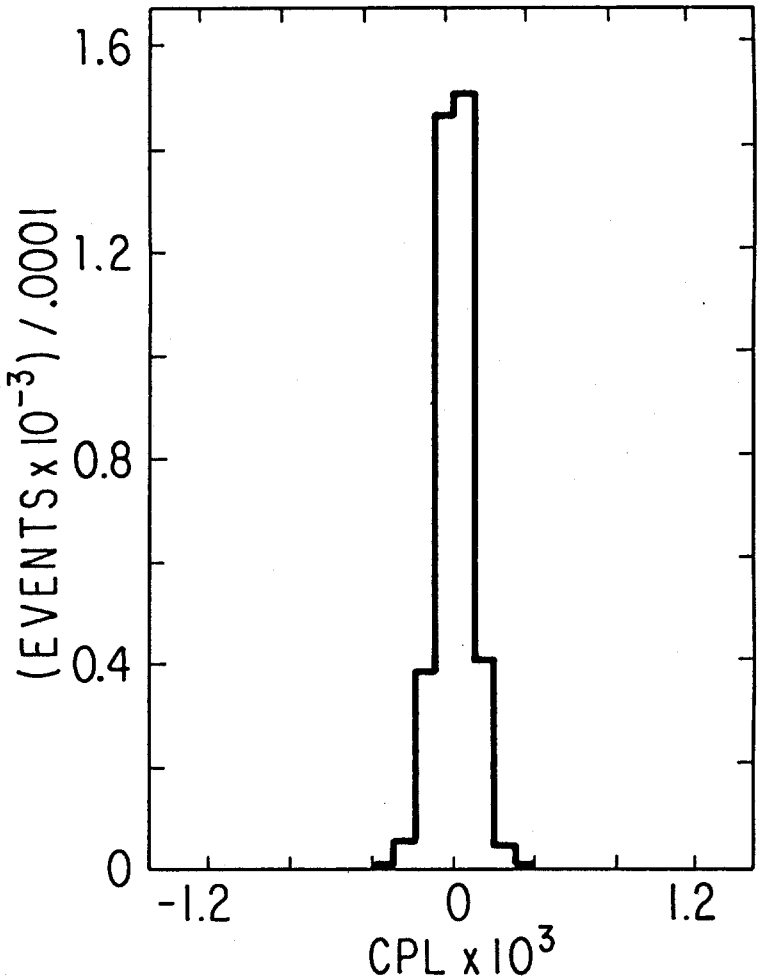

(c)

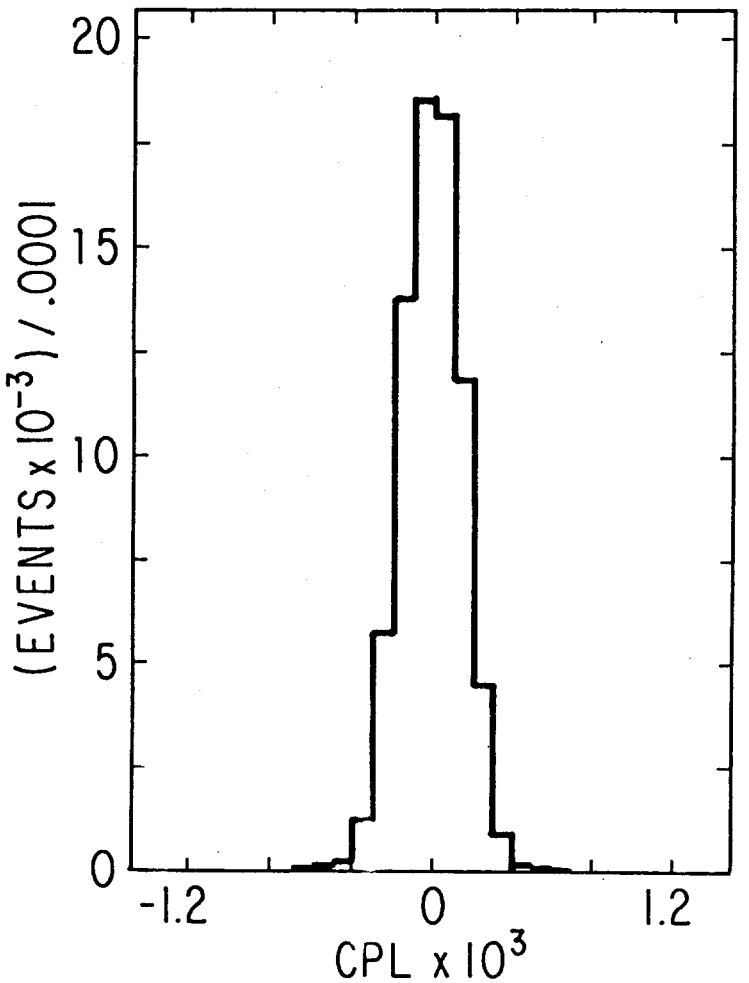

(d)

Figure A10.12 (continued)

Appendix 11

Monte Carlo

The experiment was simulated by Monte Carlo methods. Simulated data were analyzed by the same programs as the real data to determine the detection efficiency of the apparatus as a function of t (see figure A11.11 and Tables A13.2-A13.13).

The simulation of an event began with the generation of the beam vector momentum, the location and slope of the beam at the first proportional chambers (b1x and b2y) a value of t and ϕ and a target interaction point. The initial parameters for these distributions were obtained from the real data. The momentum distribution was modeled after the x distribution at the P hodoscope. Because this hodoscope was located at a momentum dispersed focus in the beamline there was a linear relation between the particle position and momentum. The initial distributions of the beam in x and y were taken from the distributions in b1x and b2y. The beam angles were determined by extrapolating the spectrometer tracks to their meeting in the hydrogen target. This point was used with the positions in b1x and b2y to calculate the beam slopes. The vertical focusing of the beam was determined from a scatter plot of the vertical slope versus position in b2y. Adjustments were made to the widths of the beam momentum, y angular divergence and x angular divergence by comparing the kinetmatic peaks forward moment

difference, coplanarity and t difference of both real and Monte Carlo data. The t distribution was an exponential whose parameter was adjusted to match the real and Monte Carlo t distribution. A small amount, about 5%, of the events were generated with a flat distribution in t to define the acceptance in the high -t regions. The z of the elastic interaction was generated randomly between the target flask ends. The ϕ distribution was randomly distributed between limits determined by preliminary runs of the Monte Carlo.

The beam particle was tracked through the apparatus to the z position of the elastic interaction point. The scattered particles were tracked through the spectrometers with aperture cuts made at the magnet walls and hodoscopes. If all these were satisfied then the position of the particle at the wire chambers was quantized to the closest wire and written to magnetic tape for subsequent analysis.

The decay of the pion and kaon was modeled in the forward arm. Decays before reaching the hydrogen target were not modeled (see Appendix 12).

The chamber efficiencies given in Table A5.2 were used in the simulation. The number of Monte Carlo events generated for each period was proportional to the number of master triggers during the period. The averages were taken over periods in which there was no gross change in the chamber performance (e.g. no broken signal wires). The state of the beam Cerenkov counter was the same

throughout each period. In addition the efficiency of the outside logic (pretrigger for the Cornell chambers) was used to deaden the Cornell chambers. In one period the efficiency of this pretrigger depended on which matrix element would cause the trigger. This was also simulated.

Multiple scattering was simulated using Moliere theory.[1] The scattering angle distributions for four thicknesses (measured in radiation lengths) were calculated. The radiation length of each scattering center was calculated using the values in the Particle Data Book.[2] This scattering angle distribution for the center was taken as the closest of the four distributions and scaled by the factor in reference 2.

The forward analysis magnets were modeled with uniform square fields. The recoil analysis magnet was simulated by several adjacent square fields. The strength of each field was specified by a one dimensional magnet map (vertical field vs. z) which was made just before the experiment. A correction for vertical focusing was made upon entering and leaving the field. This focusing effect arose from the rise of the vertical field over some length, ℓ, along the z axis. Because the magnet was much longer in the x direction than the y direction, the model assumed that there was no horizontal variation of the field. These assumptions and Maxwell's equations give $B_x = 0$, and

$$\frac{\partial B_z}{\partial y} = \frac{\partial B_y}{\partial z} \tag{1}$$

where $\vec{B}$ is the magnetic field. This can be integrated by assuming a linear dependence of B_y on z to give

$$B_z = \frac{B_{max} y}{\ell} \tag{2}$$

where B_{max} is the maximum value of the vertical field. The impulse (for a unit charge) due to the z component of the magnetic field is

$$\begin{aligned} \delta p_y &= \int_0^t V_x B_z \, dt \\ \delta p_x &= \int_0^t V_y B_z \, dt \end{aligned} \tag{3}$$

where $\vec{V}$ is the velocity of the particle. The first integral can be expressed as

$$\delta p_y = \int_0^\ell \frac{B_{max} y}{\ell} \frac{p_x}{p_z} \, dz$$

where $\vec{p}$ is the momentum of the particle. The vertical position can be approximated as

$$y = y_0 + \left(\frac{dy}{dz}\right) z \tag{4}$$

giving

$$\delta p_y = B_{max} \frac{p_x}{p_z} \left(y_0 + \frac{dy}{dz} \frac{\ell}{2} \right) \tag{5}$$

Here y_0 and dy/dz are the y position and slope at the beginning of the magnetic field.

Similarly

$$\delta p_x = -B_{max} \frac{p_y}{p_z} \left(y_0 + \frac{dy}{dz} \frac{\ell}{2} \right) \cong 0 \tag{6}$$

since $p_y \ll p_z$ for this experiment. The combined effect of entering and leaving the field is approximately[3]

$$\begin{aligned} \Delta p_y &= (\delta p_y)_{in} + (\delta p_y)_{out} \\ &= B_{max} \left(y_0 + \frac{dy}{dz} \frac{\ell}{2} \right) (p_{x_{in}} - p_{x_{out}}) \\ &= B_{max} \left(y_0 + \frac{dy}{dz} \frac{\ell}{2} \right) \text{RBDL} \end{aligned} \tag{7}$$

The residual[4] in the last y chambers is given by

$$dy = \frac{\Delta p_y}{p_z} \Delta z \tag{8}$$

where Δz is the distance from the magnet to the y chambers. This estimate of the residual is graphed in Figure A11.1 for an extreme value of y_0. In practice the value of B_{max} was set by matching the y_0/p_z^2 dependence of the residual between Monte Carlo and real data but the value used, .0034 $(\text{GeV}/c)^2/\text{cm}$, was close to RBDL/W = .0035 $(\text{GeV}/c)^2/\text{cm}$.

References

1. H. A. Bethe, Phys. Rev. 89, 1256 (1953).

2. M. Aguilar-Benitez et al., Phys. Lett. 11b, April (1982).

3. Here RBDL is the recoil analysis magnet field integral defined in Table A10.3.

4. The residual is defined as the difference between the expected position at the downstream chambers (i.e. the extrapolated position of the upstream track segment) and the y downstream cluster coordinate.

Figures A11.1 - A11.10. Comparison between Monte Carlo and real data. The real data is represented by the black squares and the Monte Carlo data by the histograms. The total number of Monte Carlo events has been normalized to the total number of real events in each figure. The variables are defined in Table A10.4.

Figure	Distribution	Beam Momentum (GeV/c)
A11.1	DXF (mm)	-200
A11.2	DXR (mm)	-200
A11.3	$[(PF-PRM)/PF] \times 10^3$	-200
A11.4	$(PR-PRM)/PR^2$ $(GeV/c)^{-1}$	-200
A11.5	YD (mm)	-200
A11.6	$TF-TR\ (a + b\|TF\|)$	-200
A11.7	$CPL \times 10^3$	-200
A11.8	$CPL \times 10^3$	+100
A11.9	$CPL \times 10^3$	-100
A11.10	$CPL \times 10^3$	+200

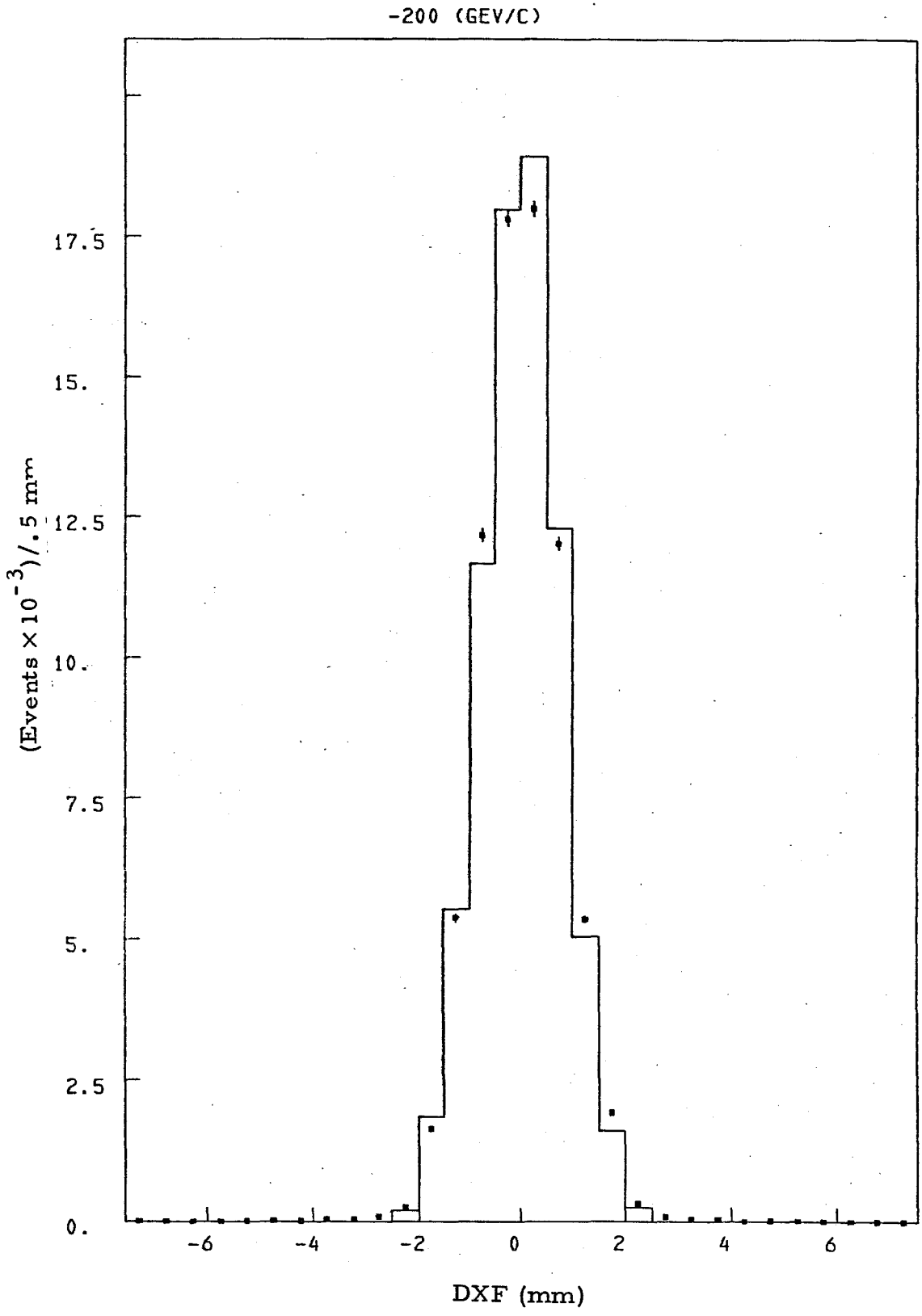

Figure A11.1

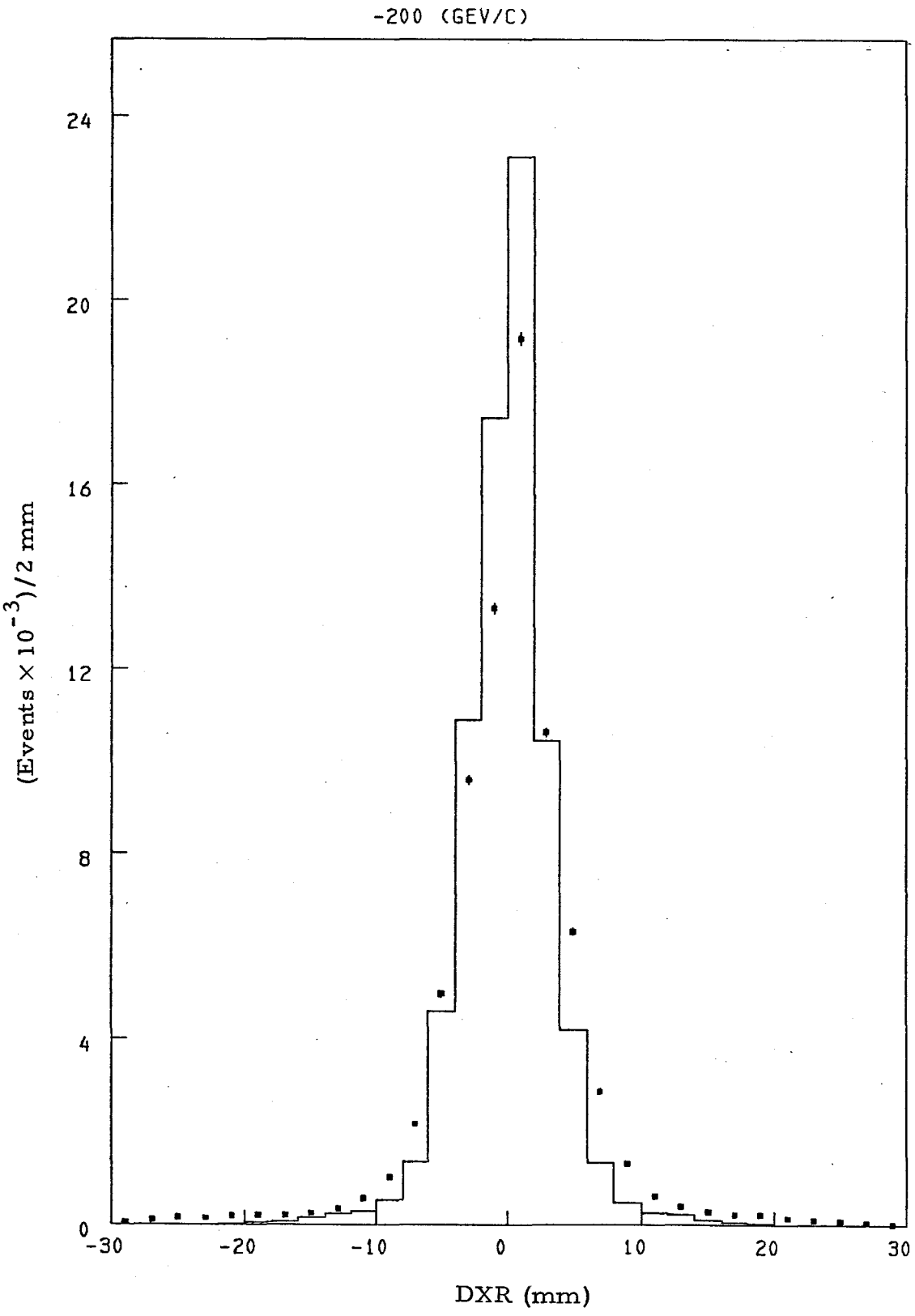

Figure A11.2

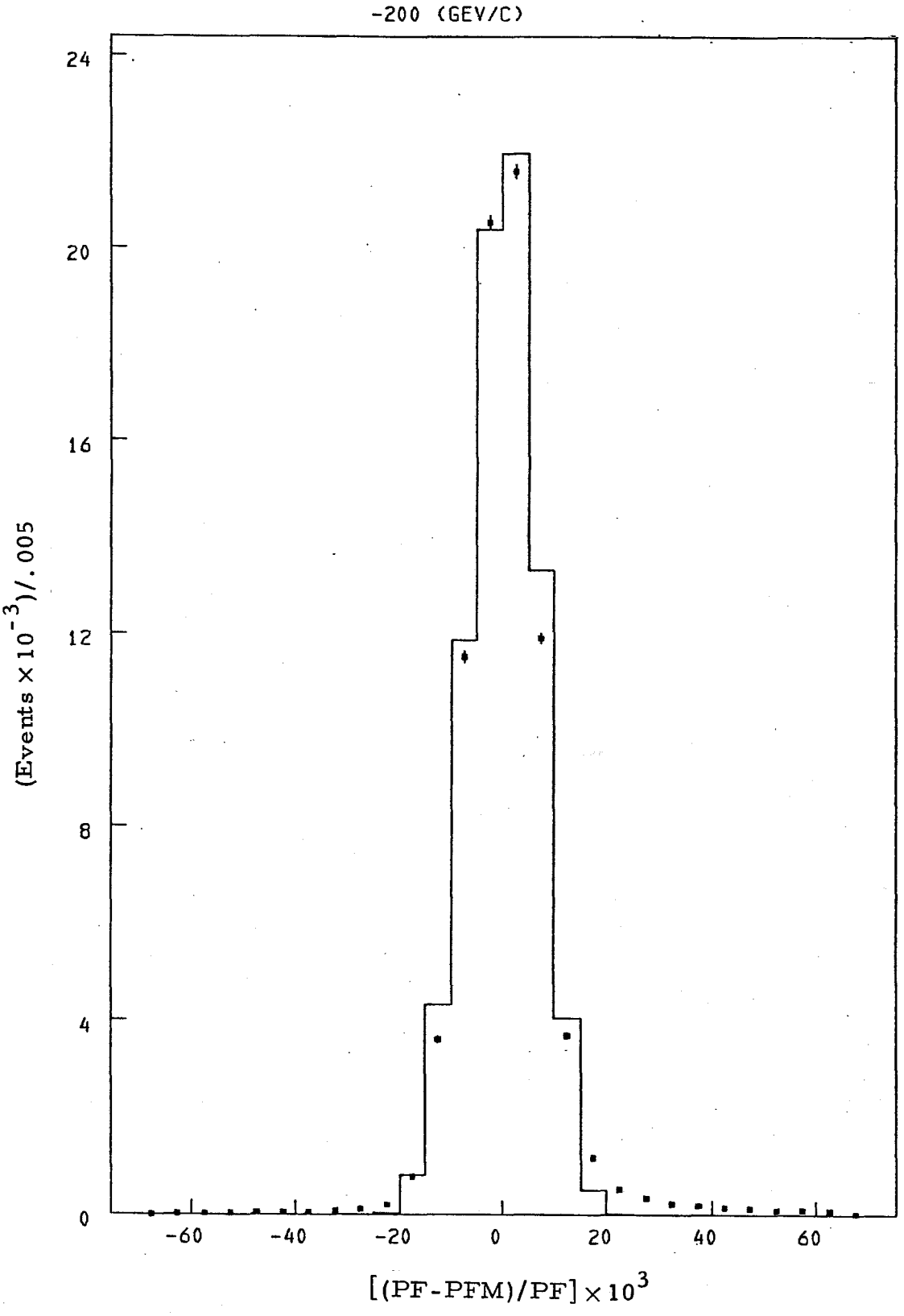
-200 (GEV/C)
24
20
16
12
8
4
0
(Events × 10^-3)/.005
-60
-40
-20
0
20
40
60
[(PF-PFM)/PF] × 10^3

Figure A11.3

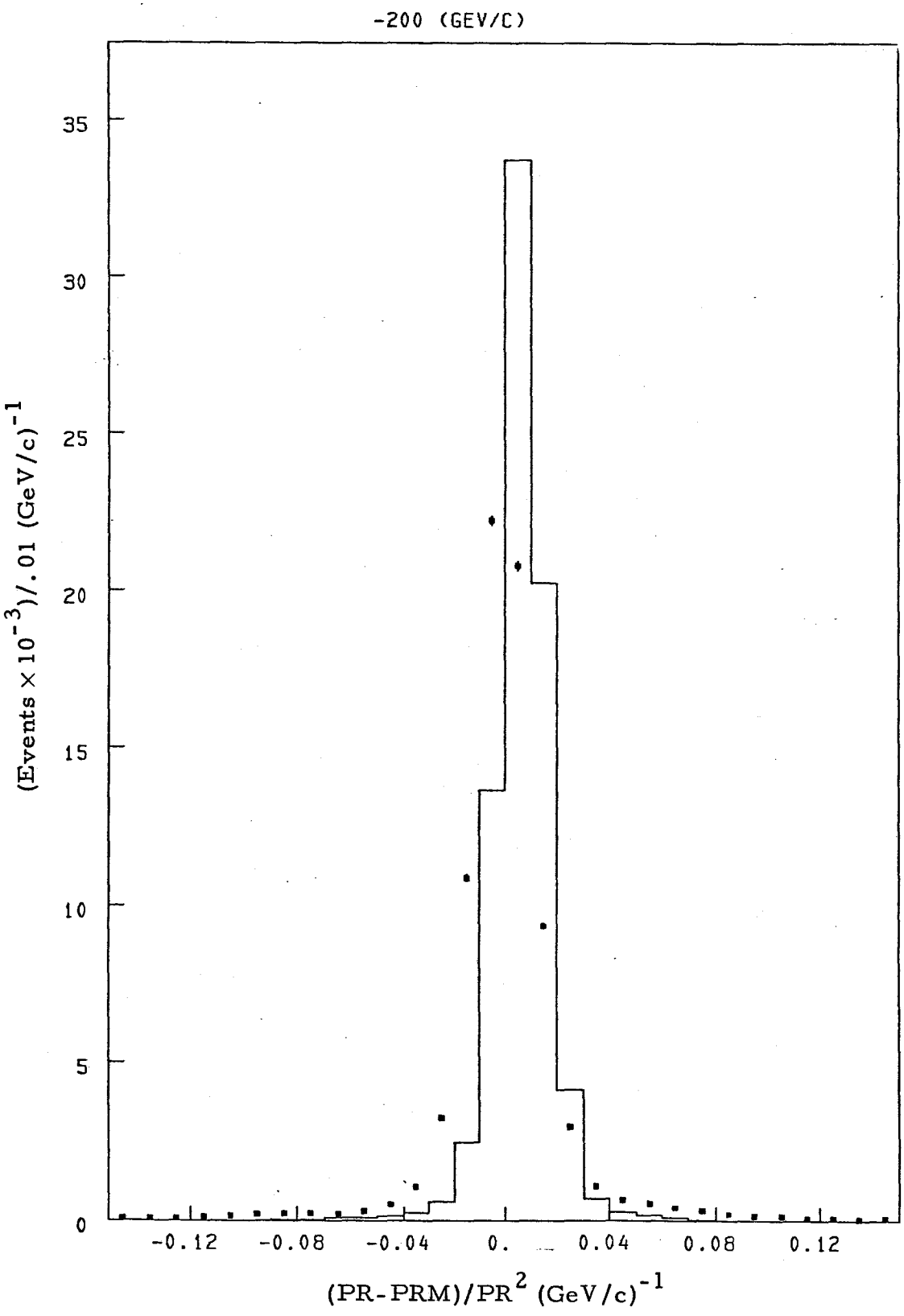
-200 (GEV/C)
35
30
25
20
15
10
5
0
(Events × 10^-3)/.01 (GeV/c)^-1
-0.12
-0.08
-0.04
0.
0.04
0.08
0.12
(PR-PRM)/PR^2 (GeV/c)^-1

Figure A11.4

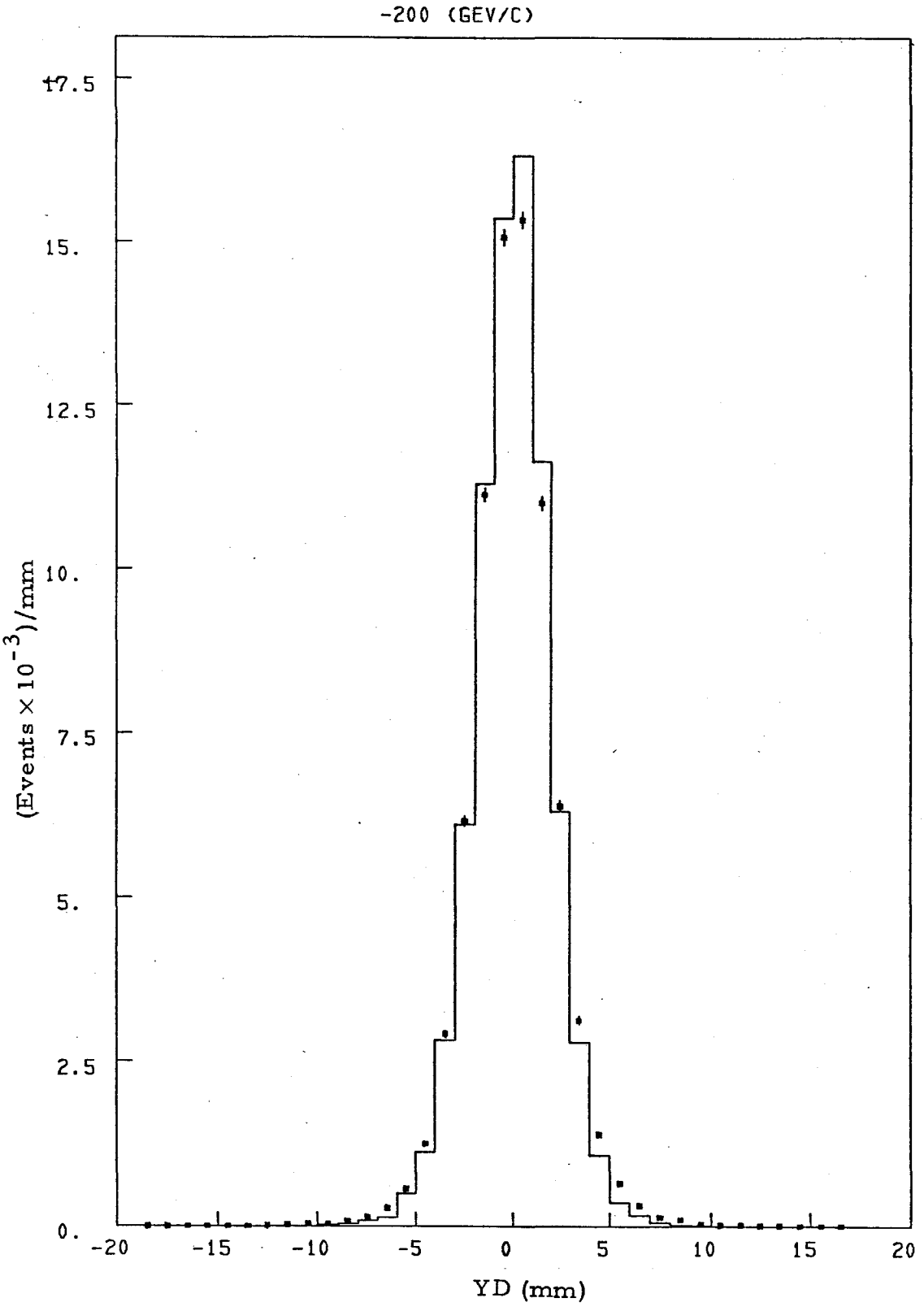
-200 (GEV/C)
17.5
15.
12.5
10.
7.5
5.
2.5
0.
(Events × 10^-3)/mm
-20
-15
-10
-5
0
5
10
15
20
YD (mm)

Figure A11.5

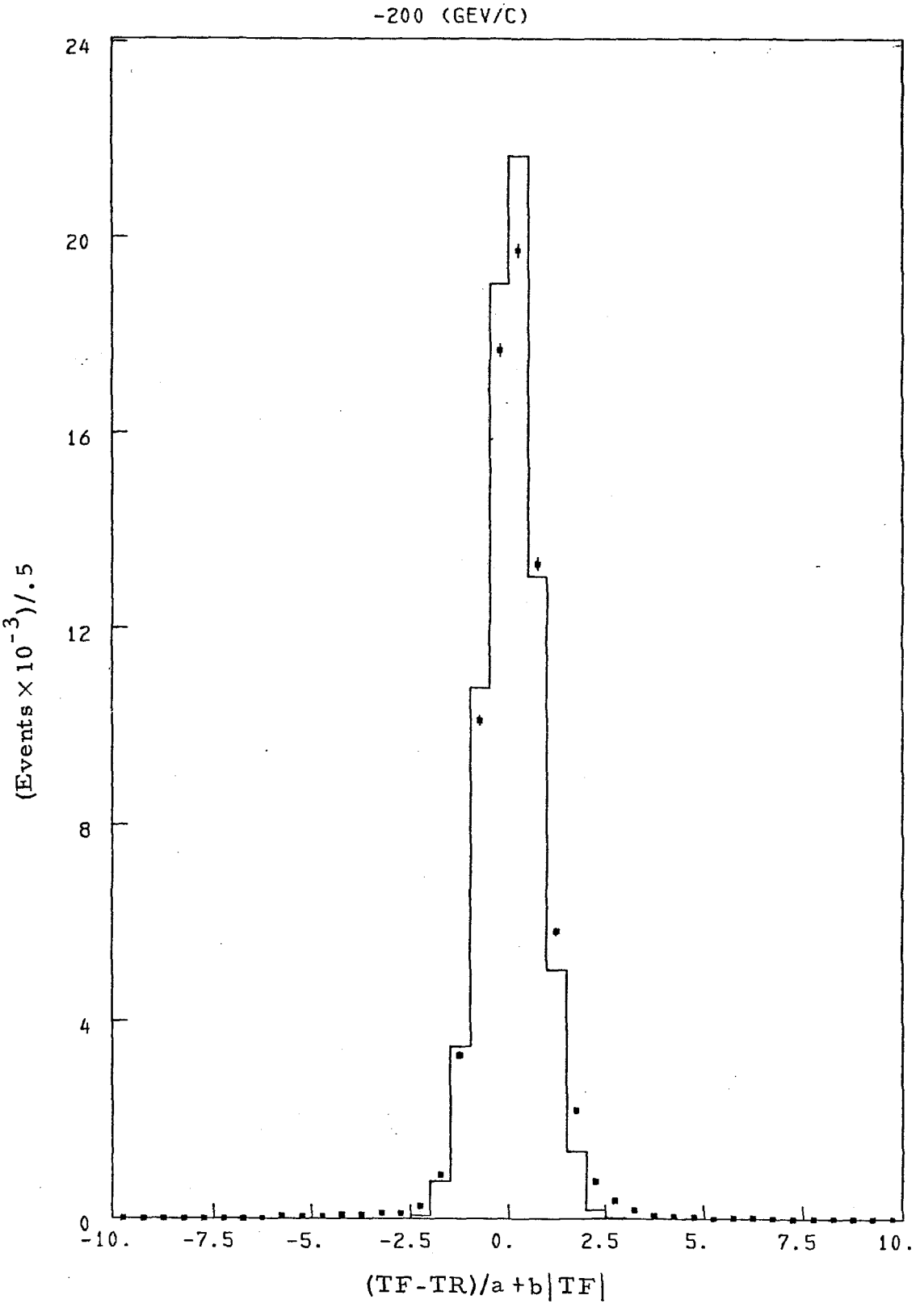
-200 (GEV/C)
24
20
16
12
8
4
0
(Events × 10^-3)/.5
-10.
-7.5
-5.
-2.5
0.
2.5
5.
7.5
10.
(TF-TR)/a +b|TF|

Figure A11.6

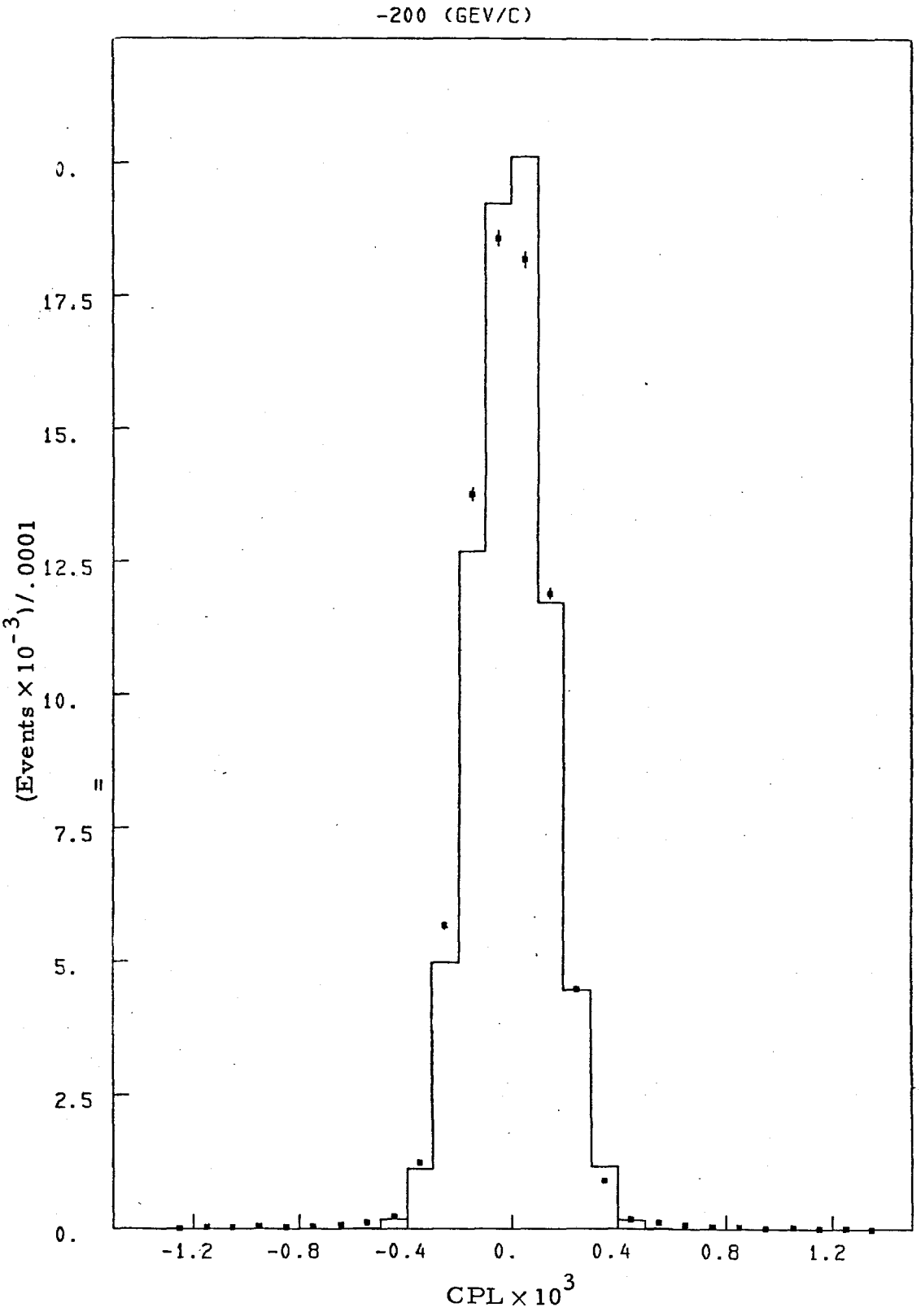
-200 (GEV/C)
0.
17.5
15.
12.5
10.
7.5
5.
2.5
0.
(Events × 10^-3)/.0001
-1.2
-0.8
-0.4
0.
0.4
0.8
1.2
CPL × 10^3

Figure A11.7

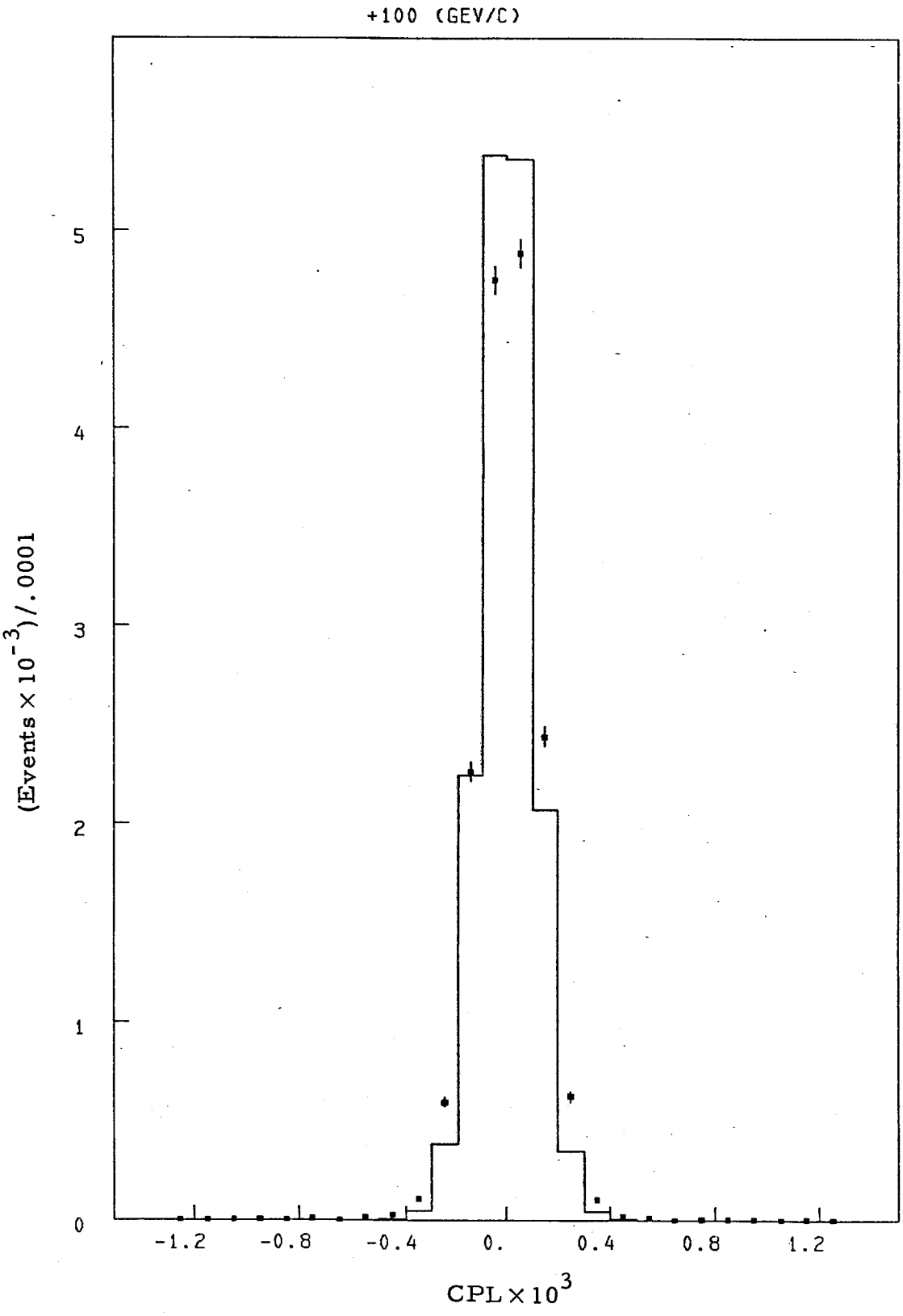

Figure A11.8

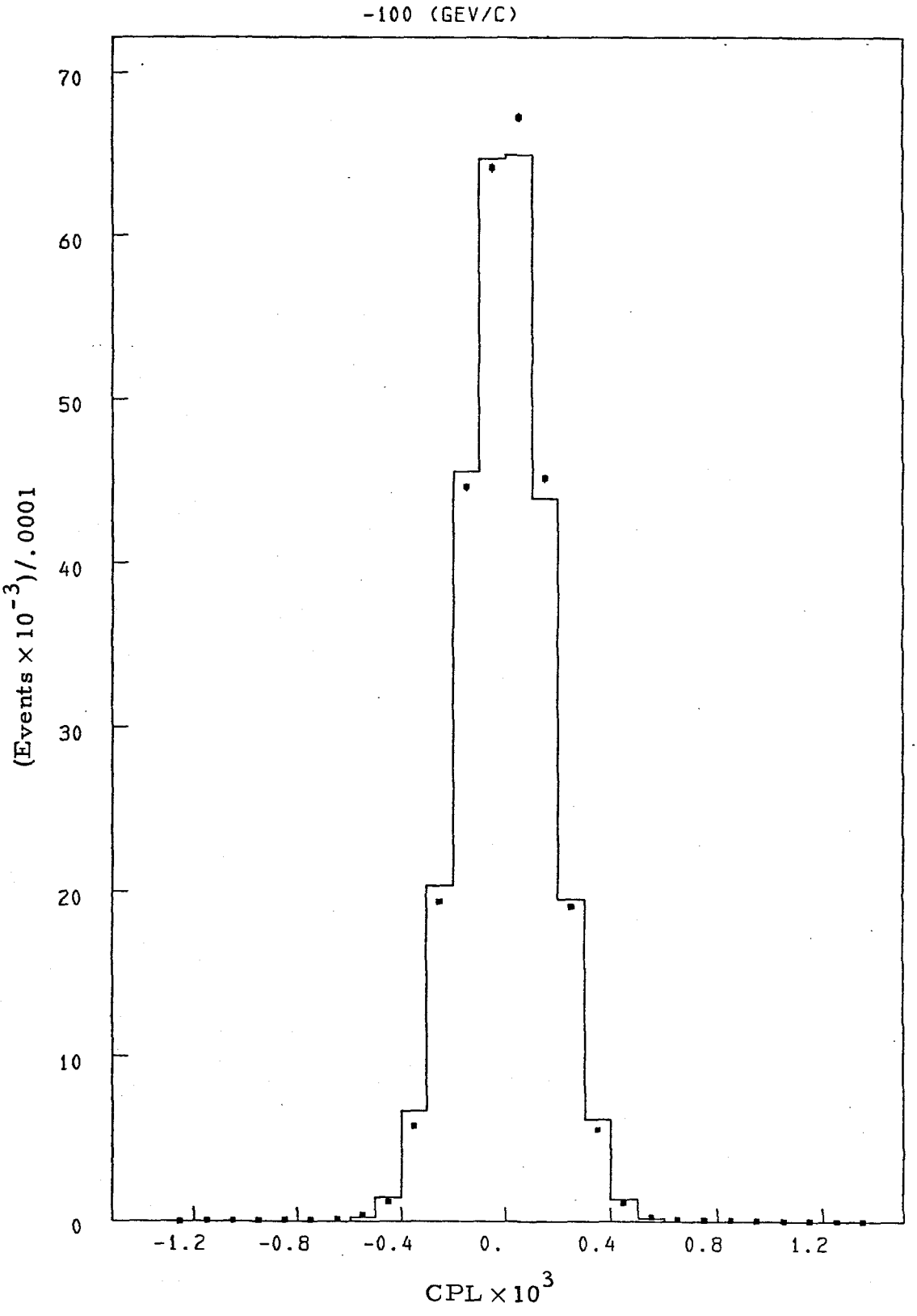
-100 (GEV/C)
70
60
50
40
30
20
10
0
(Events × 10^-3)/.0001
-1.2
-0.8
-0.4
0.
0.4
0.8
1.2
CPL × 10^3

Figure A11.9

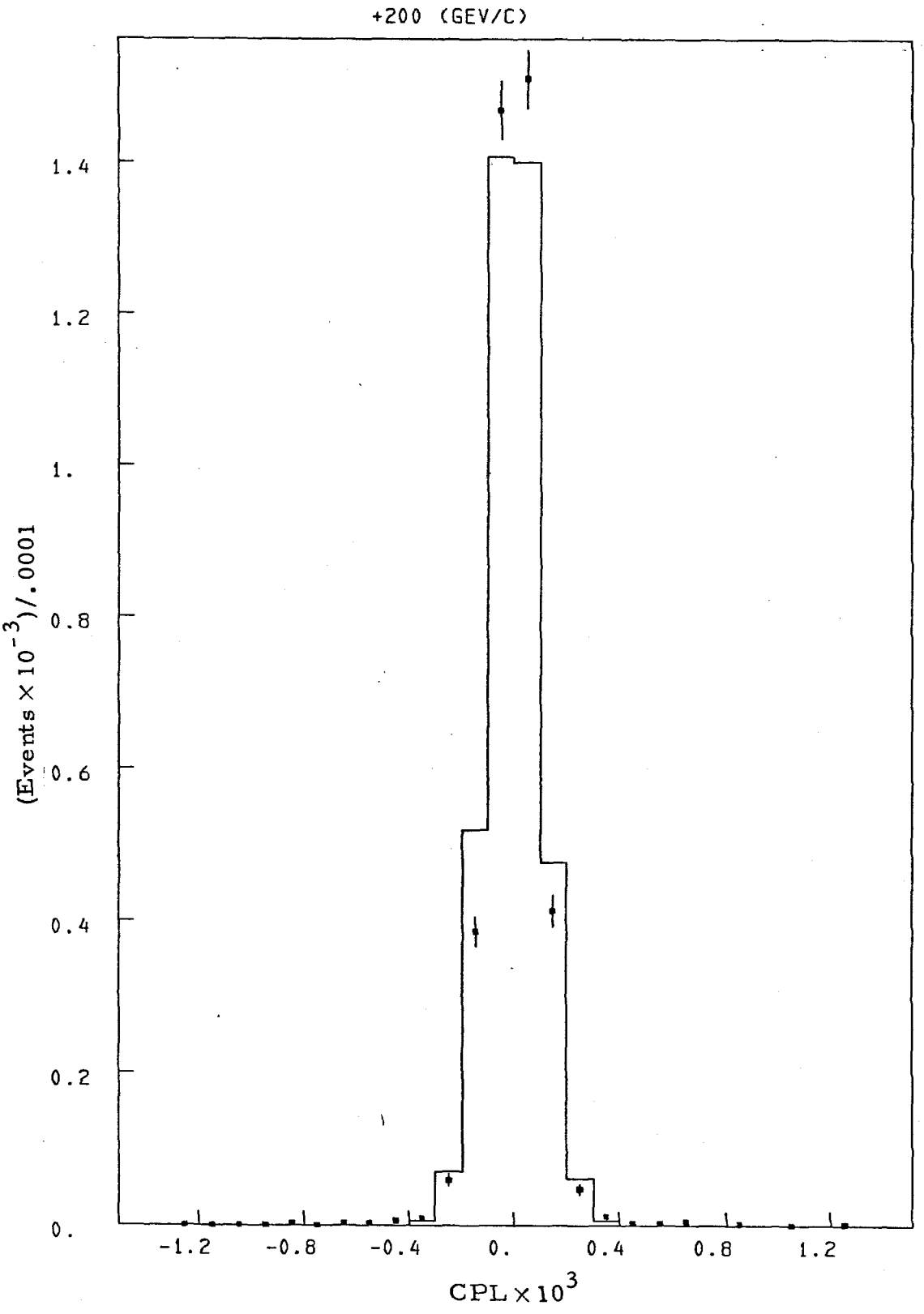

Figure A11.10

Figure A11.11. Geometrical acceptance. The geometrical acceptance is shown as a function of t. The effects of cuts and chamber efficiencies are not included in the calculation of the geometrical acceptance. The acceptance is shown for 100 and 200 GeV/c beams.

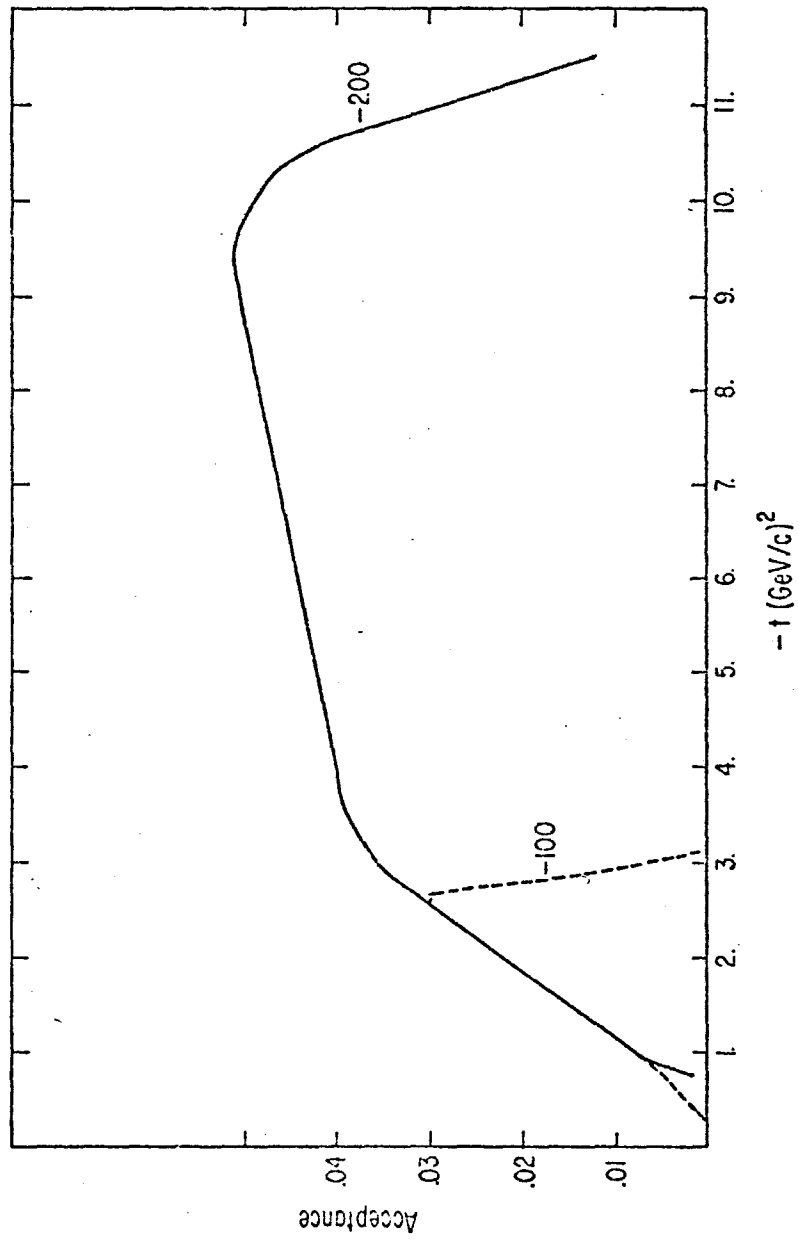
Acceptance
.04
.03
.02
.01
-100
-200
1.
2.
3.
4.
5.
6.
7.
8.
9.
10.
11.
$-t\ (GeV/c)^2$

Figure A11.12. The effect of vertical focusing on the residual in the downstream Y proportional chambers. The residual is the difference between the expected position (the extrapolated position of the upstream Y track segment) and the Y downstream cluster coordinate. The magnitude of the effect depends on the Y position of the recoil proton at the analysis magnet. The residual is calculated for this position equal to 8 cm which is an extreme value for this experiment.

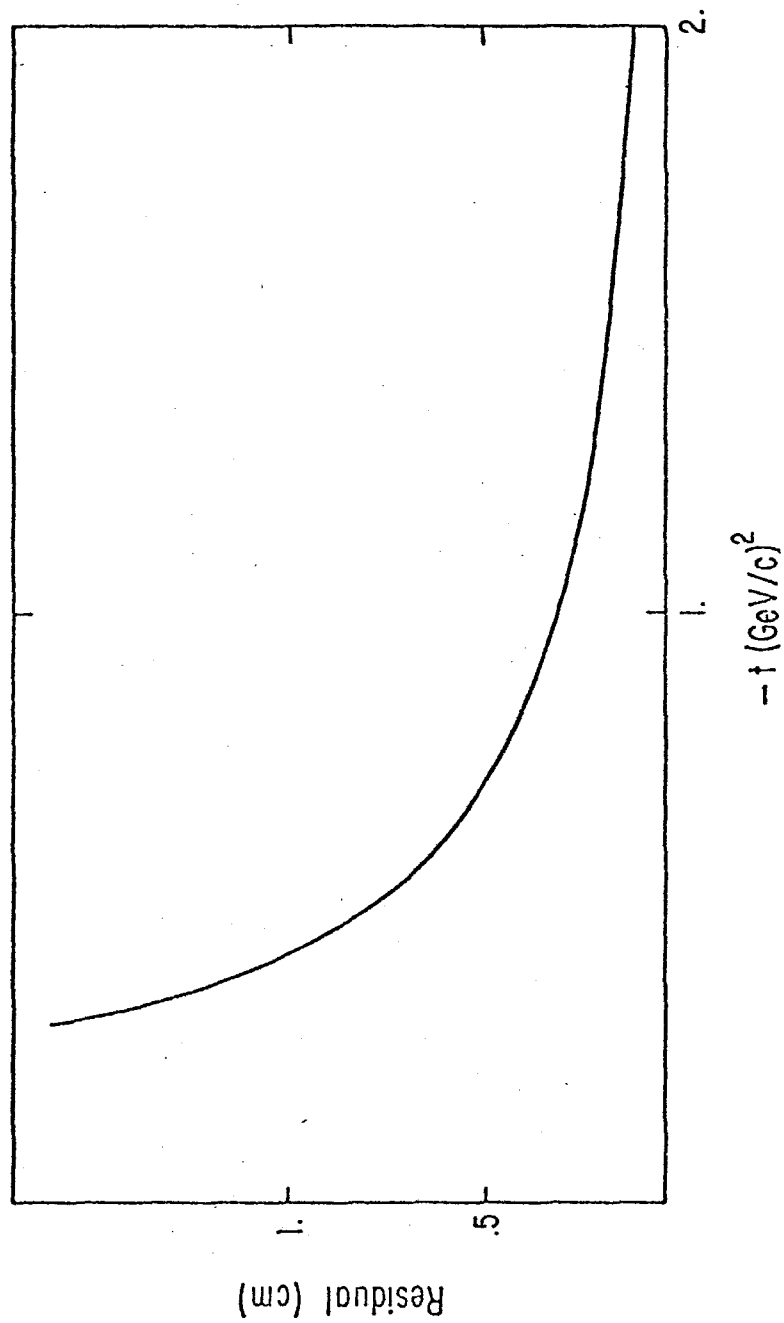
Residual (cm)
1.
.5
1.
2.
$-t$ (GeV/c)^2

Appendix 12

Particle Separation

The events were separated by incident beam particle using the Cerenkov counter data. A latch from CB signaled the presence of a pion, kaon or proton in the accelerator bunch which caused the elastic event. More than one particle could be present in the same bunch, however, so that it could not be assumed that all the CB tagged events resulted from the tagged beam particle. The forward threshold counter (CF) was sensitive to the scattered hadron. Because the probability of scattering into the acceptance was small, the probability of two particles going through CF within its 55 ns time resolution was negligible. The signal from CF was analyzed with an analog to digital converter (ADC).

The CF counter was calibrated with elastic events which were tagged by CB. The sample required both the P and X hodoscope to show at most one beam particle. This requirement removed approximately 90% of the double bunch events and the remaining contamination was estimated by comparing the sample to a similar sample in which no hodoscope requirement was made. From this information appropriate limits were chosen on the pulse height and the fraction of each type of particle within each region was calculated (Table A12.1). The separation by CF (from the pulse height recorded at each trigger)

was not complete. At 200 GeV/c there was no useful separation between pions and kaons. In addition, the antiprotons made up such a small portion of the beam that their CF signal was buried beneath the tail of the signal of the other particles. Hence a signal from CB was required to identify 200 GeV K^+ and K^- and antiprotons at 100 and 200 GeV/c.

The probability of CB misidentifying an elastic event due to multiparticle bunches was estimated from the relative cross sections (on a first pass the data) and the beam fractions of the particles. The fraction of double bunches was estimated from the response of the P and X hodoscopes during type 2 triggers which required only a coincidence of the beam scintillation counters. The small number of bunches with three or more particles were treated as double particle bunches. The appropriate combination of requirements of the CB latch and CF pulse height was made and the resulting efficiencies and contaminations tabulated (Table A12.3).

Events in which CB latched a different particle than expected from the CF region were not included in any sample. At 100 GeV/c CF was calibrated only for the 1980 data and during 1981 the counter was run with higher pressure. The ADC boundary was rescaled but the resulting relative error in the kaon sample was unacceptable so only 1980 data was used in this sample.

Table A12.1

CF calibration[1]

Beam Momentum (GeV/c)	Region	Definition	Fraction π	Fraction K	Fraction p
-200	I	ADC $\leq$ 40	.0	.008+.005	.968+.003
	II	ADC > 40	1.0	.992+.005	.032+.003
+200	II	ADC $\leq$ 40	.0	.003+.003	.984+.003
		ADC > 40	1.0	.997+.003	.016+.003
-100	I	ADC $\leq$ 40	.0	.012+.006	.937+.001
	II	40 < ADC $\leq$ 238	.009+.004	.785+.016	.063+.004
	III	ADC > 238	.0	.193+.011	.0
+100	I	ADC $\leq$ 40	.0	.024+.006	.997+.002
	II	40 < ADC $\leq$ 238	.009+.002	.794+.016	.063+.004
	III	ADC > 238	.991+.002	.191+.011	.0

[1] During the 1981 data the +-100 GeV/c CF ADC boundaries were scaled up 88 ADC channels.

Table A12.2

CB calibration

Beam Momentum (GeV/c)	Sample	Fraction	Fraction of particles contained in sample		
			π	K	p
-200	K^-	.243	.012+.002	.976+.002	.012+.002
-200	$\bar{p}$	.243	.0016+.0003	.0016+.0003	.9968+.0004
+200	K^+	.233	.0082+.002	.9835+.002	.0082+.002
-100	$\bar{p}$	.253	.0082+.002	.0082+.002	.9835+.003

Table A12.3

Particle contamination correction matrix (P_{ij})

Beam Momentum (GeV/c)	Sample	Expected fraction of elastically scattered particles contained in sample			Required Counters
		π	K	p	
-200	π^-	1.	.992±.005	.032±.003	CF(III)
	K^-	.0010±.0003	.992±.005	.00032±.00002	CF(II), CB
	$\bar{p}$	.0	.00001	.965±.003	CF(I), CB
+200	π^+	1.	.997±.003	.016±.003	CF(II)
	K^+	.0064±.002	.997±.003	.00010±.00003	CF(II), CB
	$\bar{p}$	.0	.003±.003	.984±.003	CF(II)
-100	π^-	.991±.004	.193±.011	.0	CF(III)
	K^-	.009±.004	.794±.016	.063±.004	CF(II)
	$\bar{p}$	.0	.0	.937±.004	CF(I), CB
+100	π^+	.991±.004	.191±.013	.0	CF(III)
	K^+	.009±.004	.785±.014	.003±.001	CF(II)
	p	.0	.024±.006	.997±.002	CF(I)

Appendix 13

Cross Section Calculation

The differential cross sections are presented in bins corresponding to a range of t. The limits on the bins were chosen to straddle spikes in the t distribution due to the finite wire spacing of the proportional wire chambers. The average differential cross section for a bin centered at value t_i is defined as:

$$\frac{d\sigma}{dt}(t_i) = \frac{N(t_i)}{\Delta t_i \, \epsilon(t_i) \, PT \, C_1 \, \Phi} \qquad (1)$$

where

Δt_i = the width of the bin

PT = the number of protons contained in the hydrogen target, 4.28×10^{24} cm^{-2}

$\epsilon(t_i)$ = the detection efficiency of the apparatus as determined by the Monte Carlo program

Φ = the measured hadron flux through the hydrogen target

C_1 = a correction factor which is independent of t

$N(t_i)$ = the number of events in bin centered on bin t_i corrected for background, measurement resolution and efficiency of particle separation.

$$N(t_i) = \sum_m N(t_m)\, C_2(t_m)\, C_3(t_m, t_i)\, C_4(t_i)$$

where

$N(t_m)$ = the number of events in bins centered on the measured t value, t_m

$C_2(t_m)$ = the background correction

$C_3(t_m, t_i)$ = the measurement resolution correction (defined below)

$C_4(t_i)$ = the correction for particle separation.

The raw flux was calculated from the 1980 and 1981 integrated beam signals.[2] The result for each period was weighted by the beam fractions (Table A2.1) to obtain the flux of each particle type.

The t independent corrections are summarized in Table A13.1. The first correction to the raw flux was the "double bunch" correction. Sometimes CB would tag a particle which was the second particle in the accelerator bunch. These events were not included in the samples of Table A12.3 if only CF was required and the particle tagged by CB was different than the sample indicated by CF. This correction compensated the loss in flux due to this event.

A correction was made for the decay of the beam hadron between CB and the hydrogen target. Only a negligible number of decays which occurred upstream of CB resulted in a particle being counted by the beam counters. Decay of the hadron in the spectrometers was modeled in the Monte Carlo. The absorption of the

hadron in the hydrogen target was calculated using measured total cross sections[1] and the hydrogen target length. Absorption due to material in the spectrometers and beamline (after B2) was calculated using these total cross sections. An additional correction was made for the estimated number of delta rays (knock-on electrons) which penetrated the aluminum target block and were detected by the target veto counters.

A rate correction was necessary because the yield of elastic events per gated beam was a decreasing function of intensity. The correction was made by assigning each spill a bin on the basis of the spill's intensity as measured by the N counter. The total number of gated beam counts and elastic events were accumulated for each bin and the ratio of these plotted. The rates were extrapolated to zero intensity. The correction was the average (over all intensities) rate divided by the rate at zero intensity. These extrapolations were done for the 1980 and 1981 pion samples and the final correction was the weighted (by gated beam signals) average of the two periods. Figure A13.1 shows an example of this extrapolation. The extrapolations were made by fitting a straight line through the data. The systematic error of the correction was taken as the statistical error of the least squares fit.

Corrections which depended on t were made to the raw number of events and are summarized in Table A13.2. The first of these

was a background correction and was made by looking at the coplanarity signal of each particle. Essentially no Monte Carlo event had coplanarity with absolute value greater than .0006 so that the background was estimated from the number of events with absolute value of coplanarity between .0006 and .00012. The number of background events under the signal peak was calculated by assuming that the background distribution was flat.

Next the events were redistributed to reflect the finite measurement resolution of the experiment. The resolution can be calculated by differentiating equation (A9.16) with respect to the recoil scattering angle. The measurement error of this angle can be estimated from the wire spacing and distance between the two upstream recoil x chambers ($\delta\theta_4 = 1.4$ mr). The result as a function of t is shown in figure A13.2. The analysis of the Monte Carlo data yielded the number of simulated events which were reconstructed with measured value t_m as a function of the number of trial events generated with value t_g. The relation of the simulated events as binned by the simulated and measured t values can be expressed in terms of a matrix M,

$$N_{rs}(t_m) = \sum_g M(t_m, t_g)\, N_s(t_g) \tag{2}$$

Here $N_{rs}(t_m)$ is the number of reconstructed events with measured

value of t within the mth bin. $N_s(t_g)$ is the number of trial simulated events that were generated with a t value in the gth bin. The real data can be binned in terms of the measured t value, $N(t_m)$ and the corrected distribution of events expressed

$$N(t_i) = \sum_m M^{-1}(t_m, t_i)\, N(t_m) \tag{3}$$

Not all simulated events were reconstructable and some did not pass the event selection criteria. The efficiency of the detection as determined by the analysis of the simulated data is

$$\epsilon(t_g) = \frac{N_{rs}(t_g)}{N_s(t_g)} \tag{4}$$

where $N_{rs}(t_g)$ is the number of simulated events that were found with any measured value of t but were generated with t value in bin g. To use the correction equation (3) with equation (1) the effects of the efficiency and measurement error can be factored. Equation (2) can be written

$$\begin{aligned} N_s(t_m) &= \sum_g \frac{M(t_m, t_g)}{\epsilon(t_g)}\, N_{rs}(t_g) \\ &\equiv \sum_g m(t_m, t_g)\, N_{rs}(t_g) \end{aligned} \tag{5}$$

so that

$$M^{-1}(t_m, t_g) = [\epsilon(t_g)\, m(t_m, t_g)]^{-1}$$
$$= \frac{m^{-1}(t_m, t_g)}{\epsilon(t_g)} \tag{6}$$

and equation (3) becomes

$$N(t_i) = \frac{1}{\epsilon(t_i)}\, m^{-1}(t_m, t_i)\, N(t_m) \tag{7}$$

giving

$$C_3(t_m, t_i) = m^{-1}(t_m, t_i) \tag{8}$$

Finally corrections were made for the efficiency of particle separation (i.e. how many events are lost by the particle separation criteria, the factor C4b in Tables A13.2-A13.13) and the contamination by other particles in the sample (C4a in Tables A13.2-A13.13). The worst case of contamination were the +200 and -200 pion samples which contained kaons. Because the statistical quality of the kaon data was much worse than that of the pion data, an exponential fit was done to the kaon cross section before subtracting it from the pion cross section.

These corrections were done by an iterative process. If $N_j(t_i)$ is the true number of events of particle type i then, by definition of the correction matrix P_{ij} (Table A12.3), the number of events in each sample is

$$N_j'(t_i) = N_j(t_i)\, P_{jj} + \sum_{k \neq j} N_k(t_i)\, P_{jk} \tag{9}$$

This can be solved for $N_j(t_i)$

$$N_j(t_i) = \frac{N_j'(t_i)}{P_{jj}} \left[\frac{1}{1 + \sum_{k \neq j} \left(\frac{N_k(t_i)\, P_{jk}}{N_j(t_i)\, P_{jj}} \right)} \right] \tag{10}$$

The procedure involved making successive approximations for $N_j(t_i)$ and $N_k(t_i)$ in the right hand side of equation (10). These were calculated using the cross sections from the previous step.

$$N_k(t_i) \propto \frac{d\sigma}{dt}(t_i)\, \epsilon_k(t_i)\, \Delta t_i\, \Phi_k \tag{11}$$

Note that constant factors such as Δt_i cancel out in the correction. In particular the value of Φ_k was taken as the beam fraction so that corrections between samples normalized to gated beam and normalized to CB could be made.

References

1. A. S. Caroll et al., Phys. Lett., 61b (1976) 303.

2. Gated beam in the number of $B_1 \cdot B_2 \cdot \bar{A}_1$ coincidences when the experiment was enabled (see Appendix 8).

Figure A13.1. Rate correction extrapolation. The rate extrapolation is shown for the 1981 100 GeV/c data. Here I is the extrapolated value of elastic events for gated beam. A is the total number of elastic events divided by the total gated beam. The correction is I/A.

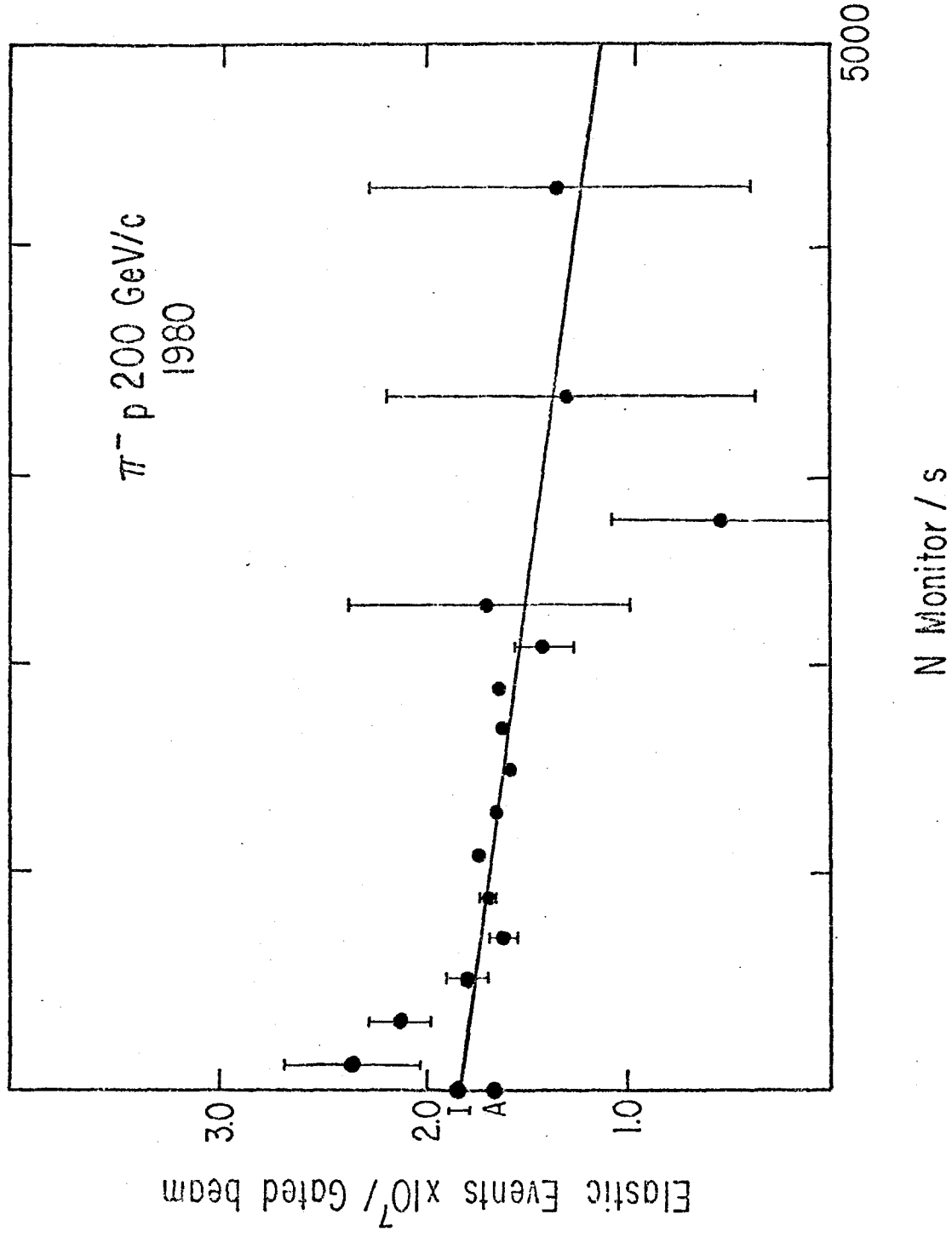

Figure A13.1(a)

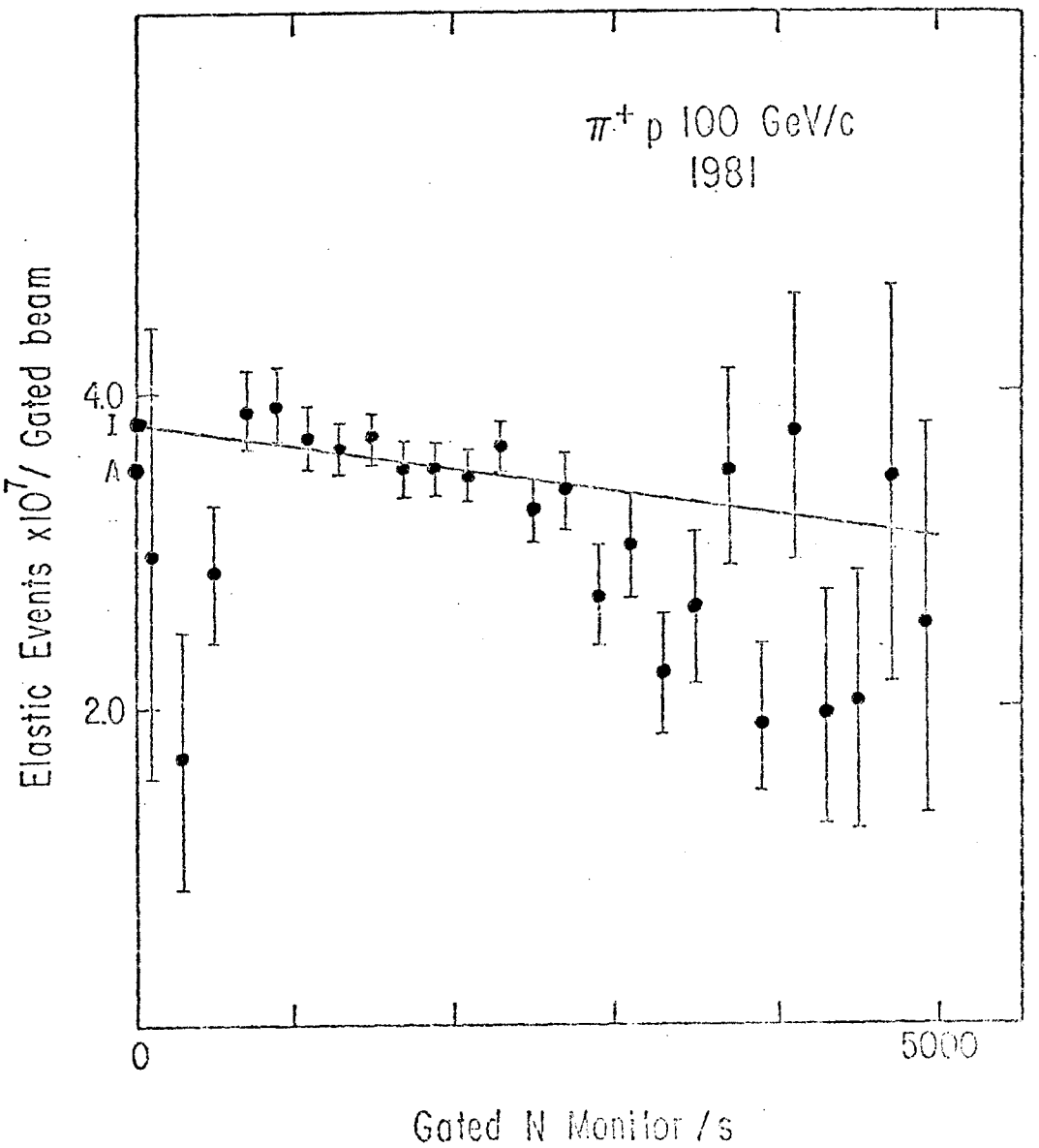

Figure A13.1(b)

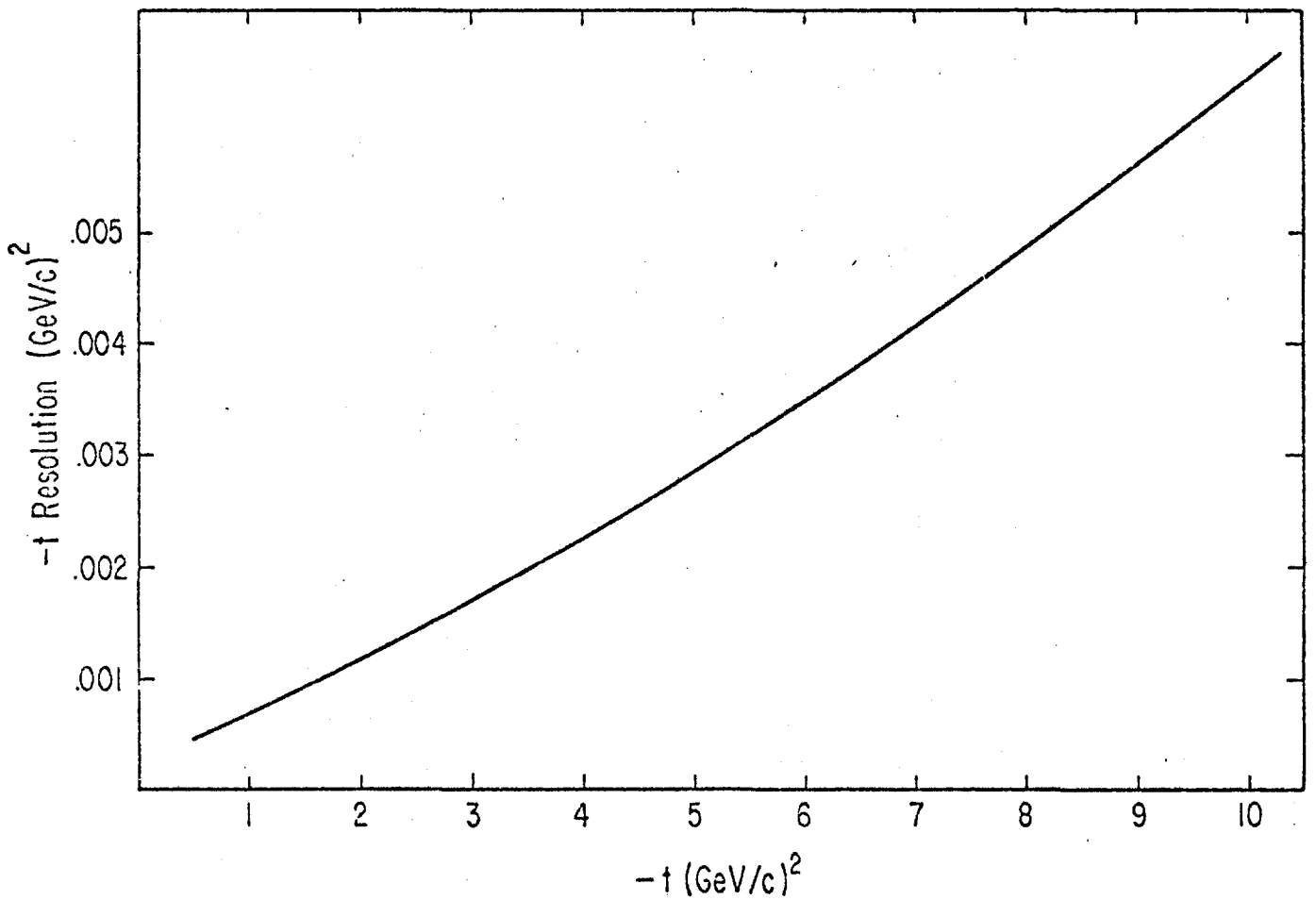

Figure A13.2. Measurement resolution of -t as a function of -t .

Table A13.1. Corrections to incident hadron flux.

Beam Momentum (GeV/c)	-100			+100		
	π^-	K^-	$\bar{p}$	π^+	K^+	p
raw flux	4.714×10^{11}	8.410×10^{9}	1.099×10^{10}	2.697×10^{10}	1.505×10^{9}	1.944×10^{10}
double bunch correction	.9936	1.	.9975	.9666	1.	1.
decay after CB	.9928	.9478	1.	.9929	.9478	1.
absorption of hadron in target	.9024	.9162	.8350	.9050	.9224	.8482
absorption of hadron in spectrometer	.9539	.9605	.9205	.9551	.9271	
absorption of recoil proton in target	.9960	.9960	.9960	.9960	.9960	.9960
absorption of recoil proton in spectrometer	.9884	.9884	.9884	.9884	.9884	.9884
δ-rays setting target veto counters	.98	.98	.98	.98	.98	.98
correction to this point	.819 ±.015	.805 ±.015	.740 ±.020	.800 ±.015	.813 ±.015	.759 ±.020
rate correction	.793 ±.038	.793 ±.038	.793 ±.038	.766 ±.054	.766 ±.054	.766 ±.054
C1-total corrections	.649 ±.032	.638 ±.032	.586 ±.031	.613 ±.044	.623 ±.044	.581 ±.043
corrected flux	3.061×10^{11}	5.365×10^{9}	6.446×10^{9}	1.654×10^{10}	9.373×10^{8}	1.130×10^{10}
relative error (%)	5.	5.	6.	7.	7.	8.

Table A13.1. (continued)

Beam Momentum (GeV/c)	-200			+200		
	π^-	K^-	$\bar{p}$	π^+	K^+	p
raw flux	4.675×10^{11}	4.853×10^{8}	1.600×10^{9}	2.536×10^{10}	8.316×10^{9}	1.542×10^{11}
double bunch correction	.9996	1.	.9980	.9731	1.	.9987
decay after CB	.9964	.9763	1.	.9964	.9736	1.
absorption of hadron in target	.9011	.9150	.8375	.9030	.9184	.8464
absorption of hadron in spectrometer	.9583	.9599	.9217	.9542	.9616	.9262
absorption of recoil proton in target	.9960	.9960	.9960	.9960	.9960	.9960
absorption of recoil proton in spectrometer	.9884	.9884	.9884	.9884	.9884	.9884
δ-rays setting target veto counters	.98	.98	.98	.98	.98	.98
correction to this point	.825 ±.015	.827 ±.015	.743 ±.020	.806 ±.015	.830 ±.015	.753 ±.020
rate correction	.950 ±.171	.848 ±.057	1.016 ±.278	.750 ±.090	.750 ±.090	.750 ±.090
C1-total corrections	.784 ±.142	.702 ±.049	.755 ±.208	.604 ±.075	.622 ±.075	.566 ±.070
corrected flux	3.663×10^{11}	3.406×10^{8}	1.211×10^{9}	1.533×10^{10}	5.170×10^{9}	8.733×10^{10}
relative error (%)	18.	7.	27.	12.	12.	12.

Tables A13.2 - A13.13. Acceptance and corrections.

t - The bin center in $(GeV/c)^2$

Δt - The bin width

ϵ - The acceptance (detector efficiency)

$\delta\epsilon$ - The statistical error of the detector efficiency

N' - The number of events in the bin after separation of events by beam particles

C_2 - Background correction

C_3 - Measurement resolution correction

C_{4A} - Correction for contamination by other particles

C_{4B} - Correction for events excluded to maintain a pure event sample

σ - Differential cross section

$\delta\sigma$ - Error in differential cross section

Table A13.2. 100 GeV/c $\bar{p}p$ acceptance and corrections

t	Δt	ϵ	$\delta\epsilon$	N'	C_2	C_3	C_{4A}	C_{4B}	$\sigma_{\bar{p}}$	$\delta\sigma_{\bar{p}}$
.349	.098	.000152	.000006	192	.996	1.627	1.000	1.067	807.76497	55.20804
.414	.031	.000586	.000019	321	1.000	1.018	1.000	1.067	696.41648	43.45083
.447	.035	.001114	.000029	453	1.000	1.056	1.000	1.067	474.54281	24.38168
.483	.037	.001542	.000040	569	.994	1.051	1.000	1.067	403.16660	19.08239
.521	.040	.001821	.000052	503	.992	.840	1.000	1.067	222.47287	12.30309
.563	.043	.002122	.000067	500	.994	1.083	1.000	1.067	228.29739	11.92939
.607	.045	.002616	.000090	445	1.000	.856	1.000	1.067	125.15054	7.56699
.654	.050	.003024	.000119	371	1.000	.969	1.000	1.067	91.96625	5.92146
.706	.053	.003475	.000162	259	.986	.899	1.000	1.067	48.24547	3.81139
.761	.058	.004311	.000225	213	.993	.967	1.000	1.067	31.65339	2.70522
.821	.061	.004779	.000302	186	1.000	.979	1.000	1.067	24.15012	2.30937
.885	.067	.005478	.000401	132	.995	.985	1.000	1.067	13.62669	1.52973
.955	.073	.006396	.000487	87	.992	.906	1.000	1.067	6.47684	.86382
1.030	.078	.007501	.000594	51	1.000	.948	1.000	1.067	3.19826	.51225
1.112	.085	.010321	.000698	29	.976	.902	1.000	1.067	1.12592	.22872
1.200	.091	.009533	.000704	10	1.000	1.000	1.000	1.067	.44594	.14042
1.295	.099	.011049	.000685	3	1.000	1.000	1.000	1.067	.10609	.05966
1.399	.109	.011261	.000662	0	1.000	1.000	1.000	1.000	0.00000	.02958
1.512	.117	.012951	.000679	0	1.000	1.000	1.000	1.000	0.00000	.02395
1.634	.127	.013550	.000665	1	1.000	1.000	1.000	1.067	.02248	.02179
1.766	.138	.015416	.000657	2	1.000	1.000	1.000	1.067	.03637	.02494
1.912	.153	.016458	.000633	2	1.000	1.000	1.000	1.067	.03072	.02106
2.071	.166	.020203	.000627	6	1.000	1.000	1.000	1.067	.06921	.02743
2.246	.184	.021407	.000604	2	1.000	1.000	1.000	1.067	.01964	.01346
2.437	.198	.023351	.000594	2	1.000	1.000	1.000	1.067	.01673	.01146
2.644	.216	.024448	.000567	5	1.000	1.000	1.000	1.067	.03663	.01588
2.868	.232	.012645	.000469	3	1.000	1.000	1.000	1.067	.03956	.02216
3.117	.266	.001006	.000157	0	1.000	1.000	1.000	1.000	0.00000	.13712

Table A13.3. 200 GeV/c $\bar{p}p$ acceptance and corrections

t	Δt	ϵ	$\delta\epsilon$	N′	C_2	C_3	C_{4A}	C_{4B}	$\sigma_{\bar{p}}$	$\delta\sigma_{\bar{p}}$
.749	.098	.000715	.000034	1	1.000	1.000	.999	1.036	2.84976	2.80465
.830	.063	.001987	.000066	6	1.000	1.000	1.000	1.036	9.57894	3.85533
.895	.068	.003655	.000121	6	1.000	1.000	1.000	1.036	4.82252	1.94107
.966	.073	.004690	.000194	2	1.000	1.000	.998	1.036	1.16584	.81190
1.042	.080	.005825	.000308	3	1.000	1.000	.999	1.036	1.28544	.73259
1.125	.085	.006574	.000482	2	1.000	1.000	.999	1.036	.71224	.49781
1.214	.093	.006150	.000694	0	1.000	1.000	1.000	1.000	0.00000	.33939
1.311	.102	.008681	.001245	0	1.000	1.000	1.000	1.000	0.00000	.22006
1.417	.109	.008765	.001867	0	1.000	1.000	1.000	1.000	0.00000	.20642
1.531	.119	.009794	.002252	0	1.000	1.000	1.000	1.000	0.00000	.16981
1.655	.130	.006752	.002413	0	1.000	1.000	1.000	1.000	0.00000	.23335
1.793	.146	.014551	.003195	1	1.000	1.000	.999	1.036	.09403	.09467
1.933	.134	.014691	.003720	0	1.000	1.000	1.000	1.000	0.00000	.10107
2.100	.200	.013481	.002821	1	1.000	1.000	1.000	1.036	.07411	.07445
2.300	.200	.019488	.002964	1	1.000	1.000	1.000	1.036	.05127	.05097
2.500	.200	.025200	.003177	1	1.000	1.000	1.000	1.036	.03966	.03928
2.700	.200	.026365	.003152	1	1.000	1.000	1.000	1.036	.03790	.03751
2.900	.200	.034969	.003759	0	1.000	1.000	1.000	1.000	0.00000	.02774
3.100	.200	.027182	.003338	0	1.000	1.000	1.000	1.000	0.00000	.03575
3.350	.300	.029103	.002680	0	1.000	1.000	1.000	1.000	0.00000	.02219
3.650	.300	.031326	.002835	0	1.000	1.000	1.000	1.000	0.00000	.02061
4.000	.400	.031131	.002339	0	1.000	1.000	1.000	1.000	0.00000	.01553
4.400	.400	.030231	.002376	0	1.000	1.000	1.000	1.000	0.00000	.01600
4.800	.400	.034484	.002289	0	1.000	1.000	1.000	1.000	0.00000	.01401
5.500	1.000	.038381	.001468	0	1.000	1.000	1.000	1.000	0.00000	.00496
6.500	1.000	.037215	.001565	0	1.000	1.000	1.000	1.000	0.00000	.00519
7.500	1.000	.039586	.001487	0	1.000	1.000	1.000	1.000	0.00000	.00488
8.500	1.000	.042441	.001415	0	1.000	1.000	1.000	1.000	0.00000	.00455
9.500	1.000	.043812	.001392	0	1.000	1.000	1.000	1.000	0.00000	.00440
10.500	1.000	.037936	.001493	0	1.000	1.000	1.000	1.000	0.00000	.00509
11.500	1.000	.012874	.001205	0	1.000	1.000	1.000	1.000	0.00000	.01505

Table A13.4. 100 GeV/c pp acceptance and corrections

t	Δt	ϵ	$\delta\epsilon$	N'	C_2	C_3	C_{4A}	C_{4B}	σ_p	$\delta\sigma_p$
.349	.098	.000186	.000005	384	.994	1.679	.998	1.003	728.58954	33.92637
.414	.031	.000676	.000013	761	.997	1.097	.999	1.003	822.36155	32.71742
.447	.035	.001157	.000019	1288	.995	1.147	.998	1.003	751.23927	23.17955
.483	.037	.001547	.000025	1718	.998	.980	.998	1.003	607.96522	17.83492
.521	.040	.001841	.000033	1603	.997	.940	.998	1.003	422.07971	13.19733
.563	.043	.002226	.000042	1508	.998	.987	.996	1.003	320.65495	10.26456
.607	.045	.002659	.000055	1243	.996	.874	.997	1.003	187.12991	6.86559
.654	.050	.003092	.000070	1030	.996	.986	.997	1.003	135.22542	5.24593
.706	.053	.003922	.000098	831	.997	.891	.994	1.003	73.23637	3.26124
.761	.058	.004199	.000124	673	.993	.955	.995	1.003	54.10137	2.67559
.821	.061	.005388	.000175	540	.996	.996	.994	1.003	33.59146	1.81621
.885	.067	.005970	.000223	362	.995	.915	.990	1.003	16.91066	1.12862
.955	.073	.006695	.000289	220	.997	.917	.989	1.003	8.44385	.69985
1.030	.078	.007895	.000348	139	.996	.940	.984	1.003	4.30963	.42514
1.112	.085	.008589	.000389	85	.993	1.028	.979	1.003	2.41374	.28338
1.200	.091	.010816	.000441	52	.989	.886	.975	1.003	.93673	.14539
1.295	.099	.011444	.000441	23	.974	.927	.959	1.003	.36446	.08276
1.399	.109	.012962	.000451	6	1.000	1.000	.833	1.003	.07334	.03286
1.512	.117	.014312	.000458	9	1.000	1.000	.961	1.003	.10718	.03654
1.634	.127	.015272	.000442	9	1.000	1.000	.960	1.003	.09237	.03149
1.766	.138	.016399	.000438	11	.946	1.030	.977	1.003	.09600	.02973
1.912	.153	.018494	.000422	12	1.000	.974	.982	1.003	.08412	.02487
2.071	.166	.020431	.000418	13	1.000	.998	.997	1.003	.07915	.02203
2.246	.184	.023053	.000387	13	1.000	1.028	.997	1.003	.06515	.01785
2.437	.198	.025285	.000380	9	1.000	1.000	1.000	1.003	.03728	.01242
2.644	.216	.025698	.000367	7	1.000	1.000	.994	1.003	.02600	.00985
2.868	.232	.012701	.000309	8	1.000	1.000	1.000	1.003	.05631	.01992
3.117	.266	.000747	.000089	0	1.000	1.000	1.000	1.000	0.00000	.10477

Table A13.5. 200 GeV/c pp acceptance and corrections

t	Δt	ϵ	$\delta\epsilon$	N'	C_2	C_3	C_{4A}	C_{4B}	σ_p	$\delta\sigma_p$
.749	.098	.001379	.000013	546	.989	1.281	1.000	1.016	13.92556	.54064
.830	.063	.002463	.000019	858	.996	.961	1.000	1.016	14.38336	.51065
.895	.068	.003916	.000032	1047	.996	1.004	1.000	1.016	10.69656	.33923
.966	.073	.005583	.000052	854	.995	.948	1.000	1.016	5.37210	.19428
1.042	.080	.006663	.000078	615	.995	.942	1.000	1.016	2.94065	.12626
1.125	.085	.008156	.000124	334	.994	.927	.999	1.016	1.20642	.07064
1.214	.093	.008861	.000187	157	.997	.921	.999	1.016	.47516	.04054
1.311	.102	.009947	.000296	58	.975	.936	.997	1.016	.14145	.01977
1.417	.109	.011175	.000461	11	.956	1.046	.991	1.016	.02433	.00738
1.531	.119	.012858	.000654	14	.931	1.047	.995	1.016	.02412	.00661
1.655	.130	.014154	.000825	18	.973	.992	.997	1.016	.02559	.00628
1.793	.146	.016477	.000849	34	.986	1.032	.999	1.016	.03906	.00689
1.933	.134	.017720	.000956	38	1.000	1.027	1.000	1.016	.04467	.00749
2.100	.200	.018401	.000791	65	1.000	1.026	1.000	1.016	.04926	.00635
2.300	.200	.019705	.000803	33	1.000	.889	1.000	1.016	.02023	.00380
2.500	.200	.022398	.000821	40	.988	1.093	1.000	1.016	.02621	.00407
2.700	.200	.023217	.000855	37	1.000	.908	1.000	1.016	.01966	.00344
2.900	.200	.025816	.000877	22	1.000	1.000	1.000	1.016	.01159	.00248
3.100	.200	.027207	.000873	10	.903	1.107	1.000	1.016	.00500	.00158
3.350	.300	.030596	.000714	32	.985	1.072	1.000	1.016	.01001	.00172
3.650	.300	.031259	.000711	0	1.000	1.000	1.000	1.000	0.00000	.00029
4.000	.400	.030921	.000617	3	1.000	1.000	1.000	1.016	.00066	.00038
4.400	.400	.032635	.000623	2	1.000	1.000	1.000	1.016	.00042	.00029
4.800	.400	.033872	.000610	4	1.000	1.000	1.000	1.016	.00080	.00040
5.500	1.000	.034678	.000393	0	1.000	1.000	1.000	1.000	0.00000	.00008
6.500	1.000	.034119	.000391	1	1.000	1.000	1.000	1.016	.00008	.00008
7.500	1.000	.037352	.000383	2	1.000	1.000	1.000	1.016	.00015	.00010
8.500	1.000	.040661	.000376	0	1.000	1.000	1.000	1.000	0.00000	.00007
9.500	1.000	.041415	.000377	0	1.000	1.000	1.000	1.000	0.00000	.00006
10.500	1.000	.034920	.000391	0	1.000	1.000	1.000	1.000	0.00000	.00008
11.500	1.000	.010268	.000292	0	1.000	1.000	1.000	1.000	0.00000	.00026

Table A13.6. 100 GeV/c $\pi^- p$ acceptance and corrections

t	Δt	ϵ	$\delta\epsilon$	N'	C_2	C_3	C_{4A}	C_{4B}	σ_π	$\delta\sigma_\pi$
.349	.098	.000179	.000003	9153	.997	1.707	.995	1.009	682.10753	14.07430
.414	.031	.000640	.000009	16337	.998	1.037	.995	1.009	653.22242	10.34514
.447	.035	.001133	.000012	26315	.998	1.111	.990	1.009	560.98941	6.82812
.483	.037	.001570	.000015	33337	.997	1.004	.991	1.009	438.48689	4.84299
.521	.040	.001890	.000018	36560	.997	.981	.991	1.009	361.11005	3.88315
.563	.043	.002164	.000020	38057	.997	.998	.989	1.009	310.19354	3.30998
.607	.045	.002611	.000024	36139	.998	.957	.990	1.009	223.91912	2.40850
.654	.050	.003068	.000028	35085	.997	.963	.990	1.009	167.49515	1.79465
.706	.053	.003604	.000034	33307	.997	.975	.990	1.009	129.29394	1.41305
.761	.058	.004188	.000040	31278	.998	.967	.990	1.009	94.72065	1.05697
.821	.061	.005002	.000049	27682	.997	.966	.989	1.009	66.53874	.77328
.885	.067	.006004	.000060	24394	.997	.984	.992	1.009	45.47993	.54323
.955	.073	.006698	.000072	19932	.996	.957	.988	1.009	29.58965	.38215
1.030	.078	.007720	.000089	15899	.997	.981	.989	1.009	19.67845	.27566
1.112	.085	.008898	.000109	12472	.998	.955	.987	1.009	11.94844	.18306
1.200	.091	.010099	.000133	9511	.996	.973	.986	1.009	7.61837	.12795
1.295	.099	.010822	.000157	6733	.996	.958	.988	1.009	4.56546	.08753
1.399	.109	.012097	.000181	4700	.996	.988	.985	1.009	2.65890	.05584
1.512	.117	.013405	.000208	3168	.997	.965	.989	1.009	1.47873	.03530
1.634	.127	.014702	.000224	2092	.994	.978	.981	1.009	.82268	.02223
1.766	.138	.016067	.000238	1346	.993	.984	.984	1.009	.44941	.01411
1.912	.153	.017693	.000237	838	.992	.940	.985	1.009	.21930	.00840
2.071	.166	.019778	.000236	478	.994	.981	.982	1.009	.10738	.00516
2.246	.184	.021880	.000232	261	.997	.978	.966	1.009	.04708	.00303
2.437	.196	.023908	.000224	107	.987	.913	.953	1.009	.01494	.00156
2.644	.216	.024811	.000215	51	.931	1.004	.961	1.009	.00658	.00097
2.868	.232	.012435	.000181	15	.860	1.047	.955	1.009	.00344	.00096
3.117	.266	.001039	.000061	0	1.000	1.000	1.000	1.000	0.00000	.00277

Table A13.7. 200 GeV/c $\pi^- p$ acceptance and corrections

t	Δt	ϵ	$\delta\epsilon$	N'	C_2	C_3	C_{4A}	C_{4B}	σ_π	$\delta\sigma_\pi$
.749	.098	.000793	.000014	5702	.995	1.340	.964	1.000	60.16996	1.26535
.830	.063	.002174	.000023	9354	.997	.950	.958	1.000	39.51675	.59551
.895	.068	.003870	.000034	13129	.997	1.021	.956	1.000	30.98396	.38406
.966	.073	.005363	.000045	14468	.997	.986	.955	1.000	22.13994	.26495
1.042	.080	.006499	.000056	13014	.997	.965	.950	1.000	14.58817	.18398
1.125	.085	.007413	.000071	10366	.996	.962	.943	1.000	9.48408	.13327
1.214	.093	.008324	.000088	7783	.996	.970	.937	1.000	5.80221	.09223
1.311	.102	.009261	.000111	5505	.996	.963	.926	1.000	3.30008	.06158
1.417	.109	.009832	.000141	3777	.996	.979	.915	1.000	2.00564	.04499
1.531	.119	.011011	.000185	2505	.995	.969	.912	1.000	1.07226	.02907
1.655	.130	.012403	.000246	1709	.994	.984	.901	1.000	.59604	.01939
1.793	.146	.013537	.000320	1191	.994	.983	.894	1.000	.33589	.01310
1.933	.134	.016369	.000456	623	.996	1.006	.885	1.000	.16068	.00817
2.100	.200	.018091	.000496	463	.992	.943	.875	1.000	.06687	.00389
2.300	.200	.020084	.000592	208	.983	.954	.851	1.000	.02636	.00219
2.500	.200	.020947	.000679	90	.984	.933	.853	1.000	.01074	.00133
2.700	.200	.023256	.000724	39	.982	.868	.732	1.000	.00334	.00068
2.900	.200	.027101	.000777	17	1.000	.994	.816	1.000	.00162	.00044
3.100	.200	.027413	.000752	6	1.000	1.000	.779	1.000	.00054	.00025
3.350	.300	.030207	.000620	3	1.000	1.000	.668	1.000	.00014	.00010
3.650	.300	.030276	.000628	0	1.000	1.000	1.000	1.000	0.00000	.00007
4.000	.400	.032173	.000542	0	1.000	1.000	1.000	1.000	0.00000	.00005
4.400	.400	.033085	.000543	1	1.000	1.000	.981	1.000	.00005	.00005
4.800	.400	.034021	.000542	4	1.000	1.000	.999	1.000	.00019	.00009
5.500	1.000	.036254	.000340	5	1.000	1.000	1.000	1.000	.00009	.00004
6.500	1.000	.036116	.000513	5	1.000	1.000	1.000	1.000	.00009	.00004
7.500	1.000	.038030	.000512	0	1.000	1.000	1.000	1.000	0.00000	.00002
8.500	1.000	.041042	.000495	0	1.000	1.000	1.000	1.000	0.00000	.00002
9.500	1.000	.042287	.000494	1	1.000	1.000	1.000	1.000	.00002	.00002
10.500	1.000	.038063	.000513	1	1.000	1.000	1.000	1.000	.00002	.00002
11.500	1.000	.010625	.000389	1	1.000	1.000	1.000	1.000	.00006	.00006

Table A13.8. 100 GeV/c π^+p acceptance and corrections

t	Δt	ϵ	$\delta\epsilon$	N′	C_2	C_3	C_{4A}	C_{4B}	σ_π	$\delta\sigma_\pi$
.349	.098	.000199	.000005	450	.997	1.702	.990	1.009	553.08281	23.96553
.414	.031	.000688	.000012	832	.999	1.044	.983	1.009	569.99989	21.87713
.447	.035	.001137	.000016	1533	.998	1.175	.984	1.009	633.89524	17.46606
.483	.037	.001554	.000020	2078	.997	.999	.986	1.009	505.79864	12.88027
.521	.040	.001904	.000023	2167	.999	.973	.988	1.009	389.32975	9.76237
.563	.043	.002186	.000027	2291	.997	1.000	.982	1.009	340.34825	8.29478
.607	.045	.002601	.000032	2119	.999	.955	.989	1.009	243.32347	6.19674
.654	.050	.003179	.000038	2078	.999	.959	.986	1.009	175.94265	4.48029
.706	.053	.003678	.000045	1963	.999	.979	.983	1.009	137.94482	3.59154
.761	.058	.004284	.000054	1749	.997	.949	.985	1.009	93.52841	2.58584
.821	.061	.005071	.000066	1653	.998	.982	.985	1.009	73.56867	2.06749
.885	.067	.006087	.000080	1370	1.000	.964	.980	1.009	45.23234	1.38523
.955	.073	.006918	.000096	1070	.999	.949	.983	1.009	28.15368	.96977
1.030	.078	.007798	.000118	917	.997	.976	.981	1.009	20.53158	.75762
1.112	.085	.009110	.000144	730	.997	.973	.979	1.009	12.75933	.52297
1.200	.091	.010138	.000177	604	.999	.965	.985	1.009	8.86466	.39955
1.295	.099	.011443	.000212	441	.999	.972	.984	1.009	5.29989	.27514
1.399	.109	.012008	.000239	278	.998	.971	.970	1.009	2.84706	.18428
1.512	.117	.013717	.000274	204	1.000	.975	.986	1.009	1.74173	.12862
1.634	.127	.014721	.000297	150	.988	.984	.980	1.009	1.09005	.09339
1.766	.138	.016431	.000309	87	.993	.982	.977	1.009	.52144	.05784
1.912	.153	.018989	.000314	56	1.000	.932	.968	1.009	.24788	.03496
2.071	.166	.020082	.000313	36	1.000	.988	.992	1.009	.15095	.02540
2.246	.184	.022558	.000308	17	1.000	.968	.981	1.009	.05545	.01376
2.437	.198	.024562	.000297	11	.946	1.057	1.000	1.009	.03225	.00969
2.644	.216	.026005	.000287	13	1.000	1.037	.976	1.009	.03339	.00917
2.868	.232	.012092	.000234	1	1.000	1.000	1.000	1.009	.00508	.00506
3.117	.266	.000851	.000074	0	1.000	1.000	1.000	1.000	0.00000	.06264

Table A13.9. 200 GeV/c π^+p acceptance and corrections

t	Δt	ϵ	$\delta\epsilon$	N'	C_2	C_3	C_{4A}	C_{4B}	σ_π	$\delta\sigma_\pi$
.749	.098	.001405	.000022	228	.994	1.289	.680	1.000	21.97390	1.59870
.830	.063	.002591	.000031	474	.999	1.009	.822	1.000	36.69916	1.90139
.895	.068	.004002	.000043	720	1.000	1.041	.860	1.000	36.10616	1.47385
.966	.073	.005603	.000059	714	.999	.964	.843	1.000	21.60230	.92529
1.042	.080	.006965	.000076	664	.999	.969	.844	1.000	14.84074	.65751
1.125	.085	.008196	.000098	525	.995	.963	.837	1.000	9.21028	.46231
1.214	.093	.009216	.000126	401	.999	.978	.834	1.000	5.80648	.33097
1.311	.102	.010279	.000162	306	.998	.966	.832	1.000	3.57348	.23477
1.417	.109	.011072	.000214	200	.998	.977	.824	1.000	2.02796	.16477
1.531	.119	.012634	.000289	125	.996	.938	.788	1.000	.93326	.09958
1.655	.130	.014574	.000392	100	1.000	1.021	.826	1.000	.67852	.07611
1.793	.146	.015264	.000520	47	.990	.923	.745	1.000	.21881	.03940
1.933	.134	.016528	.000767	34	.986	1.019	.822	1.000	.19325	.03755
2.100	.200	.018683	.000785	19	1.000	.961	.721	1.000	.05371	.01497
2.300	.200	.020571	.001003	11	1.000	.956	.784	1.000	.03054	.01074
2.500	.200	.024057	.001107	6	1.000	1.000	.752	1.000	.01429	.00676
2.700	.200	.024341	.001131	3	1.000	1.000	.726	1.000	.00682	.00463
2.900	.200	.026337	.001184	0	1.000	1.000	1.000	1.000	0.00000	.00290
3.100	.200	.028594	.001190	0	1.000	1.000	1.000	1.000	0.00000	.00267
3.350	.300	.030513	.000965	0	1.000	1.000	1.000	1.000	0.00000	.00167
3.650	.300	.031614	.000992	0	1.000	1.000	1.000	1.000	0.00000	.00161
4.000	.400	.032194	.000849	1	1.000	1.000	.951	1.000	.00113	.00115
4.400	.400	.033685	.000842	0	1.000	1.000	1.000	1.000	0.00000	.00113
4.800	.400	.034036	.000853	0	1.000	1.000	1.000	1.000	0.00000	.00112
5.500	1.000	.035744	.000531	0	1.000	1.000	1.000	1.000	0.00000	.00043
6.500	1.000	.035670	.000533	0	1.000	1.000	1.000	1.000	0.00000	.00043
7.500	1.000	.039038	.000521	0	1.000	1.000	1.000	1.000	0.00000	.00039
8.500	1.000	.042484	.000506	0	1.000	1.000	1.000	1.000	0.00000	.00036
9.500	1.000	.042286	.000505	0	1.000	1.000	1.000	1.000	0.00000	.00036
10.500	1.000	.034420	.000524	0	1.000	1.000	1.000	1.000	0.00000	.00044
11.500	1.000	.009903	.000390	0	1.000	1.000	1.000	1.000	0.00000	.00154

Table A13.10. 100 GeV/c K^-p acceptance and corrections

t	Δt	ϵ	$\delta\epsilon$	N′	C_2	C_3	C_{4A}	C_{4B}	σ_K	$\delta\sigma_K$
.349	.098	.000151	.000008	89	.992	1.910	.662	1.259	414.62043	41.69474
.414	.031	.000572	.000022	194	1.000	1.013	.686	1.259	417.25103	35.89316
.447	.035	.001049	.000031	423	.993	1.253	.802	1.259	630.48693	33.01599
.483	.037	.001407	.000038	572	.994	1.005	.789	1.259	475.11669	23.66338
.521	.040	.001680	.000044	649	.995	.949	.798	1.259	398.78752	19.21858
.563	.043	.001949	.000051	698	.996	1.035	.815	1.259	383.77973	17.32752
.607	.045	.002358	.000061	663	.990	.952	.810	1.259	261.87592	12.40064
.654	.050	.002734	.000071	620	.997	.949	.802	1.259	188.77109	9.16500
.706	.053	.003240	.000086	590	.995	.997	.815	1.259	152.41208	7.40745
.761	.058	.003834	.000102	556	.989	.945	.806	1.259	103.26498	5.27294
.821	.061	.004375	.000123	517	.995	1.021	.830	1.259	89.58691	4.57686
.885	.067	.005256	.000150	401	.986	.904	.778	1.259	43.29728	2.62152
.955	.073	.006025	.000182	383	.987	1.025	.839	1.259	40.54878	2.34752
1.030	.078	.006937	.000224	326	.994	.937	.833	1.259	25.62174	1.65813
1.112	.085	.008788	.000285	262	.997	1.002	.854	1.259	16.41312	1.11343
1.200	.091	.009191	.000336	223	.997	.984	.865	1.259	12.40952	.92300
1.295	.099	.010032	.000400	148	.991	.931	.850	1.259	6.40509	.58832
1.399	.109	.010463	.000456	117	1.000	1.015	.877	1.259	5.00559	.48860
1.512	.117	.012490	.000525	67	.979	.926	.840	1.259	1.91597	.25219
1.634	.127	.013523	.000573	62	.989	1.025	.898	1.259	1.80123	.22695
1.766	.138	.014842	.000617	36	1.000	.972	.880	1.259	.82428	.13676
1.912	.153	.015437	.000591	20	1.000	.956	.868	1.259	.38541	.08558
2.071	.166	.018080	.000610	15	1.000	.935	.885	1.259	.22668	.05786
2.246	.184	.020165	.000596	13	1.000	1.029	.937	1.259	.18539	.04697
2.437	.198	.021540	.000582	7	1.000	1.000	.951	1.259	.08562	.02966
2.644	.216	.024012	.000581	3	1.000	1.000	.911	1.259	.02891	.01560
2.868	.232	.011967	.000471	1	1.000	1.000	.887	1.259	.01752	.01659
3.117	.266	.001136	.000169	0	1.000	1.000	1.000	1.000	0.00000	.14572

Table A13.11. 200 GeV/c K^-p acceptance and corrections

t	Δt	ϵ	$\delta\epsilon$	N′	C_2	C_3	C_{4A}	C_{4B}	σ_K	$\delta\sigma_K$
.749	.098	.000726	.000034	5	1.000	1.000	.969	1.008	47.06404	21.40849
.830	.063	.002103	.000057	9	1.000	1.000	.973	1.008	45.72379	15.43716
.895	.068	.003994	.000087	18	1.000	1.075	.974	1.008	47.99829	11.06056
.966	.073	.005431	.000115	15	1.000	.911	.975	1.008	23.25403	6.36215
1.042	.080	.006534	.000144	18	1.000	1.002	.978	1.008	23.32232	5.55607
1.125	.085	.007842	.000184	24	1.000	1.023	.981	1.008	24.98255	5.10442
1.214	.093	.008581	.000226	13	1.000	.911	.983	1.008	10.07946	2.95537
1.311	.102	.009460	.000287	6	1.000	1.000	.985	1.008	4.23607	1.74009
1.417	.109	.010865	.000377	5	1.000	1.000	.987	1.008	2.88220	1.29591
1.531	.119	.010614	.000468	8	1.000	1.000	.988	1.008	4.32536	1.54442
1.655	.130	.012524	.000634	2	1.000	1.000	.989	1.008	.84019	.59648
1.793	.146	.014496	.000865	1	1.000	1.000	.990	1.008	.32344	.32435
1.933	.134	.016097	.001206	0	1.000	1.000	.991	1.008	0.00000	.31890
2.100	.200	.015915	.001371	1	1.000	1.000	.992	1.008	.21541	.21625
2.300	.200	.019099	.001713	1	1.000	1.000	.993	1.008	.17979	.18041
2.500	.200	.017779	.001917	0	1.000	1.000	.993	1.008	0.00000	.19402
2.700	.200	.029080	.002492	0	1.000	1.000	.997	1.008	0.00000	.11837
2.900	.200	.022784	.002214	0	1.000	1.000	.995	1.008	0.00000	.15124
3.100	.200	.021762	.002157	0	1.000	1.000	.996	1.008	0.00000	.15837
3.350	.300	.029781	.001849	0	1.000	1.000	.998	1.008	0.00000	.07692
3.650	.300	.026257	.001955	0	1.000	1.000	1.000	1.008	0.00000	.08732
4.000	.400	.030308	.001596	0	1.000	1.000	1.000	1.008	0.00000	.05666
4.400	.400	.028495	.001685	0	1.000	1.000	.941	1.008	0.00000	.06029
4.800	.400	.030839	.001693	0	1.000	1.000	.458	1.008	0.00000	.05569
5.500	1.000	.030647	.001052	0	1.000	1.000	.092	1.008	0.00000	.02240
6.500	1.000	.031831	.001060	0	1.000	1.000	.002	1.008	0.00000	.02156
7.500	1.000	.034206	.001076	0	1.000	1.000	1.000	1.008	0.00000	.02006
8.500	1.000	.038373	.001056	0	1.000	1.000	1.000	1.008	0.00000	.01788
9.500	1.000	.036960	.001044	0	1.000	1.000	.000	1.008	0.00000	.01857
10.500	1.000	.035408	.001066	0	1.000	1.000	.000	1.008	0.00000	.01938
11.500	1.000	.008189	.000713	0	1.000	1.000	.000	1.008	0.00000	.08408

Table A13.12. 100 GeV/c K^+p acceptance and corrections

t	Δt	ϵ	$\delta\epsilon$	N′	C_2	C_3	C_{4A}	C_{4B}	σ_K	$\delta\sigma_K$
.349	.098	.000165	.000011	16	1.000	1.744	.784	1.274	428.55427	86.18377
.414	.031	.000602	.000029	39	1.000	1.225	.853	1.274	693.96313	102.09000
.447	.035	.001093	.000041	84	1.000	1.129	.852	1.274	670.96562	70.66096
.483	.037	.001523	.000051	100	.994	1.007	.839	1.274	472.94663	48.36579
.521	.040	.001751	.000058	99	1.000	.880	.816	1.274	322.32786	35.53147
.563	.043	.002075	.000068	119	.995	1.127	.873	1.274	414.18756	36.61752
.607	.045	.002631	.000083	99	.994	.809	.816	1.274	174.20629	19.92422
.654	.050	.002830	.000093	91	.994	1.022	.846	1.274	175.37438	18.49428
.706	.053	.003439	.000113	105	1.000	1.002	.874	1.274	160.22394	15.71438
.761	.058	.003903	.000133	86	.993	.948	.859	1.274	97.59105	10.88876
.821	.061	.004393	.000158	86	.993	.949	.864	1.274	82.97021	9.28060
.885	.067	.005543	.000198	83	1.000	1.008	.896	1.274	64.05369	6.94605
.955	.073	.006380	.000240	58	.990	.954	.879	1.274	32.85152	4.37185
1.030	.078	.007028	.000289	55	1.000	.954	.891	1.274	27.09418	3.68262
1.112	.085	.008142	.000357	46	.987	1.009	.902	1.274	18.95987	2.74215
1.200	.091	.009383	.000431	31	1.000	.926	.873	1.274	9.31943	1.70428
1.295	.099	.010724	.000528	23	1.000	.948	.878	1.274	5.72346	1.19299
1.399	.109	.012217	.000626	24	1.000	1.005	.932	1.274	5.36286	1.03888
1.512	.117	.012793	.000726	9	1.000	1.000	.863	1.274	1.64694	.53199
1.634	.127	.014974	.000749	9	1.000	1.000	.899	1.274	1.35151	.42631
1.766	.138	.016322	.000823	6	1.000	1.000	.910	1.274	.77017	.29453
1.912	.153	.017330	.000814	5	1.000	1.000	.932	1.274	.55838	.23062
2.071	.166	.018529	.000796	1	1.000	1.000	.754	1.274	.07785	.07950
2.246	.184	.020280	.000776	1	1.000	1.000	.872	1.274	.07422	.07047
2.437	.198	.023114	.000767	0	1.000	1.000	1.000	1.000	0.00000	.05450
2.644	.216	.024121	.000721	1	1.000	1.000	.904	1.274	.05509	.05137
2.868	.232	.011297	.000611	0	1.000	1.000	1.000	1.000	0.00000	.09525
3.117	.266	.000721	.000174	0	1.000	1.000	1.000	1.000	0.00000	1.33658

Table A13.13. 200 GeV/c K^+p acceptance and corrections

t	Δt	ϵ	$\delta\epsilon$	N′	C_2	C_3	C_{4A}	C_{4B}	σ_K	$\delta\sigma_K$
.749	.098	.001323	.000044	3	.839	1.192	.989	1.003	10.36636	6.01993
.830	.063	.002377	.000059	22	1.000	1.149	.973	1.003	74.47154	15.10345
.895	.068	.003722	.000083	26	1.000	.979	.965	1.003	44.00619	8.91841
.966	.073	.005343	.000115	19	1.000	.916	.971	1.003	19.63451	4.78828
1.042	.080	.006715	.000149	29	1.000	1.031	.972	1.003	24.49680	4.57198
1.125	.085	.007586	.000190	21	1.000	.945	.974	1.003	13.59233	3.10503
1.214	.093	.008881	.000245	6	1.000	1.000	.975	1.003	3.21140	1.32851
1.311	.102	.009597	.000315	12	1.000	1.085	.976	1.003	5.88378	1.65932
1.417	.109	.010765	.000420	7	1.000	1.000	.978	1.003	2.64383	1.01432
1.531	.119	.011295	.000546	6	1.000	1.000	.982	1.003	1.98774	.82312
1.655	.130	.014153	.000779	5	1.000	1.000	.977	1.003	1.20361	.54772
1.793	.146	.014326	.001026	2	1.000	1.000	.986	1.003	.42716	.30532
1.933	.134	.015208	.001431	3	1.000	1.000	.976	1.003	.65099	.38484
2.100	.200	.017548	.001610	0	1.000	1.000	.984	1.003	0.00000	.12930
2.300	.200	.022375	.001966	2	1.000	1.000	.978	1.003	.19802	.14248
2.500	.200	.021121	.002049	1	1.000	1.000	.970	1.003	.10412	.10602
2.700	.200	.023086	.002269	0	1.000	1.000	.961	1.003	0.00000	.09834
2.900	.200	.027876	.002430	0	1.000	1.000	.986	1.003	0.00000	.09136
3.100	.200	.026192	.002368	0	1.000	1.000	.985	1.003	0.00000	.08662
3.350	.300	.029794	.002009	0	1.000	1.000	.911	1.003	0.00000	.05067
3.650	.300	.026343	.001941	0	1.000	1.000	1.000	1.003	0.00000	.05734
4.000	.400	.030471	.001697	0	1.000	1.000	.292	1.003	0.00000	.03713
4.400	.400	.032961	.001730	0	1.000	1.000	.641	1.003	0.00000	.03432
4.800	.400	.033206	.001767	0	1.000	1.000	.124	1.003	0.00000	.03407
5.500	1.000	.034580	.001069	0	1.000	1.000	1.000	1.003	0.00000	.01307
6.500	1.000	.030618	.001097	0	1.000	1.000	.000	1.003	0.00000	.01477
7.500	1.000	.037136	.001033	0	1.000	1.000	.000	1.003	0.00000	.01217
8.500	1.000	.039561	.001006	0	1.000	1.000	1.000	1.003	0.00000	.01143
9.500	1.000	.037255	.001075	0	1.000	1.000	1.000	1.003	0.00000	.01213
10.500	1.000	.033237	.001070	0	1.000	1.000	1.000	1.003	0.00000	.01360
11.500	1.000	.009692	.000777	0	1.000	1.000	1.000	1.003	0.00000	.04677

Appendix 14

Chou-Yang Analysis

The Chou-Yang model is used to determine form factors from the elastic differential cross sections. Equation (24) of section II was integrated numerically using equation (1) of section II to define the scattering amplitude. The value of μ is set by normalizing the form factors to 1 at $q^2 = -t = 0$. The data were smoothed by fitting the scattering amplitude to the form

$$\begin{aligned} \mathrm{Im}\ a &= \frac{k}{\sqrt{\pi}} \sqrt{\frac{d\sigma}{dt}} \\ &= \frac{k}{\sqrt{\pi}} \left[\sqrt{A}\, e^{-\frac{(bt + ct^2 + dt^3)}{2}} \right. \\ &\qquad \left. + \sqrt{B}\, e^{-(t - t_{mx})} \left(\frac{\gamma + \beta}{2} + \frac{\gamma - \beta}{2} \tanh \left(\frac{t - t_{mx}}{\delta} \right) \right) \right] \end{aligned} \tag{1}$$

The first term describes a Gaussian with modifications at high $-t$. The second term was used to fit the secondary maximum. In this term the argument of the exponent goes to $\beta(t - t_m)$ for $t << t_m$ and $\gamma(t - t_m)$ for $t \gg t_m$. The hyperbolic tangent smoothes the transition between these two limits. The square root introduces an ambiguity in sign. At the dip the scattering amplitude can change sign or just have a minimum. Both cases were calculated. In the proton-proton case, a comparison to the electromagnetic form

factors clearly favors a change of sign at the dip. If no change in sign is made, then the calculated form factor falls too slowly with increasing -t.

The data used for the fit include data points from references 9, 1, 2, 3, of the main text and this experiment. The calculation was done numerically over the range

$$0 < -t < 3.25 \ (\mathrm{GeV}/c)^2$$

and

$$0 < b < 15.0 \ (\mathrm{GeV}/c)^{-1}$$

The number of bins used was 2800 for the t integration and 3000 for the b integration. Similar work has been done with a parallel analysis of this experiment,[1] and a similar analysis has been done for high energy low -t elastic scattering.[2]

References

1. Paul Karchin and Jay O'rear, "Determination of the pion form factor at large q," Cornell University Preprint; see also, Paul Karchin, "Measurement of pion proton deep elastic scattering at 13.7 and 19.4 GeV center of mass energies," Ph.D. Thesis, Cornell University (1982).

2. D. S. Ayres, Phys. Rev. D14 (1976) 3092.

Table A14.I

Parameters for fit to scattering amplitude

Parameter	pp	$\pi^- p$
A	77,915	29,306
B	.044934	.010091
b	11.793	9.7516
c	-3.4706	-2.9306
d	1.4992	.57982
Y	.62648	.15400
B	-3.3583	-9.6723
t_{mx}	1.6502	4.4670
δ [1]	.48893	.50000

[1] δ was fixed at $\delta = .5$ for the $\pi^- p$ fit.